Dissertation
submitted to the
Combined Faculties for the Natural Sciences and for Mathematics
of the Ruperto-Carola University of Heidelberg, Germany

for the degree of
Doctor of Natural Sciences

presented by
Dipl.-Phys. **Björn Eike**
born in Hildesheim

Oral examination: 6th November 2002

Laser-trapped Atoms as a Precision Target for the Heavy-Ion Storage Ring TSR

Referees:
Priv.-Doz. Dr. Matthias Weidemüller
Prof. Dr. H.-Jürgen Kluge

Zusammenfassung

Eine magnetooptische Falle für ultrakalte Cäsiumatome wurde als Target im Heidelberger Testspeicherring TSR installiert. Die gute Lokalisierung und die zu vernachlässigende thermische Energie machen die gefangenen Atome zu einem idealen Target zur Untersuchung elementarer Stoßprozesse mit gespeicherten Schwerionen bei einer Energie von einigen MeV/u. Stoßquerschnitte für die Ionisation der Targetatome durch unterschiedliche Projektilionen werden durchgeführt und mit theoretischen Vorhersagen verglichen. Weiterhin wird der Elektronenübertrag vom Target auf das Projektil untersucht. Die sich beim Einfang des Elektrons ergebenden Leerstellen in inneren Schalen des Targets führen über Auger-Kaskaden und Shake-off-Prozesse zu verschiedenen Ladungszuständen des Cäsiums. Diese Ladungszustände werden durch Flugzeitmessungen aufgelöst Die Flugzeitspektren erlauben eine Abschätzung des Impulsübertrags auf das rückgestoßene Cäsium-Ion. Desweiteren werden die gefangenen Atome eingesetzt, um die zweidimensionale Dichteverteilung des gespeicherten Ionenstrahls zu vermessen. Diese Methode ist besonders für sehr dünne Ionenstrahlen interessant, da jetzt verlässliche Messungen bis in den Bereich von 10 nA möglich sind. Die Auflösung dieser Messmethode ist nur durch die Größe der Atomwolke gegeben (jetziger Durchmesser: einige 100 μm). Diese Auflösung ist schon jetzt besser als die des Restgas-Strahlprofil-Monitors im TSR.

Abstract

A target based on ultracold cesium atoms confined in a magneto-optical trap (MOT) has been installed inside the Heidelberg Test Storage Ring TSR. Since the trapped atoms are very well localized and their thermal energy can be neglected they are ideally suited to study collisions with stored heavy ions at energies of some MeV/u. Measurements of collision cross sections for ionization of the target atoms are carried out and the results are compared to theoretical predictions. Additionally, the transfer of electrons from the target atom to the projectile ion is investigated. Inner shell vacancies produced in the capture process are filled by Auger-cascades and shake-off processes. Therefore, the cesium is ionized to several charge states. The charge states are resolved by time-of-flight measurements. From the TOF spectra the momentum transfer to the recoiled cesium ion is determined. As an additional application the trapped atoms are used to measure the two-dimensional density distribution of the stored ions. This method is of great interest for very dilute beams because reliable measurements down to very low ion currents in the order of 10 nA become possible. The resolution of this method is only limited by the size of the atom cloud (actual diameter: some 100 μm). Thus, the resolution is better than resolution of the restgas beam profile monitor at TSR.

It is a capital mistake to theorize before one has data. Insensibly one begins to twist facts to suit theories, instead of theories to suit facts.

Sherlock Holmes in *A Scandal in Bohemia*

Contents

Chapter 1

Introduction

Understanding the dynamics of atom-atom collisions has been the subject of scattering experiments since the beginning of the last century. The aim was not only to describe the static structures of atoms but also to get a deeper and more detailed insight into the dynamic behaviour during the interaction of atoms with another particle. The dynamics of collisions between ions and atoms are very important in several areas of science: The description of astrophysical plasmas [Stancil et al., 1998] and of sequences in the atmosphere [Hodges and Breig, 1991] have to deal with ion-atom interactions. In addition, for applications where ion-atom-collisions are of interest, e.g. in tumour therapy using heavy ions [GSI, 1996] and in chemical processes the understanding of this interaction is necessary.

Laser-trapped atoms are an ideal target because the thermal energy of the trapped atoms can be neglected completely. The thermal motion of the target does not contribute to measurements of the momentum transferred in the collision. Furthermore, the ultracold target is extremely well localized, i.e. the position where an interaction takes place is very well known. This is of high importance for time-of-flight (TOF) measurements and the determination of collision cross sections.

Laser-cooled atoms confined in a magneto-optical trap (MOT) have already been used as a target in single-pass experiments for projectiles in the keV range. Charge exchange experiments have been performed at the Kansas State University [Flechard et al., 2001]. They clearly resolved the momentum change of the projectile depending on the initial state of the target and depending on the final state of the projectile. Fraunhofer-type rings are observed by a group at the Ørsted Laboratory in Copenhagen [Poel et al., 2001]. In the collision of trapped sodium and Li^+ at some keV a coherent matter wave of the projectile emerges from a hole with a radius of $\approx 10\,a_0$. The spacing in the expected ring structure is about $\Delta\Theta = 0.008°$. Position sensitive detectors resolved this structures clearly. Collisions between laser-trapped sodium and highly charged oxygen (O^{6+}) are investigated by a group at the KVI in Groningen [Turkstra et al., 2001]. Studies of electron capture processes revealed information sensitive on the impact parameter for multielectron capture processes.

The experiments all used the techniques of COLTRIMS (cold Target RIMS) [Dörner et al., 2000] which is an extension of Recoil Ion Momentum Spectroscopy (RIMS) [Ullrich et al., 1997]. Using RIMS the complete momenta of the ionized atom and the produced electrons can be recorded and thus, the kinematics of the collision can be completely reconstructed. Experiments have shown that the angular efficiency for the recoiled ion is almost 4π and that the resolution for measuring the recoil energy is in the order of 1 meV. It is of great importance that the target atoms are cold, i.e. the measured recoil momentum is not influenced by thermal motion of the target. Therefore, supersonic gas jets have mainly been used in the RIMS experiments. MOTRIMS (Magneto-optical Trap-Target RIMS) is the next step in this development. Laser-trapped atoms provide a target which is not only cold but also the targets position can be controlled very precisely.

For the investigation of collisions with projectile energies in the range of MeV/u we installed a magneto-optical trap for cesium atoms inside the Heidelberg Test Storage Ring (TSR) at the Max-Planck-Institut für Kernphysik. The challenging task of connecting an atom trap to a large-scale facility like the TSR has been demonstrated for the first time. The link between the atom trap and the TSR makes it possible to benefit from the advantages of ultracold atoms (e.g. negligible thermal energy) and of a storage ring (e.g. high event rate). This event rate is interesting in particular for ion beams in the order of MeV/u because the cross sections for collision processes is much lower in comparison to the keV-region.

The cross sections for the interaction of the stored ions and the trapped atoms can be measured directly with a very high precision. From the monitored decay of the atom cloud as a function of the ion flux the cross section can be directly derived without any assumptions. Several measurements investigating collisions between different carbon ions and cesium as well as bare oxygen and cesium have been performed. Total cross sections for this collision processes are determined with high precision. The main contribution to this cross sections is caused by the ionization of the target. The comparison of the measured cross sections and theoretical predictions performed by V.P. Shevelko from the Lebedev Institute in Moscow shows good agreement.

Furthermore, electron transfer from the target to the projectile has been investigated. The expected cross sections for electron capture processes are three orders of magnitude smaller than the ionization cross section because only capture from inner shells of the target is possible. Therefore, a coincidence measurement of the reloaded projectile and the ionized cesium atom is applied. Comparable measurements have been performed e.g. at the GSI using argon and xenon as a target and high velocity uranium (3.6-15.5 MeV/u) as a projectile

[Kelbch et al., 1985, Ullrich, 1994]. The inner shell vacancy caused by the electron capture is filled by Auger-cascades and shake-off processes and so several charge states of the cesium occur after the capture process. The charge states of the cesium ion can be clearly identified in the measurement and the ratio between the coincidence rate and the total ionization rate of the cesium can be determined. Since the total ionization cross section is known the cross section for electron capture can be derived. In addition, a double peak structure has been identified in the TOF spectra. This double peak structure is caused by the different paths of the recoil ion towards the detector. The difference translates in a difference in the time-of-flight and, therefore, gives information about the momentum which is transferred to the cesium ion during the collision.

The ionization rate of the atom cloud depends on the stored ion flux. Therefore, the cloud can be used to monitor the local flux of the ion beam at the position of the cloud. Since the confined atoms provide a very well localized target the cloud can be used for a high precision flux determination. The two-dimensional density distribution of the stored ion beam and thus the transverse profile are monitored directly. The method provides reliable profiles down to ion currents of some nA whereas the restgas BPM [Hochadel, 1994] is already limited to currents of 1 μA. The sensitivity of our measurement can be applied to e.g. dilute, cooled ion beams where the restgas BPM is already limited. The transverse behaviour of laser-cooled or electron cooled ion beams which may undergo the transition to ion beam crystallization [Steck et al., 1996, Eisenbarth et al., 2000, Steck et al., 2001] may now be investigated with a high resolution. In addition, the cloud can be used to monitor the behaviour of high current ion beams. Since the position of the cloud can be controlled very precisely the cloud can be moved towards the halo of the beam and its structure can be studied.

In chapter 2 the properties of the TSR and the trap are introduced. As far as the trap is concerned the experimental setup is described in detail and the compatibility with the TSR is discussed. Special manipulations had to be done in order to make sure that the operation of the storage ring is not disturbed by the atom trap and vice versa. The third chapter shows the detection scheme and the application as a beam profile monitor. The measurement of cross sections is discussed in chapter 4. In chapter 5 a short summary and the future perspectives of the experiment are given.

Chapter 2

Laser-trapped atoms in a storage ring

2.1 The Heidelberg Test Storage Ring TSR

The Heidelberg Test Storage Ring (TSR) [Arnold et al., 1986] is a heavy ion storage ring with a circumference of 55.4 m and a mean vacuum of 5×10^{-11} mbar. Figure 2.1 shows a schematic drawing of the TSR. The 8 dipoles are bending the ion beam trajectories. The 20 quadrupoles focus the stored ion beam. One can store ions with an energy of up to 30 MeV per nucleon starting with protons and ending with bare gold (Au^{50+}). The storable ion currents reach from some mA (e.g. carbon ions) [Grieser, 2002] down to nA. The revolution frequency for ions

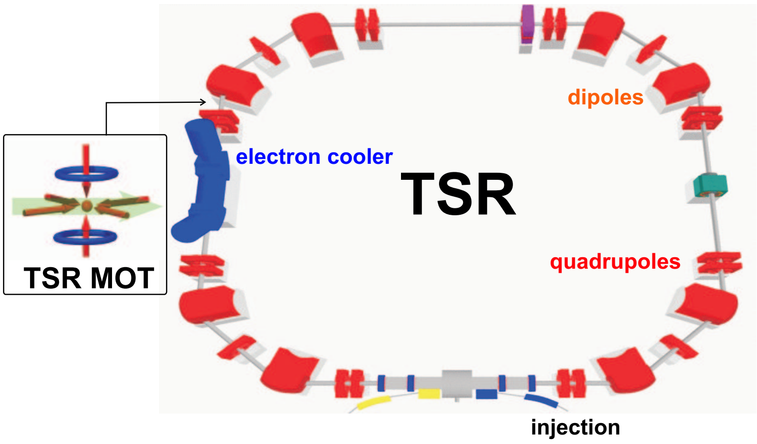

Figure 2.1: *Schematic drawing of the Heidelberg Test Storage Ring (TSR).The dipoles bend the ion beam, the quadrupoles focus it. The atom trap is installed right behind the electron cooler.*

with an energy of some MeV per nucleon is in the order of some 100kHz. Hence, the lifetime of the stored ions is long compared to the flight time for one circle in the TSR (e.g. $1.7\,\mu$s time of flight for C^{6+} with a velocity of $v = 0.11\,c$). The lifetime of the stored ions is mainly determined by collisions with restgas and interactions inside the electron cooler. This lifetime τ depends on the ion species and varies between seconds (e.g. negatively charged D^-: $\tau \approx 3\,\mathrm{s}$) and days (e.g. protons: $\tau \approx 60\,\mathrm{h}$). Inside the electron cooler the ion beam is merged with a cold beam of electrons [Poth, 1990]. Therefore, the electron cooler can be used for two purposes. First, the ion beam is cooled by the merged electron beam, i.e. the momentum spread of the ion beam is reduced. Second, the electron cooler is used as an electron target where e.g. dielectronic recombination, radiative recombination, etc. [Wolf et al., 2000] can be studied.

The target of laser-trapped Cs atoms is installed right behind the electron cooler between a pair of quadrupole magnets and the following dipole magnet (s. Fig. 2.1).

2.2 Properties of the TSR

2.2.1 Beam Profile Monitor

The transverse degree of freedom of the ion beam can be observed with the *beam profile monitor* (BPM) [Hochadel, 1994]. It is possible to measure the horizontal and the vertical density distribution of the ion beam at a given position of the storage ring. Based on these data one can determine the shape and the width of the stored ion beam at this position. The measurement uses the restgas atoms inside the vacuum pipe which are ionized by collisions with the ion beam. The rate of this ionization process depends on the beam density at this position. The ionized atoms are accelerated by an electric field ($|\vec{E}| = 60\,\mathrm{kV/m}$) towards a micro-channel plate detector (MCP) where they can be spatially resolved. The measured distribution of restgas ions corresponds to the shape of the beam. The principle of the beam profile monitor is shown in figure 2.2. One has to consider that the BPM has a limited spatial resolution due to its function principle. Even for an infinitely narrow ion beam one measures a gaussian profile with a limited *resolution width* σ_{res}. This relies on the fact that the recorded restgas ions have a thermal energy of about room temperature. During the drift from the position of ionization to the MCP the thermal motion leads to a smear out of the initial transverse position. Hence, the measured distribution is a convolution of the actual transverse ion beam profile and the resolution width of the BPM. Since the beam profile of a cooled ion beam has also an almost gaussian shape the actual width σ_{real} is determined by quadratic substraction of the measured width σ_{meas} and the

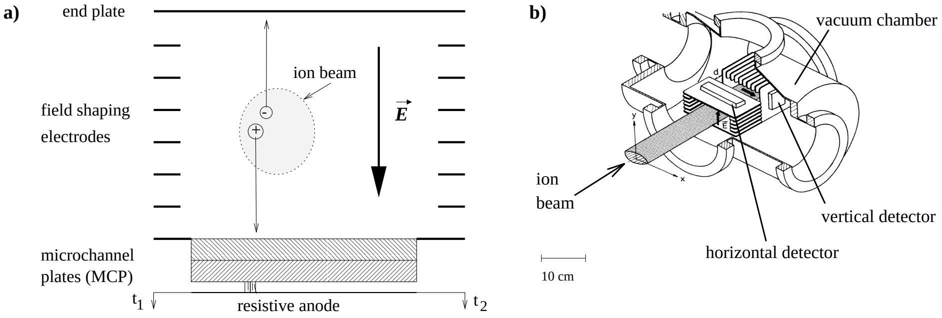

Figure 2.2: *a) Principle of the beam profile monitor. The ion beam ionizes restgas which is accelerated towards the MCP. b) Realization of the beam profile monitor inside the storage ring.*

resolution: $\sigma^2_{\mathrm{real}} = \sigma^2_{\mathrm{meas}} - \sigma^2_{\mathrm{res}}$. The resolution width can be determined by extrapolating the BPM measurements of long-term electron cooling measurements [Lauer, 1999, Beutelspacher, 2000]. Typical values for the resolution widths are $\sigma_{\mathrm{hor,res}} \approx 200\,\mu$m and $\sigma_{\mathrm{ver,res}} \approx 300\,\mu$m.

2.2.2 Recombination Detector

The usage of the electron cooler as an electron target makes it possible to investigate e.g. dielectric recombination [Burgess, 1964, Wolf et al., 2000] induced inside the electron cooler. Since the stored ions change their charge during this process the m/e-separation of the magnetic field of the bending dipole can be used to detect the reaction products. The recombination detector which is installed at the outside of the storage ring is used for the detection of reloaded ions. Figure 2.3 shows the position of the detector inside the TSR. The recombination detector

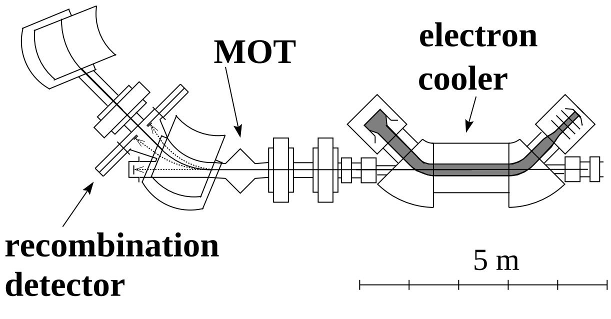

Figure 2.3: *Schematic drawing of the storage ring part including the electron cooler, the magneto-optical trap and the recombination detector.*

consists of a CsI-scintillator which is combined with a photo multiplier.

Since the magneto-optical trap is installed between the electron cooler and the dipole magnet the recombination detector can be used for the target experiments. Using the recombination detector the electron capture process

$$\mathrm{A^{q+} + Cs \rightarrow A^{(q-1)+} + Cs^{q'+}}$$

induced by collisions of the stored ion beam and the ultracold target can be detected. In section 4.2 this measurement will be described in detail.

2.3 The Magneto-optical Trap

The magneto-optical trap (MOT) is an important tool for all kinds of experiments with cold atoms. Since the first realization of a magneto-optical trap in 1986 by Raab et al. [Raab et al., 1987], it has been extremely well investigated [Drewsen et al., 1994a, Townsend et al., 1995, Townsend et al., 1996, Lett et al., 1988]. It is a standard tool used for trapping and pre-cooling e.g. in Bose-Einstein-condensation experiments (e.g. [Anderson et al., 1995, Davis et al., 1995]), for high-precision spectroscopy of trapped atoms (e.g. [Lu et al., 1994, Gwinner et al., 1994, Kasevich et al., 1989]) including photoassociation experiments (e.g. [Abraham et al., 1995, Lett et al., 1995, Fioretti et al., 1998]), for studies on ultra-cold collisions (e.g. [Marcassa et al., 1993, Julienne, 1991, Santos et al., 1995, Schlöder, 1998]) and as an intense source of cold atoms [Lu et al., 1996, Dieckmann et al., 1998]. The principle of the MOT and the parameters characterizing its performance are introduced in this section.

2.3.1 Scattering Force and Optical Molasses

The magneto-optical trap belongs to the group of radiation pressure traps which are based on the spontaneous scattering force. This force arises from subsequent cycles of absorption and spontaneous emission of photons and the momentum transferred to the atom in each of these processes. Therefore, two conditions have to be fulfilled: A closed optical transition is needed to ensure that many cycles of absorption and spontaneous emission are possible and the interaction time of the atom with the light field has to be long compared to the lifetime of the excited state.

We consider as an example a two-level atom with one ground state and one excited state. The atom is assumed to be in resonance with a laser and the atomic transition frequency is ω. If the atom is excited by absorption of a photon, the photon's momentum $\hbar\,\vec{k}$ is transferred to the atom. During the following spontaneous decay to the ground state the atom emits a photon with momentum $\hbar\,\vec{k'}$, where in general $\vec{k} \neq \vec{k'}$.

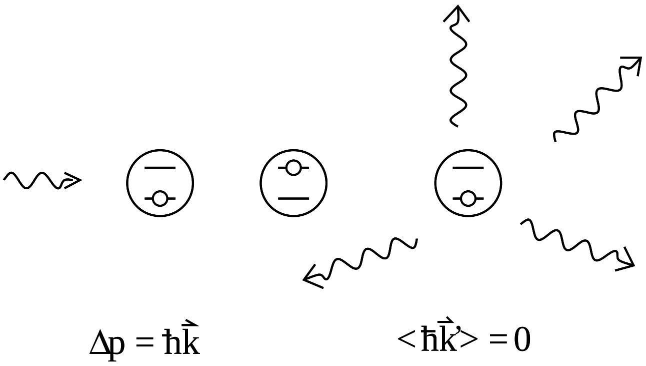

Figure 2.4: *Momentum transfer between photons and a two-level atom.*

After multiple cycles the momentum $\hbar\,\vec{k}$ in the direction of the laser is transferred to the atom several times, whereas the total momentum transfer by the emitted photons averages to zero, $\langle \hbar\,\vec{k'} \rangle = 0$ because the decay occurs with equal probabilities in opposite directions. Therefore, a net force in the direction of the laser beam is exerted on the atom (see Fig. 2.4). The averaged momentum transfer of one cycle is given by

$$\Delta\vec{p}_{\mathrm{sp}} = \langle \hbar\vec{k} - \hbar\vec{k'} \rangle = \langle \hbar\vec{k} \rangle - \langle \hbar\vec{k'} \rangle = \hbar\vec{k} \quad . \tag{2.1}$$

The force exerted on an atom is thus given by the rate of the absorptions multiplied with the averaged momentum transfer:

$$\vec{F}_{\mathrm{sp}} = \hbar\vec{k} \cdot \Gamma_{abs}. \tag{2.2}$$

For a two-level system we obtain

$$\vec{F}_{\mathrm{sp}} = \hbar\vec{k} \cdot p_e = \hbar\vec{k}\frac{\Gamma}{2} \cdot \frac{S}{1 + S + (\frac{2\delta}{\Gamma})^2} \quad , \tag{2.3}$$

where p_e is the probability of exciting the atom, $I_{\mathrm{sat}} = \hbar\,\omega_0^3\,\Gamma\,/(12\,\pi\,c^2)$ is the saturation intensity, and $S = I/I_{sat}$ is the saturation parameter. Γ denotes the natural linewidth, and $\delta = (\omega - \omega_0 + kv)$ is the detuning where v is the velocity of the atom.

Now we consider an atom positioned between two counterpropagating laser beams whose frequencies are detuned to lower frequencies with respect to the atomic transition ω (A laser tuned to $\omega < \omega_0$ is called *red detuned*). Due to the Doppler shift the atom preferably absorbs photons from the laser counterpropagating to its own motion. Therefore, the atom's motion in this direction is damped longitudinally. Because of this viscous damping such a setup where atoms are cooled by two or more counterpropagating pairs of laser beams are called optical molasses. As the force cooling the atoms in an optical molasses is based on the Doppler shift it is often called Doppler cooling force.

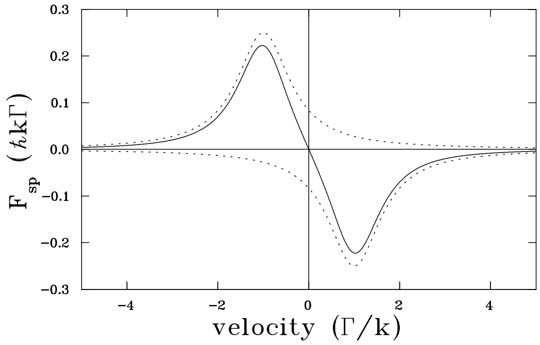

Figure 2.5: *Doppler cooling in the field of two counterpropagating red-detuned laser beams at a saturation parameter of $S = 1$ and a detuning to the red of $\delta = \Gamma$. The force exerted on an atom (solid line) is the sum of the single light forces of the two lasers (dashed lines).*

The Doppler force acting on an atom in a molasses in its dependence on the velocity of the atom along the axis of the laser beams is shown in Fig. 2.5. The dashed lines indicate the force exerted by each of the counterpropagating laser beams and the solid line corresponds to the resulting spontaneous force.

At $v = 0$ the light forces of the two lasers cancel because the atom absorbs photons from each of the laser beams with the same rate. For small velocities the force is purely dissipative and the atom is damped in its motion. The momentum transfer in random directions by absorption and emission is a heating process which limits the temperature achievable with this cooling mechanism. This temperature is the so called Doppler limit and is given by [Metcalf and van der Straten, 1994]:

$$T_{Doppler} = \frac{\hbar\Gamma}{2k_B} \quad . \tag{2.4}$$

However, experiments showed that temperatures far below this limit could be realized in a 3-dimensional optical molasses [Lett et al., 1988]. Explanations for this were found by introducing polarization gradient cooling into the theory [Dalibard and Cohen-Tannoudji, 1989]. This cooling mechanism is based on pumping processes between the magnetic sub-levels of the atom and can be induced by choosing orthogonal polarizations for the counterpropagating laser beams (lin⊥lin or $\sigma^+ - \sigma^-$) or by application of magnetic fields. With polarization-gradient cooling one can prepare atomic samples at temperatures on the order of $\sim 10\,T_{rec}$, where the recoil temperature T_{rec} is given by the recoil impulse the atom gets when it emits a photon:

$$T_{rec} = \frac{\hbar^2\, k^2}{m \cdot k_B} \quad , \tag{2.5}$$

where m denotes the mass of the atom.

2.3.2 Confinement Principle and Properties of a MOT

The magneto-optical trap (MOT) was first realized by Raab et al. [Raab et al., 1987] and rapidly became a widely used tool for various experiments. A schematic drawing of a MOT is shown in part a) of Fig. 2.6. The standard configuration consists of three orthogonal counterpropagating pairs of laser beams and a pair of anti-Helmholtz coils, which produce an axially symmetric magnetic quadrupole field.

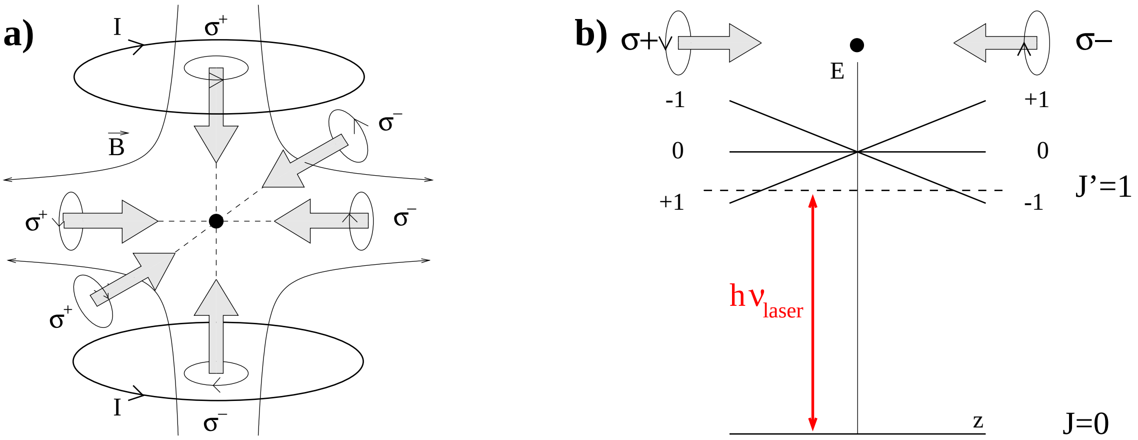

Figure 2.6: **a)** *Schematic drawing of a MOT.* **b)** *Two-level atom with spatially dependent splitting of the magnetic sublevels in the field of two counterpropagating red detuned circularly polarized laser beams.*

The magnetic field induces a spatially varying Zeeman splitting of the magnetic substates and due to the selection rules for circularly polarized light the laser beam with the corresponding polarization pushes the atoms back into the center as depicted in Fig. 2.6 b). This leads to a confinement of the atoms in a small volume in the center of the trapping fields. The velocity dependency of the spontaneous force and the spatially varying Zeeman shift result in a force on the atom which is both cooling and confining.

Loading of a MOT

Entering the intersection region of the MOT beams an atom is captured if its velocity is smaller than the *capture velocity* v_{cap}, and if it crosses the MOT within the *capture radius* r_{cap}. The capture velocity can be estimated using the following consideration [Wallis et al., 1993]:

The Doppler-shift which an atom experiences in the MOT laser beams is given by $\Delta_D = kv$. An atom at the capture velocity experiences the maximum spontaneous force, i.e. the Doppler shift due to its velocity just compensates the detuning of the laser beam: $\Delta_D = \delta$. As $v = k\,v/k$ we thus get for the capture velocity

$$v_{cap} \simeq \frac{|\delta|}{k} \quad . \tag{2.6}$$

Similar considerations lead to an estimation of the capture radius, which depends on the magnetic field gradient $\partial B/\partial z$:

$$r_{cap} \simeq \frac{\hbar\,|\delta|}{\mu_B}\,\frac{1}{\partial B/\partial z} \quad . \tag{2.7}$$

The trap can be loaded with atoms from the low velocity tail of a thermal atomic beam or with particles from the vapour pressure in the apparatus. High loading rates can be achieved by decelerating an atomic beam using e.g. the technique of a Zeeman slower (see e.g. [Prodan et al., 1985]).

Regimes of Behaviour

The behaviour of an atomic cloud in a MOT depends on the density regime the MOT can be associated with. Four different regimes of behaviour can be identified for a MOT cloud: the multiple scattering regime, the two-component regime, the regime of an optically thick cloud, and the temperature-limited regime - the regime of our MOT [Townsend et al., 1995].

In the multiple scattering regime reabsorption of scattered photons becomes important for the behaviour of the trapped atoms. In this regime the trap size depends on the number of atoms and the maximum trap density which is inversely dependent on the intensity in the trapping light field as multiple scattering of photons acts as a repulsive force. The two-component regime is reached when the extension of the cloud is bigger than the region where sub-Doppler cooling mechanisms create a strong force field gradient $\partial F/\partial z$. The trapped cloud then divides into a cold component at the center of the MOT and a hotter one, less localized ‘halo’ around this cold core. The more atoms are in this outer region, the more the system becomes a pure Doppler-theory system. Finally, if density increases further, the trap gets optically thick, and light is scattered only in the outer region of the cloud.

In the temperature-limited regime the diameter of the cloud depends only on the temperature of the atoms and not on their number. Losses in this regime are only due to residual gas collisions. Since the size of the cloud is an important parameter in the measurements described later on it is advantageous to have a constant size of the atom cloud. Therefore, our MOT was designed to operate in the temperature-limited regime to ensure a constant width for all numbers of trapped atoms. The theory of the temperature-limited regime as well as the other MOT regimes is reviewed in detail in [Townsend et al., 1995]. Here, only a short overview over the parameters characterizing the behaviour of a temperature-limited MOT is given.

At small numbers N of trapped atoms the atomic density is low and interactions of the atoms can be neglected. The spatial as well as the momentum distribution are close to Gaussian and can be characterized by the $1/\sqrt{e}$ cloud radii σ_x, σ_y, σ_z and the temperature T. The radius σ_i of a cloud along an axis i (i= x,y,z) is given by the equipartition theorem:

$$\frac{1}{2}\kappa_i\sigma_i^2 = \frac{1}{2}k_BT \quad , \tag{2.8}$$

where k_B is the Boltzman constant and κ_i is the spring constant in the axis i which depends on the field gradient. In a quadrupole magnetic field formed by two coils the field gradient along the coil axis is twice as strong as in the plane parallel to the coils: $\partial B/\partial z = 2\,\partial B/\partial x = 2\,\partial B/\partial y$. Therefore, from $\kappa_z = 2\,\kappa_x = 2\,\kappa_y$ we obtain $\sigma_z = \sigma_x/\sqrt{2} = \sigma_y/\sqrt{2} \equiv \sigma_r/\sqrt{2}$ for the cloud radii.

If the atoms are localized in the center of the MOT where sub-Doppler mechanisms are dominant, a semi-classical analysis shows that

$$\kappa_i = \kappa_0\,\frac{\Gamma}{\delta}\,b_i \quad , \tag{2.9}$$

where κ_0 is a constant of proportionality, and b_i is the dimensionless field gradient $b_i = (\partial B/\partial i)$/(G/cm). Measurements of κ_0 for Cs range from 0.4×10^{-19} N/m to 2.7×10^{-19} N/m, while calculations give values of $\sim$3 $\times$ 10^{-19} N/m as given in [Townsend et al., 1995] and references therein.

At low trap density the temperature in a cesium magneto-optical trap is the same as in an optical molasses created by the same laser-field configuration [Steane and Chowdhury, 1992, Drewsen et al., 1994b]. For detunings larger than a few linewidths ($\delta > 5\,\Gamma$) and light shifts in the range of $0.02\,\Gamma < \Omega^2/\delta < 0.4\,\Gamma$, where Ω is the Rabi frequency ($\Omega = \Gamma\,\sqrt{S/2}$), this temperature varies as

$$k_B T = C_\sigma \hbar \frac{\Omega^2}{\delta} \quad , \tag{2.10}$$

where C_σ is a proportionality constant. The measurements performed by C. Townsend et al. on a magneto-optical trap gave values of C_σ=0.28 $\pm$ 0.05. Inserting equations 2.9 and 2.10 into equation 2.8, one gets for the $1/\sqrt{e}$-radii of the trap:

$$\sigma_i = \sqrt{\frac{\hbar C_\sigma \Gamma}{\kappa_0} \frac{S}{2} \frac{1}{b_i}} \quad . \tag{2.11}$$

The peak atomic number density at the center of the elliptical Gaussian distribution in a temperature-limited MOT is given by

$$n = \frac{N}{(\sqrt{2\,\pi})^3\, \sigma_r^2\, \sigma_z}. \tag{2.12}$$

As σ only depends on the temperature T and not on the number of atoms, the peak density is linearly proportional to N.

The MOT of this Experiment

According to our measurements the MOT presented in these experiments is in the temperature limited regime. The trapping laser frequency is detuned 5 Mhz below the transition frequency of the D2 line which corresponds to $1\,\Gamma \cdot (2\pi)^{-1}$. We reach a number of trapped atoms of $\approx 10^4$ and we measured widths of $\sigma_z \approx 230\,\mu$m and $\sigma_r \approx 290\,\mu$m. This leads to a density of $\approx\; 1 \times 10^9$ atoms/cm^2. The magnetic field gradient is 24 G/cm in the strong axis. The typical lifetime of the trapped atoms is 120 s which is limited by collisions with restgas at a vacuum of 5×10^{-11} mbar.

Intrinsic Loss Processes

Atoms can be lost from a magneto-optical trap either by collisions with residual gas particles or by two-body collisions with other trapped atoms. These atom-atom collision can lead to loss if at least one of the partners is in the upper hyperfine state. Then a hyperfine-changing collision can occur where the atom changes into the lower hyperfine state and the energy difference is transformed into kinetic energy. If this kinetic energy is high enough to lead to atom velocities above the capture velocity, the collision results in the loss of the atom.

The loss of atoms from a MOT can be expressed by

$$\dot{N}(t) \;\;=\;\; -\alpha\, N(t) \,-\, \beta \int_V n^2(\vec{r}, t)\, d^3 r \quad , \tag{2.13}$$

where the coefficients α and β describe the losses by residual-gas collisions and two-atom collisions, respectively, V is the trap volume and $n(\vec{r}, t)$ is the number density of the cloud.

Trapping of Cesium

It was already mentioned that cloud radii of $\sigma \lesssim 50\,\mu$m have been observed in cesium clouds trapped in a magneto-optical trap. In a MOT temperatures of $\sim 10\,T_{rec}$ can be realized and cesium due to its relatively large mass has a very low recoil temperature of only $T_{rec} = 0.2\,\mu$K (see Eq. 2.5). In the temperature limited regime where the equipartition theorem is valid this translates directly into small cloud sizes. In addition, in comparison to the other alkalis or earth-alkalies that can be laser-cooled for cesium already a simple and easy-to handle laser system can provide laser beams with a sufficient frequency stability for our application. Concerning the atomic species for a well localized ultracold target cesium was so the logical choice.

Cesium was discovered by Georg Robert Kirchhoff and Robert Bunsen spectroscopically in Heidelberg in 1860. With an atomic number of $Z = 55$ it is the heaviest stable alkali atom where Cs-133 is the only stable isotope. It has a very low melting point of $28.5°$ C and a boiling point of $670°$ C [Mortimer, 1987]. At room temperature it has a vapour pressure of 2.17×10^{-6} mbar.

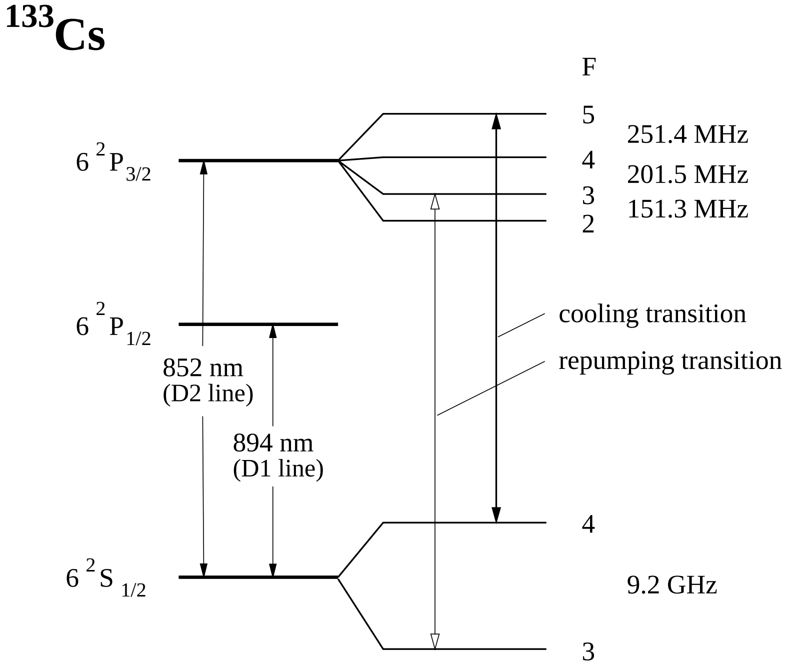

Figure 2.7: *Relevant part of the level scheme of cesium.*
Left hand side: Fine structure splitting, the arrows indicate the wavelengths of the two transitions of the D lines.
Right hand side: Hyperfine splitting of the D_2 line. The ground state splits into two hyperfine states which are separated by 9.2 GHz. The arrows show the transitions which are used for cooling and repumping the atoms in our MOT.

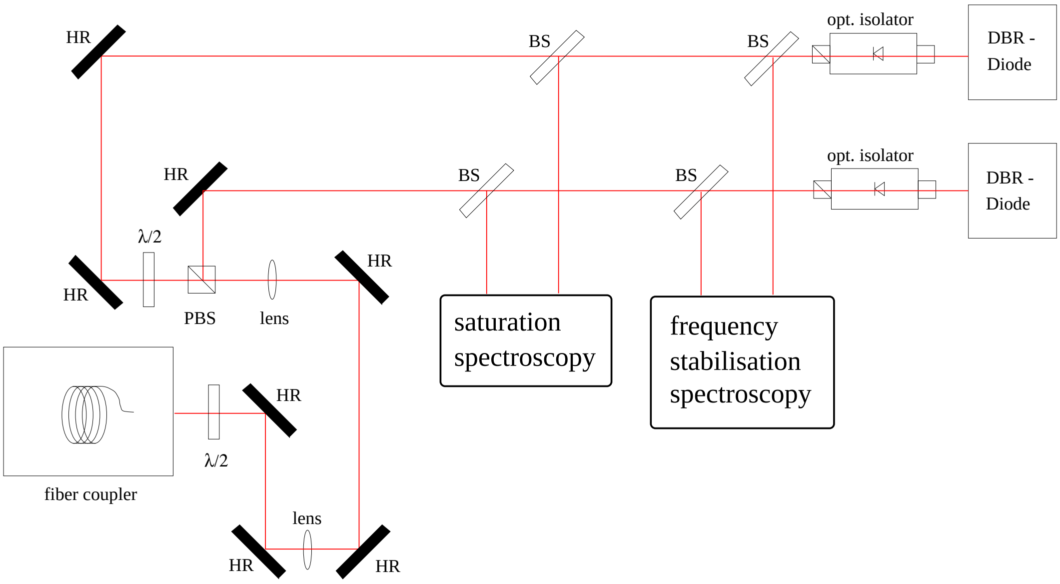

Figure 2.8: *Sketch of the laser system: λ/4 - quarter-wave plates, λ/2 - half-wave plates, BS - beam splitter, PBS - polarizing beam splitter cube, PD - photo diode, HR - mirror.*

Because cesium is an alkali atom it has only one valence electron. Its spin-orbit coupling in the excited state (splitting energy $\hbar\,\Delta'_{FS}$) leads to the well-known D-line doublet $6^2S_{1/2} \rightarrow 6^2P_{1/2}, 6^2P_{3/2}$. The coupling to the nuclear spin of $I = 7/2$ then produces the hyperfine structure of both ground and excited states with energy splittings $\hbar\,\Delta_{HFS}$ and $\hbar\,\Delta'_{HFS}$, respectively. Fig. 2.7 shows the relevant part of the atomic level scheme of cesium.

The lifetime of the excited state is $\tau = 30\,\mathrm{ns}$ which corresponds to a natural linewidth $\Gamma = \tau^{-1} = 2\,\pi \times 5.3\,\mathrm{MHz}$. In Sec. 2.3.1 we pointed out that a closed optical transition is needed for operating a MOT. Due to off-resonant pumping of the atoms via the $F = 4 \longrightarrow F' = 4$ transition with a relative probability of about 0.001 a weak repumping beam is required to pump the atoms back into the closed transition. The arrows on the right hand side in Fig. 2.7 indicate the cooling and repumping transitions. The saturation intensity for the $F = 4 \longrightarrow F' = 5$ cooling transition is $I_{sat} = 1.1\,\mathrm{mW/cm}^2$. This low saturation intensity makes it possible to reach saturation parameters of ~ 20 in the MOT using standard laser diodes. In addition, at the transition wavelength of $\lambda = 852\,\mathrm{nm}$ custom DBR (distributed Bragg reflection) diodes are available which in themselves already show a high frequency stability.

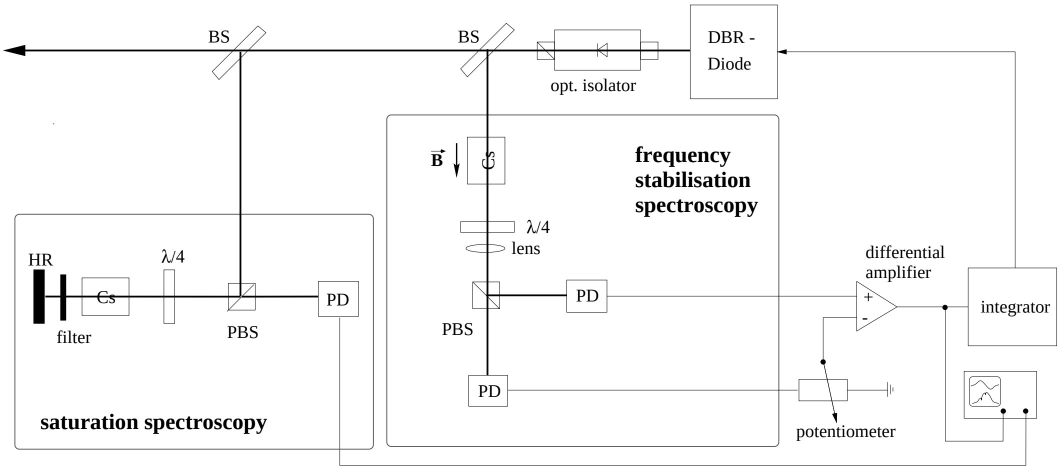

Figure 2.9: *Sketch of the frequency stabilization. The abbreviations are the same as in Fig. 2.8. The rectangles with inscription 'Cs' symbolize glass cells filled with cesium vapour.*

2.3.3 Lasersystem

The laser system for the MOT requires two frequency-stabilized single-mode lasers: one for cooling and trapping, and a second for repumping the atoms into the closed transition. The atomic transition has a natural linewidth of $\Gamma/2\pi = 5.3$ MHz. The setup of the laser system for the MOT is schematically shown in Fig. 2.8. It consists of two diode lasers stabilized to the $F = 4 \longrightarrow F' = 5$ (cooling) transition and the $F = 3 \longrightarrow F' = 4$ (repumping) transition of the cesium D2-line. The laser beams are then superimposed and coupled into a single-mode polarization-maintaining fibre leading to the trap chamber installed in the TSR. With this fibre the laser system can be operated separated from noise and electromagnetic background at the TSR.

The diode lasers used in our setup are two DBR (distributed Bragg reflector) diode lasers (SDL-5712-H1) with a nominal output power of 100 mW. At an operating current of $\sim$ 150 mA we measured $\sim$ 70 mW output power per laser and a spectral width of each laser of $\sim$ 10 MHz (FWHM)[1]. The two diode lasers are frequency-stabilized by Doppler-broadened polarization spectroscopy which takes advantage of the frequency-dependent circular dichroism of cesium vapour to generate an error signal. This locking scheme can be realized by a simple setup.

A beam splitter reflects $\sim 0.1\,\%$ of the linearly polarized laser light into a glass cell filled with cesium vapour which is placed in a longitudinal magnetic field of $\sim$ 100 G. After having passed the cell the laser beam is splitted up into its

---

[1] We determined the spectral width of the lasers by measuring the width of their beating signal and dividing it by $\sqrt{2}$.

circularly polarized components by the means of a $\lambda/4$-plate in combination with a polarizing beam splitter. The two components are detected by photo diodes as shown in Fig. 2.9. As the Zeeman splitting of the hyperfine levels leads to a different frequency shift for σ^+ and σ^- transition the Doppler profiles in the absorption signal are shifted to different frequencies for σ^+ and σ^- probe light. Therefore, by subtracting the two photo diode signals an error signal can be generated. This error signal is fed into an integration loop which controls the injection current of the laser diode. To avoid frequency instabilities caused by temperature fluctuations of the cesium vapour the vapour cells are placed inside a copper block which is temperature-stabilized to $25 \pm 0.1°$ C.

Though the accuracy of the choice of frequency in this locking scheme is limited because the signals used are Doppler-broadened signals, it has the advantage of very robust operation within a wide locking range. This allows us to choose the locking point within $\pm$150 MHz ($\sim$ 30 Γ) with respect to the center of the Doppler profile.

Additionally, we have set up a saturation spectroscopy for each laser that is used for calibration of the Doppler-broadened signals. By sweeping the operating current of the laser diodes with a frequency ramp of up to $\sim$ 10 GHz, we can scan the laser frequency over the Doppler profile. The saturation spectroscopy allows for very accurate frequency tuning with the help of the Lamb dips and cross-over resonances in the Doppler profile as we can display this signal together with the signal obtained from the polarization spectroscopy. Figure 2.10 shows the saturation spectroscopy signal. In figure 2.10 a) the complete frequency scan including the transitions F=4 $\rightarrow$ F' and F=3 $\rightarrow$ F' is shown. b) and c) the saturation spectroscopy signal is identified in detail including the transition dips and cross-over resonances. The Doppler-broadened signal and the saturation spectroscopy signal is shown together in figure 2.11. Using the saturations spectroscopy signal to calibrate the Doppler-broadened signal the lock of the laser can be set to the right frequency. The saturation spectroscopy signal of cesium and the calibration procedure are described more detailed in [Eike, 1999]. A frequency change of 1 GHz corresponds to a change of about 1 mA in the operation current of the laser diode. The frequency of the laser used for trapping and cooling is tuned typically to $\sim$ 8 MHz corresponding to $\sim$ 1.5 Γ below the atomic resonance of the $F = 4 \longrightarrow F' = 5$ transition. The repumping laser is operated at the resonance of the $F = 3 \longrightarrow F' = 3$ transition as we observed a better operation of the MOT with this transition than with the $F = 3 \longrightarrow F' = 4$ transition. Frequency stability is essential owing to the dependence of the fluorescence on the frequency detuning with respect to the atomic transition. By detecting the beating signal of the two lasers with an avalanche photo diode we found that the standard deviation of the center frequency over several days was below 2 MHz (see Fig. 2.12), giving a frequency deviation of $\sim$ 1.4 MHz (0.25 Γ) for each laser. Considering the

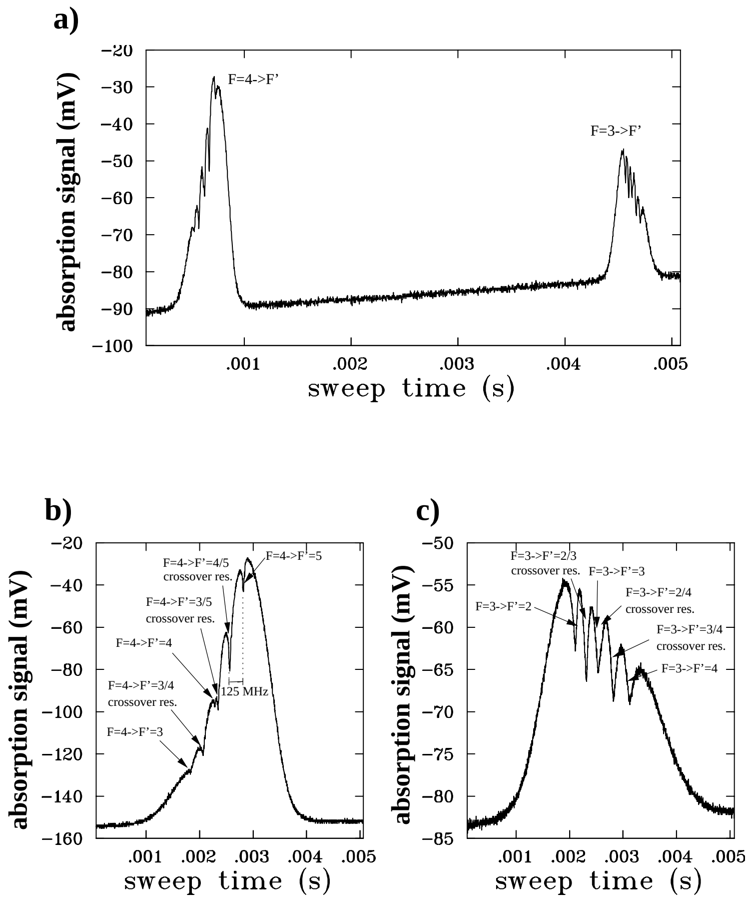

Figure 2.10: *Signal of the saturation spectroscopy.a) shows the complete scan including the spectroscopy signal for the levels F=4 and F=3. b) Saturation spectroscopy of F=4 with identified transitions. c) Saturation spectroscopy of F=3 with identified transitions.*

operation of a MOT this stability is more than sufficient.

As a polarization-maintaining fibre has two axes on which the polarization is maintained we superimposed the linearly polarized laser beams in a way that their polarization planes were orthogonal before we coupled them into the fibre (FS-PM-4621, Thorlabs). The use of a fibre allows us to place the lasers and the stabilization system in a secluded room near the storage ring hall where the effects of noise and electromagnetic background can be reduced. In addition, the use of a single-mode fibre offers the advantage of spatially filtering the laser beams and it provides better stability and day-to-day reproducibility of the alignment of

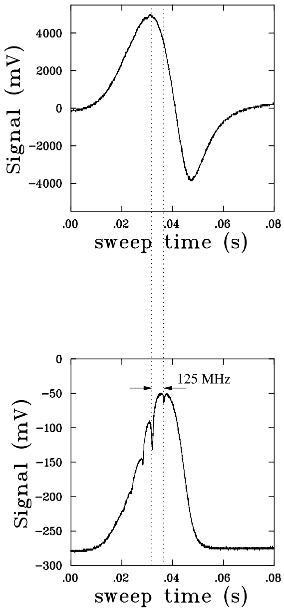

Figure 2.11: *Doppler-broadened signal and saturation spectroscopy signal for the transition F=4 → F'.*

the beams. Our fibre is connectorized with FC couplers at both ends. We use a collimation package with a focal length of f=4.5 mm to couple the laser beams into the fibre and another package with f=11 mm at the output (F220FC-B and F230FC-B, Thorlabs). For optimum mode matching we have set up a telescope consisting of lenses with focal lengths of 500 mm and 300 mm. The second lens is attached to a translation stage for optimization of the adjustment of the telescope. Behind the output of the fibre, the cooling laser beam has a power of $\sim$ 25 mW and the repumping beam has a power of $\sim$ 10 mW. The higher loss is caused by the more elliptic profile of the repumper beam. The beam diameters are 2.1 mm.

Behind the output coupler a combination of a λ/2-plate and a polarizing beam splitter cube is used to split a variable part of the laser beam off to the atomic beam deflection which is explained in Sec. 2.4.1. Due to the nature of the used splitting technique nearly all of the repumping laser power is splitted off the main beam. As repumping is needed only once per thousand cooling cycles, the repumper power of a few mW remaining in the main beam is still more than sufficient for the MOT.

The main beam is then widened by a factor of six using a telescope consisting of two lenses with f=50 mm and f=300 mm before it is split up into three beams of equal power. Each beam is then widened a second time by a Kepler telescope before entering the main vacuum chamber. The first concave lens of this telescope has a focal length of f=-50 mm while the second convex lens has a focal length of

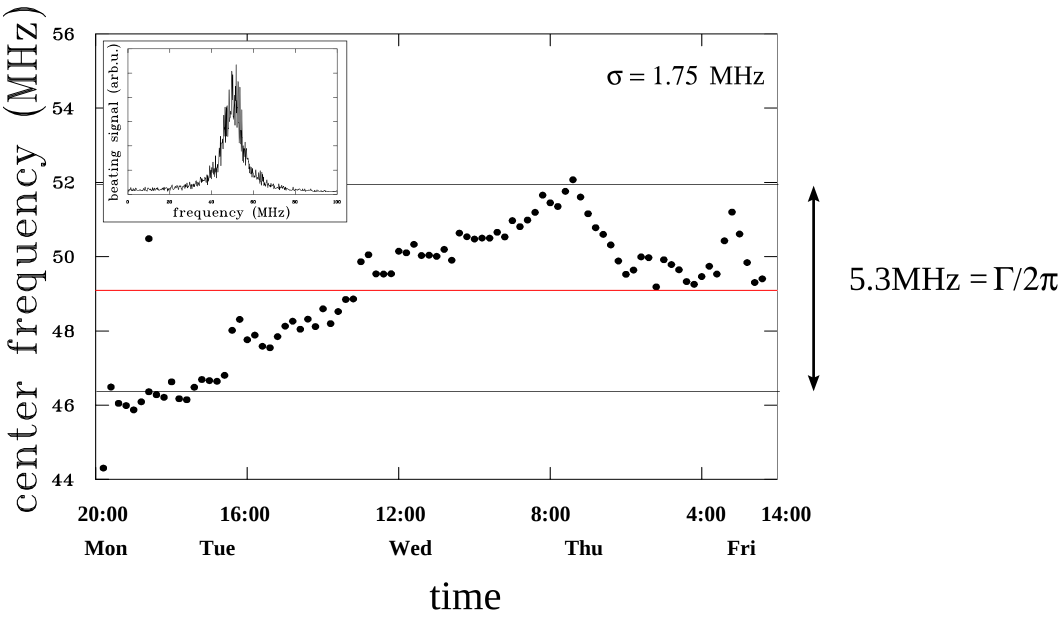

Figure 2.12: *Long-term measurement of the stability of the laser frequencies. A part of the superimposed laser beams was split off and focussed onto a photo diode, and the beating signal (see inset) was recorded once per hour over a period of 5 days. The center frequency shows a deviation of less than 2 MHz for both lasers.*

f=100 mm resulting in a widening of the beam by a factor of two. The resulting beam has a diameter of d=25.2 mm. By widening up the beam in two stages we could use optics of 1 inch size as the beam is only widened to its design diameter directly before it enters the MOT chamber. In order to be able to use a 1 inch sized mirror for the back reflection of the beam another Kepler telescope of the same specifications was put between the window and the back reflecting mirror.

2.4 Vacuum System

One of the main tasks for the design of the trap was the construction of an ultra-high vacuum (UHV) system that could provide the required 5×10^{-11} mbar even during operation of the atomic beam loading the trapped atom cloud. The standard measures we took were the choice of all-metal components, the use of specially treated steel (316LN) for the components that will be connected to the ring vacuum, and the use of all-metal sealing gaskets in all parts of the vacuum system. Further measures had to be taken especially in the design of the atomic beam section. Those measures are explained in detail in the first part of this section. In the second part the main vacuum chamber which is implemented into the storage ring is described.

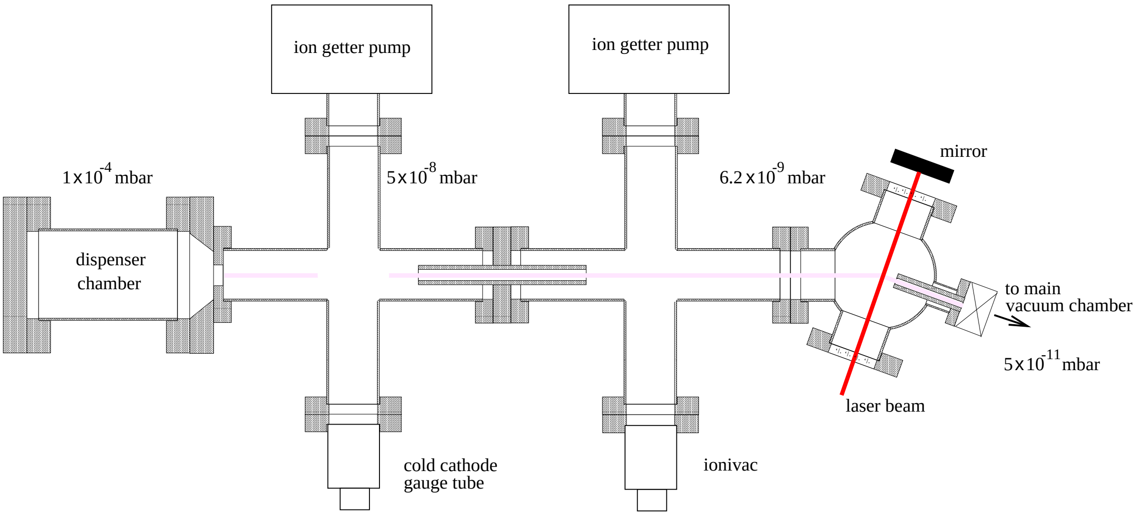

Figure 2.13: *Schematic drawing of the atomic beam section.*

2.4.1 Atomic Beam Section - Loading Concept

In order to realize a vacuum compatible with the storage ring vacuum of 5×10^{-11}mbar the atomic beam section is of special interest. An overview over the whole atomic beam section is given in Fig. 2.13.

A double differential pumping section separates the oven chamber - which is at roughing pressure ($\sim 10^{-4}$ mbar) - from the ultra-high vacuum of the main chamber. In addition, we realized a loading concept that allows only those atoms to enter the trap chamber that can be caught by the magneto-optical trap. We therefore included a velocity filter in the form of a deflection section where only the slowest cesium atoms are deflected into the main vacuum chamber. The details of our loading concept are given in the following subsections.

Cesium Source

The oven which provides the atomic cesium beam is a tube of 63 mm diameter covered with two CF flanges at its ends. The oven is fed by so-called dispensers (CS/NF/8/25 FT10+10, SAES Getters). They are metal strips in which cesium is chemically bound to a getter material. After activating the metal strips with a current of at least 7 Ampères for some minutes cesium is dispensed into the oven chamber by feeding the stripes with a permanent current of typically 4 A. Four feedthroughs of 4 mm diameter are built into one of the flanges. The feedthroughs are used for applying the current and they serve as supports for the holders of the dispensers. The holders are made of flat ceramic strips to provide electrical isolation from the oven. The dispensers are connected in series by small copper plates which are screwed to the ceramic strips. The dispensers are devided into two groups of 4 dispensers. This division ensures continuous operation if one group is exhausted. The cesium pressure inside the oven can be controlled by Doppler-spectroscopy using a suitable laser beam. The laser passes the oven through two CF16 viewports which are attached to the dispenser chamber. We decided to feed the oven with such dispensers because of the easy and safe handling of the cesium in this form, as it is gettered and does not react in air before activation. Moreover, by switching on and off the dispenser current one can control the evaporation of cesium, i.e. cesium is only fed into the oven chamber during operation time.

The nozzle of the oven is formed by a copper channel of 30 mm length and 1.5 mm diameter which is located in the middle of the second flange. The dimensions of the channel ensure that the mean free path of the cesium atoms at the operation temperature of the oven (typically 120° C) is larger than the length of the channel. Furthermore, it is important that the channel is as small as possible to provide low conductance because the pressure in the oven chamber is given by the saturation pressure of cesium, which is as high as $\sim 2 \cdot 10^{-3}$ mbar at 120° C.

Differential Pumping Sections

The atomic beam section includes two sections of differential pumping. The first is formed by a cross with an additional flange for the connection to the turbo pump used for roughing (V70LP, Varian). During normal operation, this connection is shut off by a right angle valve (DN40CF, Varian). The additional flanges allowed us to connect a cold cathode transducer (Inverted Magnetron, Varian), as well as the ion getter pump (VacIon Plus 25, Varian) pumping this section. A small copper channel of 12 cm length connects this first differential pumping section to another cross. The channel is divided into three parts of different diameters to cope with the trade-off of having as high a resistance as possible and of avoiding to cut too many atoms out of the atomic beam. The diameters range from 6 mm to 10 mm.

At the second cross another ion getter pump of the same type as at the first cross as well as a vacuum gauge tube (UHV24 Ionization Gauge Tube, Varian) are installed. This cross is connected to the deflection chamber which will be explained in the next subsection. From the deflection chamber another copper channel with a diameter of 6 mm and a length of 55 mm leads to a gate valve (DN16CF all-metal, VAT) connecting the atomic beam section to the main vacuum chamber. This valve was installed to separate the atomic beam section from the ring when it is not in operation especially in order to enable us to change the dispenser strips in the oven without ventilating the main chamber.

The vacuum pressure p that can be achieved using differential pumping is given by

$$p = \frac{p_0}{R\,J} \quad , \tag{2.14}$$

where p_0 is the pressure in the preceding chamber, R is the resistance of the tube connecting the chambers, and J is the pumping speed in l/s of the pump attached to the chamber. The resistance R for a long tube is given by [O'Hanlon, 1988]

$$R\,/\,\mathrm{sl}^{-1} = 3.28 \times 10^{-2}\,\frac{l}{r^3}\,\frac{\mathrm{cm}^3}{\mathrm{cm}}\sqrt{\frac{M\,/\,\mathrm{u}}{T\,/\,\mathrm{K}}} \quad , \tag{2.15}$$

where l is the length and r is the radius of the tube, M denotes the atomic mass, and T symbolizes the absolute temperature. For cesium ($M = 133$) at room temperature, we get $R = 2.19 \times 10^{-2}\,l/r^3\,\mathrm{cm}^3/\mathrm{cm}$. With the parameters given for the oven nozzle and assuming a pressure of $\sim 2 \cdot 10^{-3}$ mbar in the oven, Eq. 2.15 gives a resistance of 155.7 s/l leading to a vacuum of 6.5×10^{-7} in the first differential pumping section. Here, we made a rather low assumption of 20 l/s for the ion getter pump, while the real pumping speed is probably higher. Measurements with the cold cathode showed that the vacuum pressure even while the atomic beam is operating is on the lower limit of its linear range of measurement which is $\sim 1 \times 10^{-8}$. For the tube leading to the second section the parts with different diameters add up as they are connected in series. One calculates a resistance of 5.3 s/l for the tube connecting the differential pumping sections and 4.5 s/l for the one leading to the main vacuum chamber. With the pumping speeds of the second 25 l ion getter pump and the pumps attached to the main vacuum chamber (see Sec. 2.4.2) this is enough to reach a vacuum of $\sim 5 \times 10^{-11}$.

Selection of Slow Atoms

As already shown the differential pumping section in itself is sufficient to prevent a deterioration of the ring vacuum by the pressure of the cesium oven. However, as it is desirable to minimize any effect of the atomic beam on the performance of the storage ring, we included a velocity filter as described in [Witte et al., 1992] into our concept, that allows us to separate the atoms with velocities below the capture velocity of the MOT v_{cap} (see Sec. 2.3.2 and Eq. 2.6) from the fast, hot part of the Maxwell distribution. The atomic flux into the chamber is thus reduced to $\sim$1% of the initial atomic beam.

As mentioned above after the fibre a fraction of the superimposed laser beams is split off before the beam is widened and split up into the three beams forming the light field of the MOT. This separated fraction is expanded to a diameter of 6 mm in a 1:3 telescope crosses the atomic beam under an angle of 72° in the last differential pumping section and then is retroreflected to form a standing wave.

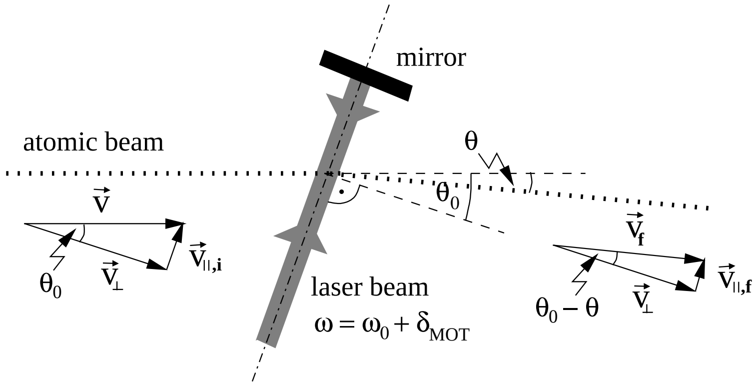

Figure 2.14: *Schematic drawing of the velocity filter realized by a velocity selective atomic beam deflection, introducing the symbols used in the calculation of the deflection angle. Parallel (*$\|$*) and perpendicular (*$\perp$*) refer to the laser beam axis.*

As the laser beam used here has the same frequency detuning $\delta = \omega - \omega_0$ from the transition frequency ω_0 as the beams used for cooling and trapping of the atoms in the MOT the same Doppler force as described in Sec. 2.3.1 for an optical molasses is exerted on the atoms while they cross the laser beam. It leads to a damping force $F = -\alpha v_{\|}$ on the velocity component $v_{\|}$ of the incoming atoms at velocity v which is directed parallel to the axis of the standing wave. For clarification of the symbols used see Fig. 2.14. By the damping of $v_{\|}$ the atoms are deflected towards the axis perpendicular to the standing wave. The angle of deflection of each atom depends on its interaction time with the laser field. Since slow atoms have a longer interaction time they can be deflected further than fast atoms. We will now assume a deflecting laser beam with saturation parameter $S = I/I_{sat} \ll 1$ where I is the intensity of the beam, and I_{sat} = 1.1 mW/cm^2 is the saturation intensity of the cesium D$_2$-line. If $kv \ll \delta$ and $kv \ll \Gamma$ where k is the value of the wave-vector of the laser beam, the damping constant α of such a beam is given by [Witte et al., 1992]

$$\alpha(S) = 4\hbar k^2 S \frac{4\pi(\delta/\Gamma)}{(1 + (4\pi\delta/\Gamma)^2)^2} \quad . \tag{2.16}$$

We assume that the velocity component $v_\perp$ perpendicular to the molasses beams is not altered in the process, the interaction time of an atom with the standing wave is given by $t = d/v_\perp = d/v \ \cos(\theta_0)$ where d is the diameter of the laser beam and $\theta_0 = 18^\circ$ is the angle between the normal to the laser beam axis and the axis of the incident atomic beam. The velocity component $v_{\|}$ is damped by a factor of $\exp -(\alpha/m)\, t$ resulting in a deflection angle of

$$\theta(v) = \theta_0 - \arctan \frac{\sin\theta_0 \, e^{-\frac{\alpha(S)}{m}\, t(v)}}{\cos\theta_0} \quad . \tag{2.17}$$

This effect can be used to generate a velocity filter. The copper channel leading to the main vacuum chamber is arranged in an angle of 18° with respect to the direction of the incoming atomic beam, allowing only atoms which are fully deflected onto the axis perpendicular to the laser beams to reach the main chamber. All other atoms are dumped on the wall of the deflection chamber. By adjusting the intensity of the deflecting laser beam, one can adjust the force exerted onto the atoms and thus the maximum velocity, an atom may have to be deflected onto this axis. With a laser beam of 6 mm diameter corresponding to the diameter of the copper tube, a laser intensity of a few milliwatt results in a deflection of atoms with velocities up to a few times 10 ms^{-1}. In this way the demand for a loading concept which allows only atoms at velocities $v < v_{cap}$ to reach the main vacuum chamber can be fulfilled by an appropriate choice of the intensity of the deflecting laser beam. The magnetic stray fields of the nearby quadrupole and dipole in the TSR induce magneto-optical forces inside the deflecting section comparable to a magneto-optical trap. These forces change with the magnetic stray field and are not under control. It turned out that this magneto-optical forces decrease the loading flux into the trap. Nevertheless, it is possible to change the adjustment of the deflecting laser in a way that enough atoms are available for loading the trap. But this adjustment deviates from the situation shown in figure 2.13. The angle between the laser beam and the channel leading to the storage ring deviates from 90° and the adjustment has to be done iteratively. In addition, the loading flux varies in time and changes for different magnet field configurations. Therefore, the deflecting section is surrounded by a mu-metal shielding which suppresses the magnetic field inside the deflecting section. This shield ensures that the flux is kept constant and independent from the magnetic field. Furthermore, the adjustment of the laser beam becomes much easier. It has to be adjusted only once according to the situation shown in figure 2.13.

Loading of the Trap

The loading flux has been measured for several currents of the nearby dipole magnet. The results are shown in figure 2.15. The dipole current was adjusted to currents between 0 A and 600 A in steps of 200 A. The loading flux has been stopped by blocking the laser which deflects the cesium atoms inside the loading section using a mechanical shutter. Then the shutter is opened and the atoms are deflected into the storage ring. The loading of the trap is recorded by detecting the fluorescence of the trapped atoms with a CDD-camera. Figure 2.15 shows that loading the trap is not interfered by the magnetic field of the dipole magnet anymore. It

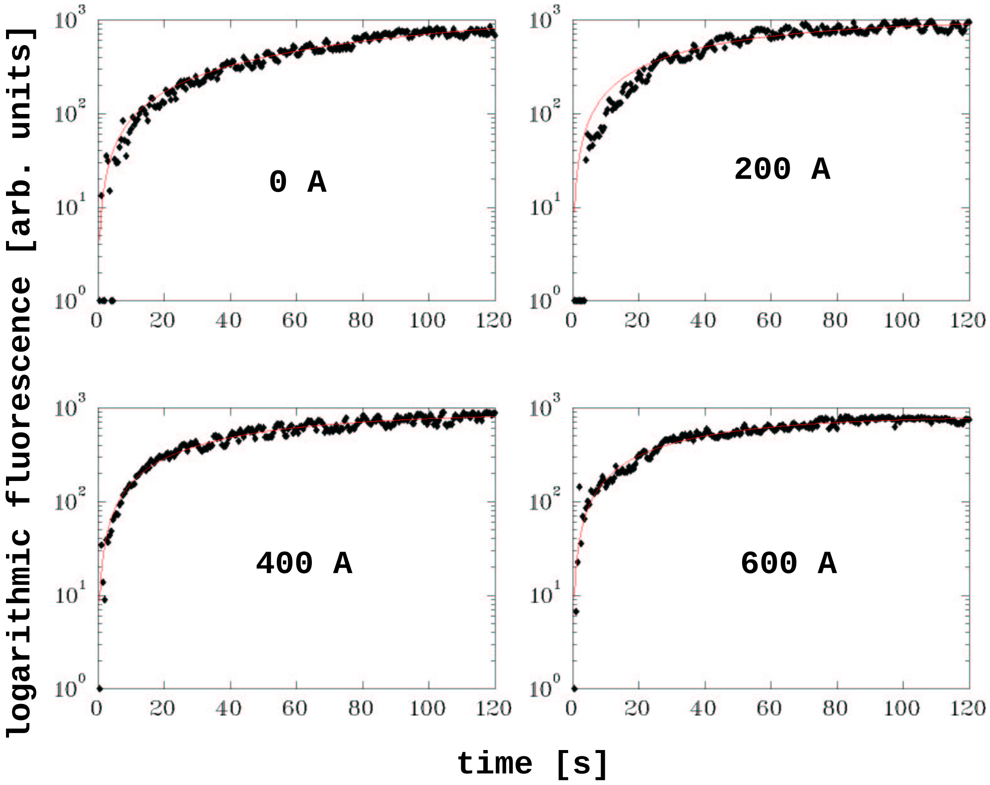

Figure 2.15: *Loading of the trap at different dipole currents. The trapping of atoms is investigated by recording the fluorescence of the trapped atoms with a CCD-camera.*

becomes clear that the magnetic shielding mentioned above suppresses the stray fields very efficiently. The number of trapped particles is described according to

$$N(t) = \frac{\mathrm{L}}{\Gamma} \cdot \left(1 - e^{(-\Gamma \cdot t)}\right) . \tag{2.18}$$

N(t) is the fluorescence recorded by the CCD-camera in arbitrary units ('counts'). The quadratic losses inside the trap are neglected in this description. This signal is proportional to the number of trapped atoms. Γ is the decay rate of the atom cloud in s^{-1}, L the loading rate in counts $\cdot\, \mathrm{s}^{-1}$. From a fit to the data in figure 2.15 a loading rate form 14 - 19 counts $\cdot\, \mathrm{s}^{-1}$ can be extracted. Since the fluorescence counts of the CCD-camera are not calibrated, the loading rate cannot be expressed in atoms $\cdot\ \mathrm{s}^{-1}$, yet. A rough estimation can be made by using measured values from the test setup [Luger, 1999]. These measurements indicated a number of trapped atoms in the order of 3×10^4. Assuming this as the particle number which corresponds to the maximum fluorescence in figure 2.15 one calculates a loading rate of ≈ 500 atoms$\cdot$s^{-1}. This rate would be one order of magnitude lower than the loading rate measured in the test setup.

2.4.2 Main Vacuum Chamber

The main vacuum chamber was designed not to influence the acceptance of the storage ring which is the range in which trajectories of stored ions can run without colliding with the walls. It therefore had to provide a free diameter of at least 200 mm in the horizontal and 80 mm in the vertical direction. To realize this we chose a vertically flat cylinder as the base shape for the chamber. Figure 2.16 shows a schematic drawing of the trap chamber. The whole chamber has 12 flanges of which ten are arranged in the horizontal plane. At the top and bottom of the chamber two DN 100 CF flanges are integrated on which the viewports for the vertical laser beam are mounted. In addition, they can be used for observation of the MOT as their diameter is much larger than that of the laser beams. All tubes attached to the side of the chamber are aligned with their center axis towards the chamber center. Four of the flanges (DN 40 CF) serve as viewports for the horizontal laser beams. To one flange (DN 16 CF) the atomic beam section is attached, while the one located opposite to this one leads to the pumps installed at the main chamber (DN 63 CF). Another DN 63 CF flange is used for the installation of the micro channel plate (MCP) needed for the transversal ion beam detection and on a third DN 63 CF flange a viewport for additional optical detection is mounted. All viewports are anti-reflection coated for a wavelength of 852 nm. At both ends of the chamber flat tubes are attached on which DN 200 CF-flanges are installed.

The pumping section consists of a sublimation pump (USP 063, Balzers) and a 60 l ion getter pump (StarCell VacIon 60, Varian) which are attached to

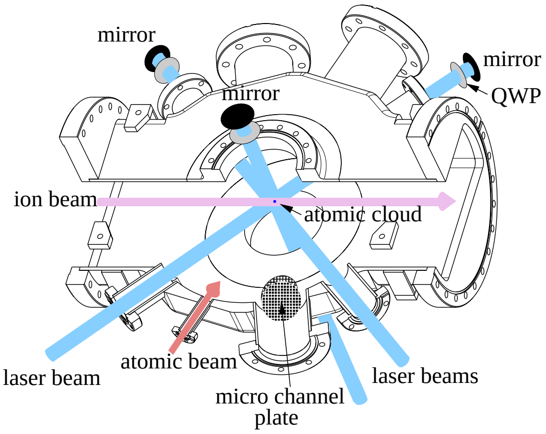

Figure 2.16: *Schematic drawing of the main vacuum chamber installed inside the TSR (QWP: Quarter wave plate).*

a DN 63 CF double cross. This is the standard combination used for pumping UHV-setups as the two types of pumps complement each other with respect to their pumping speeds for the atomic species contained in the residual gas. On the other flanges of the double cross a vacuum gauge tube as used at the storage ring and another anti-reflection coated viewport are mounted. The viewport is positioned directly opposite to the atomic beam section and gives the opportunity e.g. of shining in an additional decelerating laser beam in a Zeeman-slower setup for applications of the MOT as a scattering target where high loading rates would be needed to create a sufficient density.

2.5 Position Control of the Atom Cloud

In our setup, a superposition of three magnetic fields is needed. The first field is the magnetic quadrupole field confining the atoms in the MOT. It is created by a pair of coils which are situated on top and beneath the main chamber in an anti-Helmholtz-like configuration. Each coil consists of 300 turns of lacquered wire with a diameter of 2 mm. Their mean radius is 11 cm and their centres are 14 cm apart. Both coils are water-cooled and can be removed for bakeout. During our experiments the current applied to the coils was 8 A corresponding to a field gradient of $\sim$24 G/cm. This gradient is an order of magnitude below the gradients of the focusing fields of the storage ring magnetic field structure, and its slight focusing effect on the ion beam can be easily compensated by the correction magnets included in the ring.

Two additional fields are needed to move the cloud of trapped atoms within the capture volume defined by the laser beams. As described in Sec. 3.3.4 this is achieved by moving the magnetic field zero using additional homogeneous fields in the horizontal and vertical direction. These fields are created by two pairs of coils (shifting coils) which are arranged in a Helmholtz-like setup. The two coils for the vertical displacement of the cloud are situated on top and beneath the quadrupole field coils, respectively. They each consist of 195 turns of 1.5 mm thick wire. Their centres are 22.5 cm apart and they have a radius of 9.7 cm. They are attached to the MOT field coils. The coils for horizontal displacement are attached to the MCP flange tube and the viewport flange tube on the opposite side, respectively. They consist of 65 turns of a 3 mm thick wire which is wound directly around the tubes and therefore cannot be removed for bakeout. Therefore, a special wire had to be used that can endure the 250°C which is the standard peak temperature for bakeout of the TSR. The mean distance of the coils is 19.4 cm and their radius is 5 cm.

Influence of the Magnetic Stray Fields of the Nearby Magnets

In addition to the static field of the shifting coils the stray fields of the nearby quadrupole and dipole magnet influence the position of the magnetic zero of the trap field, too. The stray fields of the dipole magnet have to be compensated by the vertical shifting coils (s.Fig. 2.17). The hatched area indicated the accessible region of the atom cloud. The vertical offset current is plotted versus the dipole current for several quadrupole currents (0 A, 100 A, 200 A, 300 A). 2 A of the vertical offset current correspond to a shift of $\approx$ 1.6 cm. The region which can be accessed with the atom cloud does almost not change for different dipole currents. Since the magnetic field lines of the stray field of the dipole cross the trap chamber in vertical direction a horizontal compensation is almost not necessary (s. Fig. 2.18). The influence of the quadrupole's stray field is almost negligible up to a current of 300 A. Although the atom cloud disappears at a current of 400 A this has not been investigated further since quadrupole currents higher than 300 A have not been used in the experiment so far.

2.5.1 Backaction on the Closed Orbit of the Stored Ion Beam

The additional fields of the shifting coils give a tiny kick to the stored ion beam due to the Lorentz-force. This momentum kick causes only a small deflection angle in the order of 1 μrad per pass but repeated with a frequency of some 100 kHz it causes a substantial displacement of the closed orbit. The displacement can be monitored by the restgas beam profile monitor. The open circles in figure 2.19 show the horizontal deviation of the closed orbit depending on the vertical position of the magnetic zero. The effect is compensated by an additional pair of

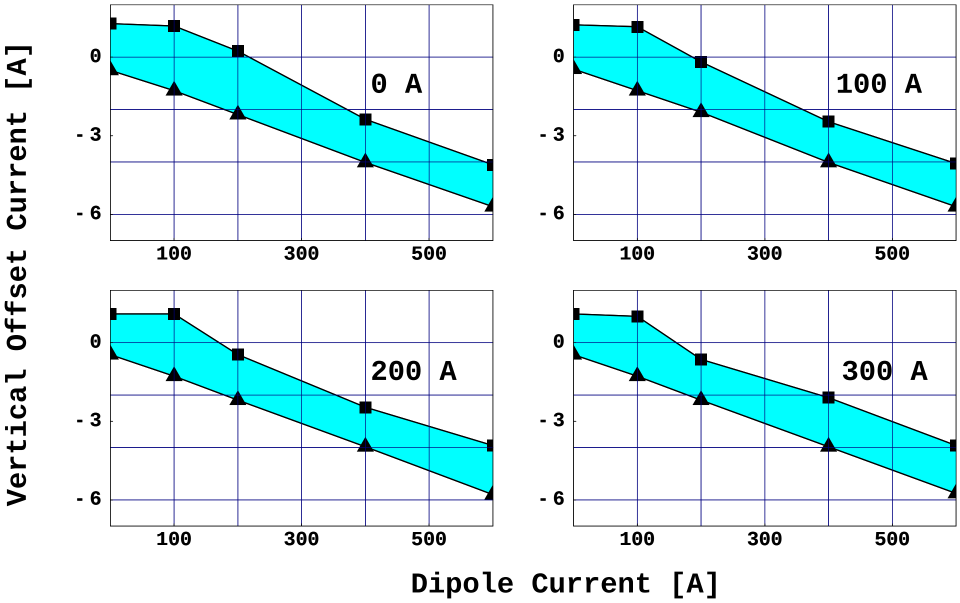

Figure 2.17: *Influence of the nearby quadrupole and dipole magnet on the magneto-optical trap. The vertical offset current is plotted versus the dipole current at several quadrupole currents. The hatched area indicates the accessible region of the atom cloud.*

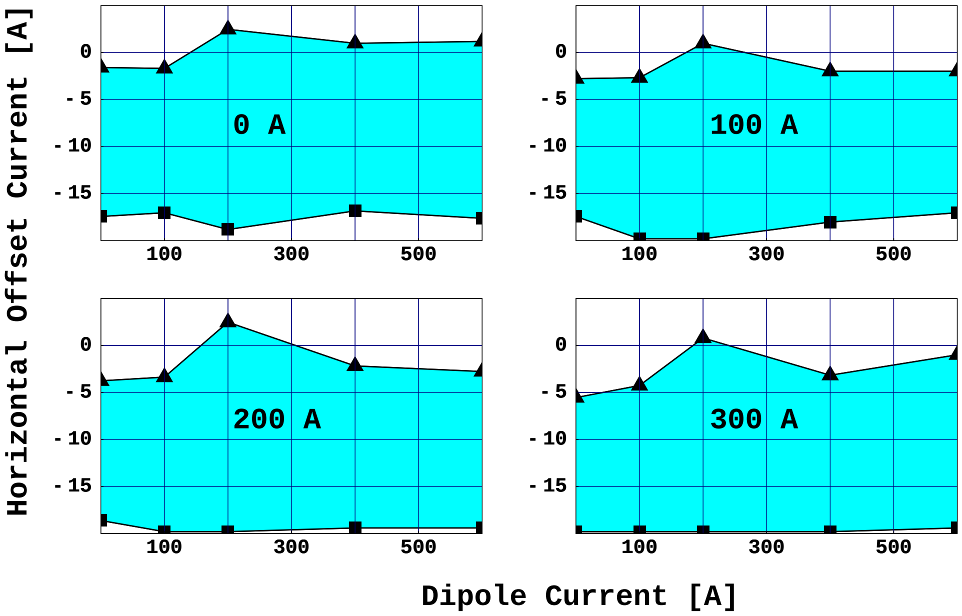

Figure 2.18: *The horizontal offset is plotted versus the dipole current at several quadrupole currents. 20 A horizontal offset current correspond to ≈ 1.6 cm.*

coils (compensating coils) which is installed 50 cm in front of the MOT chamber. Since the cloud can be moved in the horizontal and in the vertical plane, two pairs of coils are needed for the complete compensation of the effect shown above. Each of the coils consist of 380 turns of lacquered wire with a diameter of 2 mm. Their mean radius is 7.5 cm and the centres of each pair are 32 cm apart. The ratio between the the shifting coils and their corresponding correction coils is fixed and was aligned in the following way: The displacement of the stored ion beam caused by the shifting coils is monitored by the restgas beam profile monitor. The current of the compensation coils then is adjusted until the displacement is cancelled at the position of the restgas beam profile monitor. This method works fine if the displacement of the ion beam passed no turning point. Otherwise the compensation would go into the wrong direction. The procedure has to be repeated several times until it converges. It is sufficient to use one pair of coils for the compensation of each direction because the tune Q of the ion beam inside the TSR is always between 2-3. Therefore, the phase of the betatron oscillation [Wille, 1996] changes only slightly between the compensating and the shifting coils. The full circles in figure 2.19 show clearly that the combination of this two pairs of coils suppresses the deviation of the closed orbit. The deviation of the closed orbit in the outermost regions is caused by the fact that the power supplies of the compensation coils are limited for large shifts of the magnetic zero. Since

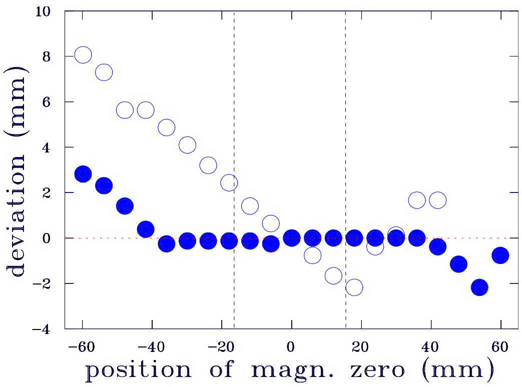

Figure 2.19: *The shift of the magnetic zero displaces (open circles) the closed orbit from its original position (horizontal dashed line). Additional coils invert this effect. Now the magnetic zero can be moved without disturbing the closed orbit (full circles). The vertical dashed lines indicate the region where the atom cloud can be positioned.*

the vertical dashed lines in figure 2.19 indicate the region where the cloud can be positioned, it is clear that the limitation of the power supplies is no problem for the function of this concept. The accessible region corresponds to the overlap of the laser beams with a diameter of about 20 mm.

Chapter 3

Laser-trapped Atoms as a Beam Profile Monitor

3.1 Ion Detection Scheme

The ion detection scheme consists of three main parts which are shown in figure 3.1: the MCP, a lens electrode system and a ring electrode. The MCP has two stacks in chevron configuration with an active diameter of 25 mm [Wiza, 1979]. It is insensitive to the stray magnetic fields of the nearby quadrupole and dipole magnet of the TSR. A voltage of -2 kV is applied to the front electrode of the MCP. The rear anode is set to +150 V (s. Fig. 3.1). The principle of the microchannel plate is depicted in figure 3.2. Ions which hit the micro channels plate create secondary electrons inside the channels. These electrons are accelerated inside the

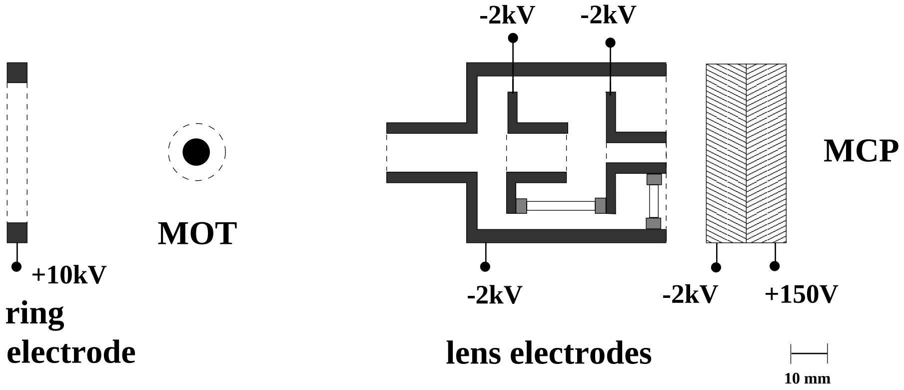

Figure 3.1: *Schematic drawing of the MCP and the lens electrode system which accelerates the ions towards the MCP. The electrodes have cylindrical symmetry (the distance between the push electrode an the lens electrodes is not scaled).*

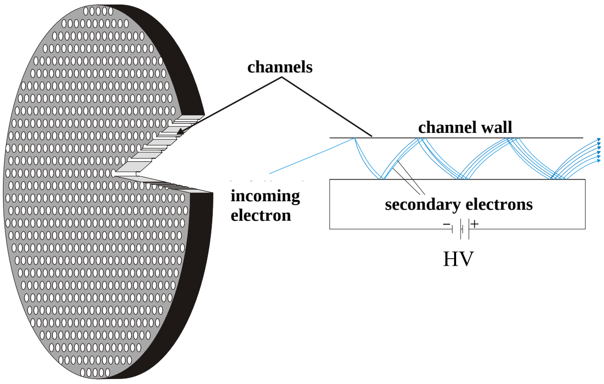

Figure 3.2: *Schematic drawing of the principle of a MCP. Inside the channels an avalanche of secondary electrons is created. These secondary electrons amplify the original signal.*

channels by the electric field between the front and the rear electrode. The secondary electrons repetitively hit the wall and produce an avalanche of secondary electrons. Via a capacitor (1 nF) which is connected parallel to the high voltage supply this avalanche signal is taken (s. Fig. 3.7). Then it is amplified by a fast amplifier (FL8000, GSI). A constant fraction (Constant Fraction Discriminator 473, ORTEC) is used in the leading edge mode to convert the negative signal into a logical TTL-pulse. Additionally, the discriminator is used to reduce noise on the signal. The logical pulses are detected using a counter card (*National Instruments PC-TIO-10*, 32bit counter) in a standard PC. The software *Labview* ^{TM}produced *National Instruments* is used for further processing of the data.

The ion optics system consists of three electrodes which have cylindrical symmetry. They are designed to serve for two purposes. First, ions are accelerated towards the MCP and second, they are designed as an Einzellens to narrow the spatial region from which ions are detected. The three lens electrodes are isolated against each other by ceramic cylinders which also stabilize the mechanical construction. Three individual voltages can be applied to the lens electrodes to image only the region of the atom cloud. Therefore, restgas ions which are the main background in the measurement are only detected from this region. The restgas ions are produced in collisions along the whole ion beam. Without the lens system the restgas ions would be attracted from the whole trap chamber by the electric field of the MCP. The lens system thus narrows this region and reduces the background signal. For a detailed drawing of the lens system see Appendix A.

Unfortunately, during the building process a thin metallic film was deposited on the ceramics. This film electronically connects the electrodes. As a consequence, the voltages of the electrodes cannot be individually set. For

the experiments presented here all electrode voltages are set to -2 kV. The ring electrode is set to +10 kV. It is used to push the ions towards the MCP and to homogenize the electric field which accelerates the ions.
The MCP can be combined with the recombination or the ionization detector inside the TSR. Coincidences between ionization of the atom cloud and electron capture by the ion beam or ionization of the beam can be investigated. The recombination/ionization signal is used for a time-of-flight measurement of the ionized cesium atoms. These experiments will be described in detail in chapter 4.

3.1.1 Calibration of the Time-of-flight of the Cesium Ions

The calibration of the time-of-flight for cesium ions is important for the determination of the charge states produced in the collision processes. Since the flight time depends on the charge the different cesium ions can be distinguished if the flight time for one of the cesium ions, e.g. singly-charged Cs^{1+} is known.

The calibration of the flight time is based on photoionization of the cesium atoms. The setup for the time-of-flight measurement of the Cs^{1+} is illustrated in figure 3.3. We use a pulsed Nd:YAG-laser at a wavelength of 532 nm which is

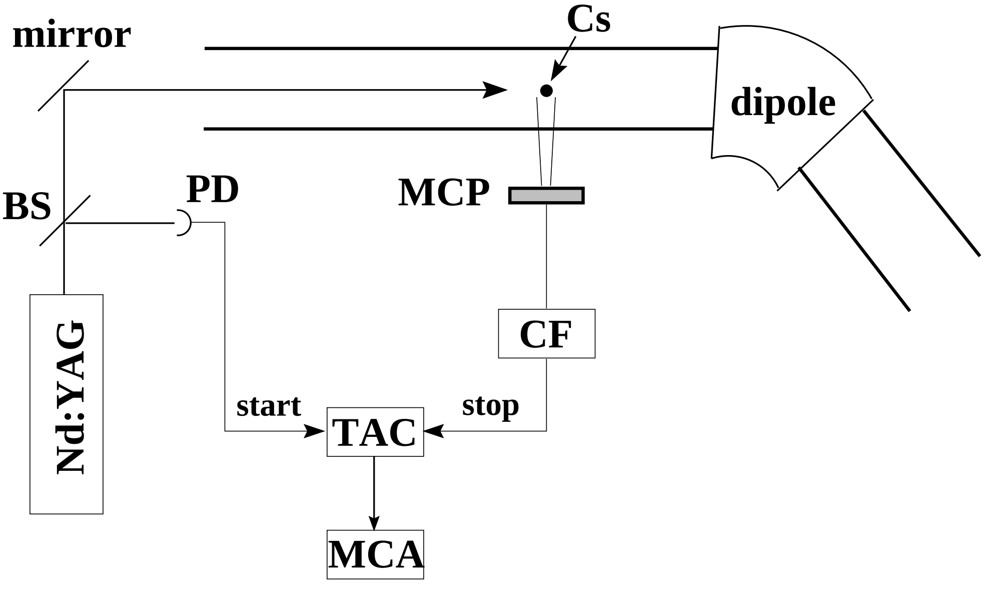

Figure 3.3: *Schematic drawing of the setup for the time-of-flight calibration (bs: beam splitter, PD: photo diode).*

focused to the position of the atom cloud by a telescope using two lenses with focal lengths of f_1=75 mm and f_2= 175mm at a distance of d = 225 mm. The distance between the laser and the atom cloud is $\approx$ 15.5 m. At the position of the cloud the laser beam is focused to a diameter of $\approx$ 1 mm. The length of the laser pulse is 7 ns and the repetition rate is 50 Hz with an energy of $\approx$ 5 mJ/pulse. In order to photoionize the cesium the cloud is moved into the focussed laser beam. The photoionization of the cesium is a two-photon process for the ionization of the 6s electron. The binding energy of the 6s electron is 3.9 eV. The pulsed laser ionizes the trapped cesium atoms and the flight time of the cesium ions is measured by a TAC. The start trigger for the measurement is given by the laser pulse which is registered by a photodiode. The stop pulse is generated by the signal of the MCP. The measured amplitude of the TAC is then given into a MCA. The resulting spectrum is shown in figure 3.4. This spectrum has to be calibrated since

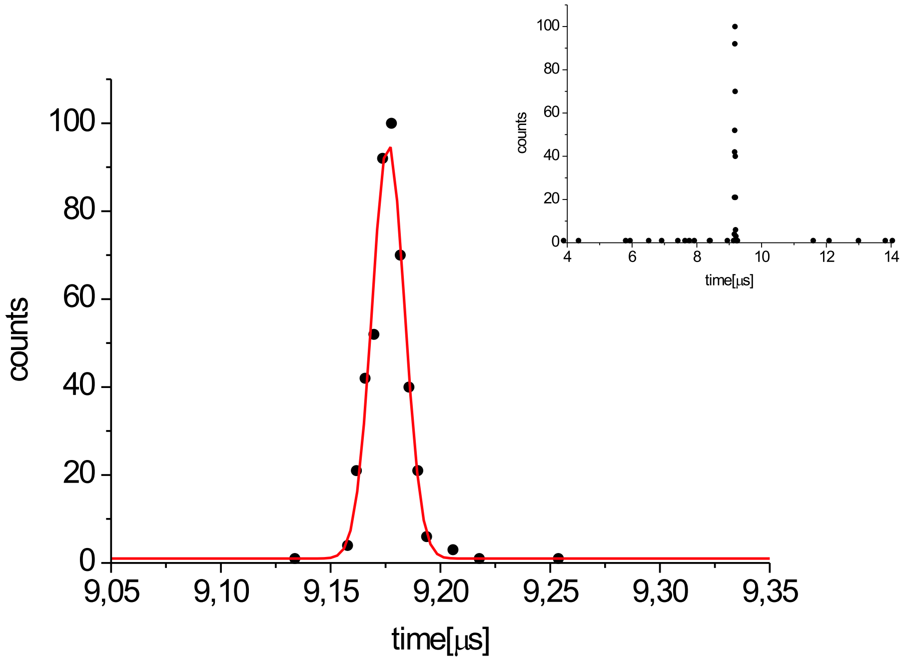

Figure 3.4: *MCA spectrum for the Cs^{1+} ion. The inset shows the total spectrum. The width of the peak corresponds to σ_t = 8 ns. The flight time t_0 has to be shifted according to several time delays in the measurement (s. App. C).*

delays in the coincidence caused by e.g. the electronics and the cables have to be considered. Finally, using this method we measured a time-of-flight for Cs^{1+} of 9.27 μs $\pm$ 0.04 μs. The width σ_t = 8 ns of the peak corresponds to a calculated difference in the length of the flight path of $\approx$ 400 mum. This is a clear indication that the width σ_{t} is mainly given by the size of the atom cloud since the laser beam is much broader than the cloud.

The calibration of the MCA is summarized in Appendix C.

Comparison of the TOF Measurement to a Simulation Using SIMION$^{\mathrm{TM}}$

The program SIMION$^{\mathrm{TM}}$ has already been used by J. Kleinert to simulate different ion detection schemes for the actual experiment [Kleinert, 2002]. The program calculates numerically the Laplace equation for a given geometry. For a more detailed description of the simulation of our setup see [Kleinert, 2002].

The ability of SIMION$^{\mathrm{TM}}$ to simulate trajectories of ions including the field configurations was applied to study the time-of-flight of the produced Cs^{1+} ions. An example of the simulation is shown in figure 3.5. The cesium ions start from realistic points (the accessible region of the cloud) inside the chamber. The initial momentum of the produced cesium ions has been neglected in this simulation. The TOF which is extracted from the simulation varies between 9.21 μs and

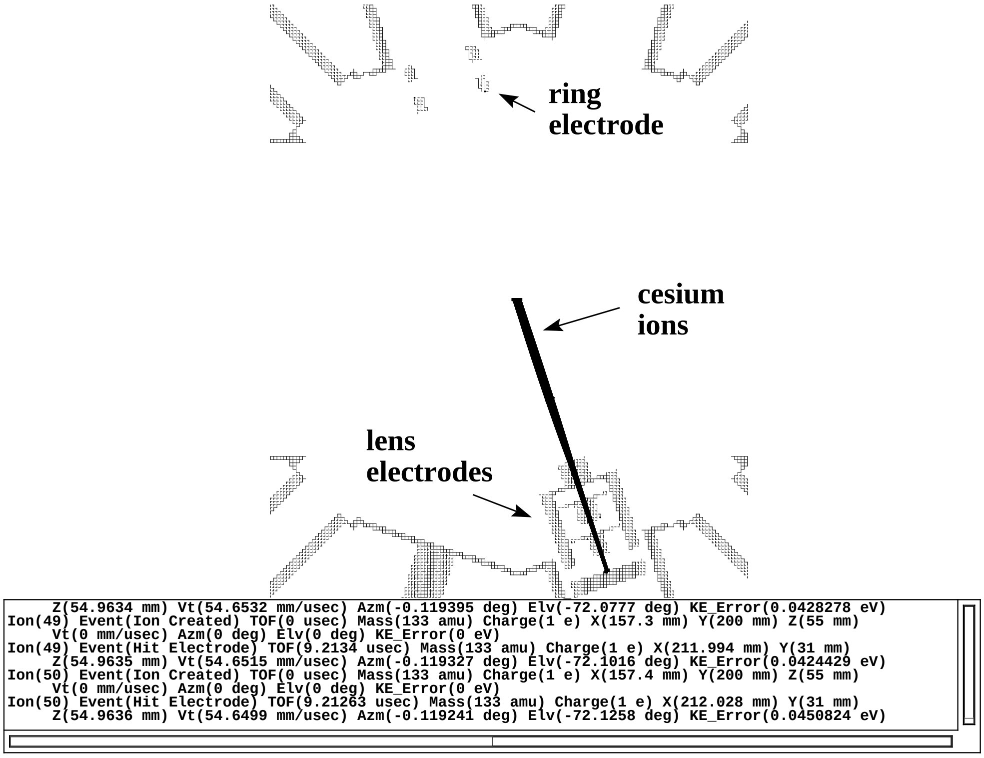

```
     Z(54.9634 mm) Vt(54.6532 mm/usec) Azm(-0.119395 deg) Elv(-72.0777 deg) KE_Error(0.0428278 eV)
Ion(49) Event(Ion Created) TOF(0 usec) Mass(133 amu) Charge(1 e) X(157.3 mm) Y(200 mm) Z(55 mm)
     Vt(0 mm/usec) Azm(0 deg) Elv(0 deg) KE_Error(0 eV)
Ion(49) Event(Hit Electrode) TOF(9.2134 usec) Mass(133 amu) Charge(1 e) X(211.994 mm) Y(31 mm)
     Z(54.9635 mm) Vt(54.6515 mm/usec) Azm(-0.119327 deg) Elv(-72.1016 deg) KE_Error(0.0424429 eV)
Ion(50) Event(Ion Created) TOF(0 usec) Mass(133 amu) Charge(1 e) X(157.4 mm) Y(200 mm) Z(55 mm)
     Vt(0 mm/usec) Azm(0 deg) Elv(0 deg) KE_Error(0 eV)
Ion(50) Event(Hit Electrode) TOF(9.21263 usec) Mass(133 amu) Charge(1 e) X(212.028 mm) Y(31 mm)
     Z(54.9636 mm) Vt(54.6499 mm/usec) Azm(-0.119241 deg) Elv(-72.1258 deg) KE_Error(0.0450824 eV)
```

Figure 3.5: *Simulation of the ion trajectories. The flight time is indicated in the lower box.*

9.28 μs depending on the starting position. Since the electric field is almost constant at the varying start positions of the cesium ions, the time-of-flight does not change very much. In the lower box of Fig. 3.5 the different flight times ('TOF') are shown for the last ion trajectories calculated in the simulation. The values agree very well with the measured time-of-flight. Figure 3.6 shows the electric field between the starting position of the cesium ions and the MCP according to the simulation.

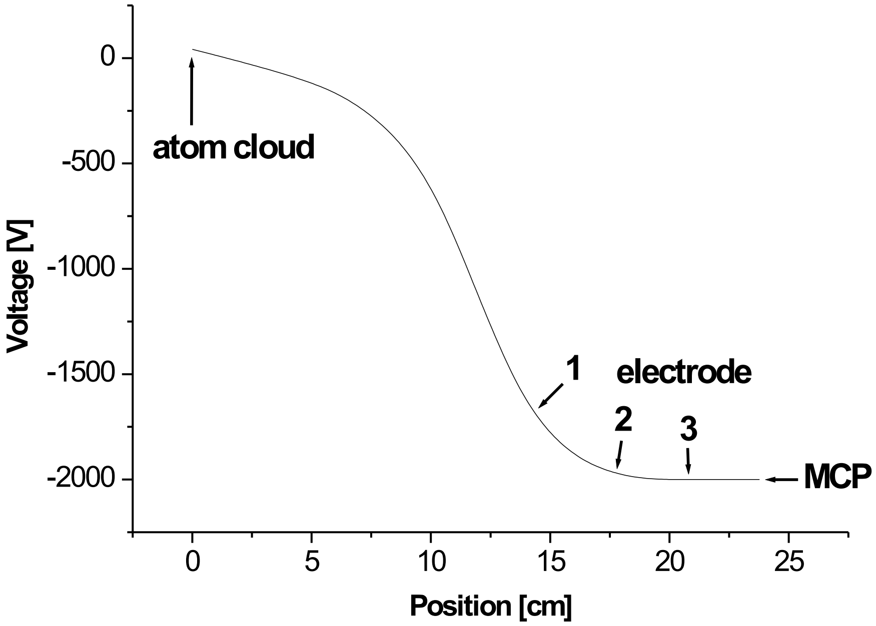

Figure 3.6: *Electric field between the start position of the cesium ions and the MCP according to the simulation.*

3.2 Fluorescence Detection

The fluorescence of the trapped atoms is measured with two CCD-cameras. The camera signals are fed into a tv-card (WINTV, *Hauppauge*) and are grabbed using a frame grabber which is embedded into *Labview* ^{TM}. A relais is used to switch between the two cameras. The stereoscopic fluorescence detection is used for two purposes. First, the fluorescence is used to depict the number of trapped particles. Since the fluorescence is proportional to the number of trapped atoms the development of the particle number can be imaged and especially losses from the trap can be watched. Second, the actual position of the atom cloud is determined by the two CCD-cameras. The position of the trapped atoms differs slightly from the position of the magnetic zero. The mean deviation is about 100 μm and it is caused by interference patterns in the overlap of the laser beams. In addition, the interferences cause a spatially varying light shift inside the laser field. This leads to varying fluorescence intensity of the atoms. At certain points the fluorescence can even vanish, although the atoms are still trapped. The deviation of the cloud's position and the fluctuations of the fluorescence can be reduced by modulating the retroreflecting mirrors. The relative phase of the laser beams can be scrambled, if mirrors mounted on small pc-speakers are used. So the mean deviation of the cloud's position from the magnetic field zero can be reduced to about 50 μm.

3.3 Beam Profile Measurement

3.3.1 Control of the Experimental Sequence

The control of the experiment is based on the software *Labview* ^{TM} produced by *National Instruments*. All major tasks like position control, ion counting, and fluorescence detection are executed by pc-cards. Each card is represented by a so-called *virtual instruments* and these instruments are addressed and managed by *Labview* ^{TM}. Figure 3.7 shows the principle of the experiment control. The position of the cloud is controlled by an analog output card *PCI-6208V* from *Adlink Technology Inc*. The card includes 8 analog voltage outputs which range from -10 V to +10 V and it provides 4 digital outputs as well as 4 digital inputs. Two of the analog outputs are used to generate a control voltage. This control voltage is splitted by a voltage devider and drives simultaneously the power supplies of the shifting coils and the compensation coils. This ensures that moving the cloud generates no feedback on the closed orbit.

The logic pulses from the MCP are registered using a counter card (s. Sec. 3.1) and are processed by *Labview* ^{TM}. In this way the position dependent number of counts can be displayed directly. The pictures of the cloud are grabbed from the tv-card. They are processed by a frame grabber which is a *virtual instrument* of *Labview* ^{TM}. Further processing of the pictures like cutting or background substraction can be done by *Labview* ^{TM}, too. One of the above mentioned digital-out ports is used to switch between the two CCD-cameras.

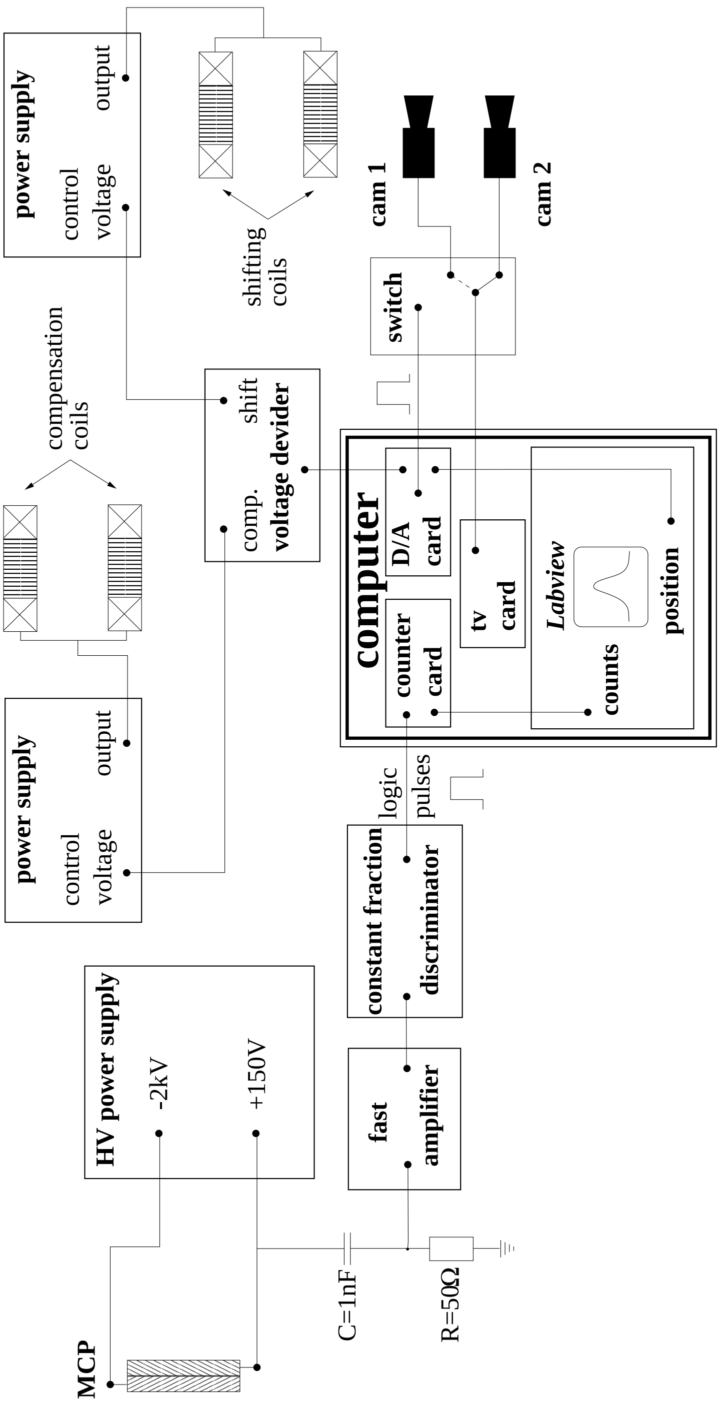

Figure 3.7: *Schematic drawing of the experiment control. The control is based on the software* Labview ™ *produced by* National Instruments.

3.3.2 Overlap Between the Stored Ions and the Target

The atom cloud can be moved within the overlap of the laser beams. Since the beam diameter is about 20 mm, this region is rather limited compared to the beam tube with a diameter of 200 mm. So it is very unlikely that the stored ions can be reached with the cloud without any adjustment of the ion beam.

Since the magnetic zero of the quadrupole trap field is the position of the cloud, the ion beam is adjusted into the magnetic zero. The ion beam's position is adjusted in the following way: Using the shifting coils the magnetic zero is set to the center of the laser overlap. This ensures that the ion beam is placed within the accessible area of the cloud.

The current of the quadrupole coils is now set step by step to 7 A, 8 A and 9 A. For each current the position of the ion beam is determined by the restgas beam profile monitor. The position of the beam will change if it does not cross the magnetic zero of the quadrupole field. The change of the magnetic field due to the current steps causes this displacement (s. Sec. 2.5.1). In order to move the ion beam into the zero the magnets LB11 (slow bumper magnet, horizontal displacement) and the KV12 (vertical correction magnet) are used to adjust a new closed orbit. Then this new orbit is checked again with the method mentioned above. This procedure has to be repeated several times until it converges. In particular since the horizontal and the vertical manipulations of the ion beam are not completely decoupled. Finally, the deviation of the ion beam for all quadrupole coil currents should be smaller then the resolution of the BPM. As a consequence the ion beam passes the quadrupole field very close to its zero.

In addition, the profile of the stored beam has to be checked for each new orbit. Since the adjustment of the position changes the alignment between the ion beam and the electron cooler it might be necessary to readjust the electron cooler, too. Otherwise there won't be proper cooling conditions anymore. After this adjustment the ion beam can be reached by moving the cloud. A systematic check of the area the cloud can access shows an interaction between the ion beam and the atom cloud. The interaction is described in detail in section 3.3.3. Using a two-dimensional scan the exact profile of the beam can be determined. This procedure is described in section 3.3.4.

3.3.3 Interaction Between the Stored Ions and the Trapped Atoms

The ion count rate and the fluorescence intensity offer two complementary methods to measure ion beam induced losses from the trap. This makes quantitative investigations of ion-atom interactions accessible. The interaction is measured in the following way: The trap is loaded outside the ion beam until the atom number reaches a steady state. The loading time is $\approx 30\,\mathrm{s}$. The cloud is then moved to the measuring position by shifting the magnetic zero. The count rate of the MCP and the fluorescence are recorded as a function of time. Figure 3.8 shows the effect of the ion beam on the trapped atoms. At the beginning the fluorescence signal (a) is constant since the trap is in a steady state outside the ion beam. The count rate of 100 Hz of the MCP (b) is only caused by ionized restgas. Although the lens system (s. Fig. 3.1) cannot be used as an Einzellens the background is suppressed efficiently (s. Fig. 3.8). Then the cloud is moved into the beam.

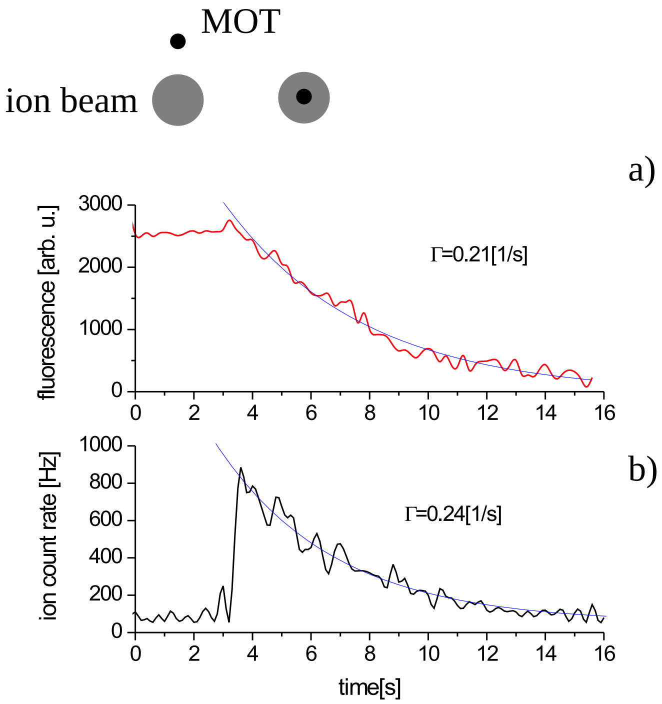

Figure 3.8: *The trap is loaded outside the ion beam. At t=3 s the cloud is moved to the measuring position. a) Outside the beam the fluorescence signal is constant. After the move the number of atoms in the cloud decreases imaged by the fluorescence light. b) Before the jump only restgas ions are detected. Then the rate increases due to the interaction with the ion beam and the count rate shows the decay of the atom cloud. Finally, an equilibrium between loss rate and loading rate is reached.*

The interaction with the ion beam reduces the number of trapped atoms. The losses are monitored by the fluorescence signal. These losses can be described as

$$\frac{d}{dt}n_{\mathrm{Cs}}(\vec{\mathrm{r}},\mathrm{t}) = \frac{L}{V} - \alpha n_{\mathrm{Cs}}(\vec{\mathrm{r}},\mathrm{t}) - \sigma \cdot v \cdot n_{\mathrm{Ion}}(\vec{\mathrm{r}} - \vec{\mathrm{r}_0}) \cdot n_{\mathrm{Cs}}(\vec{\mathrm{r}},\mathrm{t}), \tag{3.1}$$

where $n_{\mathrm{Cs}}(\vec{\mathrm{r}},\mathrm{t})$ is the density distribution of the trapped cesium atoms, L the loading rate of the cesium, V the volume of the cloud, α the rate coefficient for losses caused by collisions with the restgas, σ the cross section for collisions between ions and trapped atoms, v the velocity of the ion beam and $n_{\mathrm{Ion}}(\vec{\mathrm{r}}-\vec{\mathrm{r}_0})$ is the density of the ion beam at the position of the atom cloud and $n_{\mathrm{Cs}}(\vec{\mathrm{r}},\mathrm{t})$ is the density distribution of the trapped atoms. Quadratic losses inside the cloud (s. Sec. 2.3.2, Eq. (2.13)) are neglected. If equation (3.1) is written for the number of trapped particles N_{Cs}, this leads to an overlap integral for the beam density and the trap density.

$$\begin{aligned}\frac{d}{dt}\int_{\mathrm{V}} n_{\mathrm{Cs}}(\vec{\mathrm{r}},\mathrm{t})\,d^3r &= \int_{\mathrm{V}}\frac{L}{V}\,d^3r-\alpha\int_{\mathrm{V}} n_{\mathrm{Cs}}(\vec{\mathrm{r}},\mathrm{t})\,d^3r\\ &\quad -\sigma\cdot v\cdot\int_{\mathrm{V}} n_{\mathrm{Ion}}(\vec{\mathrm{r}}-\vec{\mathrm{r}_0})\cdot n_{\mathrm{Cs}}(\vec{\mathrm{r}},\mathrm{t})\,d^3r. \qquad (3.2)\end{aligned}$$

The integration leads to an expression for the particle number $N_{\mathrm{Cs}}(t)$

$$\begin{aligned}\frac{d}{dt}N_{\mathrm{Cs}}(t) &= L-\alpha\cdot N_{\mathrm{Cs}}(t)-\sigma\cdot v\cdot n_{\mathrm{Ion}}(\vec{\mathrm{r}_0})\cdot N_{\mathrm{Cs}}(t)\\ &= L-\alpha\cdot N_{\mathrm{Cs}}(t)-\Gamma_{\mathrm{Ion}}(\vec{\mathrm{r}_0})\cdot N_{\mathrm{Cs}}(t), \qquad (3.3)\end{aligned}$$

where $n_{\mathrm{Ion}}(\vec{\mathrm{r}_0})$ is the ion beam density of the beam at the position $\vec{\mathrm{r}_0}$ of the atom cloud. The introduced $\Gamma\mathrm{Ion}(\vec{\mathrm{r}_0})$ describes the decay of the atom cloud induced by the ion beam density at the position of the cloud. The density distributions are assumed to be gaussian shaped with the widths $\sigma_{\mathrm{i,Cs}}$ and $\sigma_{\mathrm{i,Ion}}$. Furthermore it is assumed that the ion beam density distribution $n_{\mathrm{Ion}}(\vec{\mathrm{r}_0})$ does not depend on the time t, i.e. the ion beam does not decay. The evaluation of the integral is shown in detail in appendix D. For small particle numbers the widths $\sigma_{\mathrm{i,Cs}}$ of the trap depend only on the temperature T (s. Eq. (2.11)) and therefore the volume V is constant. Equation (3.3) can now be solved. The solution of the differential equation is

$$N_{\mathrm{Cs}}(t) = \left(N_{0,\mathrm{Cs}}-\frac{L}{\alpha+\Gamma_{\mathrm{Ion}}(\vec{\mathrm{r}_0})}\right)\cdot e^{-\alpha\cdot t-\Gamma_{\mathrm{Ion}}(\vec{\mathrm{r}_0})\cdot t}+\frac{L}{\alpha+\Gamma_{\mathrm{Ion}}(\vec{\mathrm{r}_0})}, \qquad (3.4)$$

where $N_{0,\mathrm{Cs}}$ is the number of trapped particles before the atoms are moved into the ion beam.

After moving the cloud into the ion beam the ion count rate increases because the target starts interacting with the ion beam. Then the rate decreases similar to the fluorescence signal since the ionization rate R_{Ion} of trapped atoms is described by $R_{\mathrm{Ion}} = \sigma\cdot v\cdot n_{\mathrm{Ion}}(\vec{\mathrm{r}_0})\cdot N_{\mathrm{Cs}}(t) = \Gamma_{\mathrm{Ion}}(\vec{\mathrm{r}_0})\cdot N_{\mathrm{Cs}}(t)$ in equation (3.3). $\Gamma_{\mathrm{Ion}}(\vec{\mathrm{r}_0})$ can be assumed to be constant for the actual measurement (the ion beam does not decay) the MCP count rate depends on the number of trapped atoms. Consequently, the decay rate extracted from both signals is almost the same. From the example in figure 3.8 the fluorescence signal gives a decay rate of $\Gamma_{\text{fluo}} = 0.21\,s^{-1}$ and the ion count rate yields $\Gamma_{\text{Ion}} = 0.24\,s^{-1}$ at an ion beam density of $n_{\text{Ion}}(\vec{r_0}) = 2 \times 10^6/\text{cm}^3$. Moreover, the cross section σ for the ionization of trapped atoms can be determined because $\Gamma_{\text{Ion}}(\vec{r_0})$, v, and $n_{\text{Ion}}(\vec{r_0})$ are known or can be measured. In this measurement the cross section σ is determined to $\sigma = 2.6 \times 10^{-15}\,\text{cm}^2$. The measurement of different cross sections will be described in detail in chapter 4. Finally, the signals reach an equilibrium because the trap is loaded during the whole measurement. For long times t the first part of equation (3.4) including the exponential decay converges to zero:

$$\begin{aligned}\lim_{t\to\infty} N_{\text{Cs}}(t) &= \frac{L}{\alpha + \sigma \cdot v \cdot n_{\text{Ion}}(\vec{r_0})} \\ &= \frac{L}{\alpha + \Gamma_{\text{Ion}}(\vec{r_0})}. \end{aligned} \tag{3.5}$$

So the equilibrium density in the trap is determined by the density $n_{0,\text{Ion}}(\vec{r_0})$ at the position of the cloud since L, V and α remain constant. In addition, the time which is needed to reach the equilibrium is defined by the exponential part of equation (3.4) and thus again by the density $n_{\text{Ion}}(\vec{r_0})$. On the one hand a large $\Gamma_{\text{Ion}}(\vec{r_0})$ causes a fast convergence but on the other hand it leads to a rather small equilibrium particle number $\bar{N}_{\text{Cs}}$ and with it to a small count rate which cannot be distinguished from the restgas ionization anymore. Therefore, in figure 3.8 the equilibrium cannot be clearly identified against the restgas signal. Nevertheless, the procedure described above can be used to determine step by step the decay rate Γ_{Ion} of the cloud at every position inside the ion beam and thus the density distribution of the beam is imaged.

3.3.4 Measuring the Ion Beam Profile

The atom cloud is used as a probe to measure the density distribution of the stored ion beam. Moving the trapped atoms through the beam a two-dimensional scan of the stored ions is performed. The count rate of the MCP is monitored as a function of the position of the atom cloud. Figure 3.9 shows the measured count rates as a function of the cloud's position. As mentioned above the measured count rate is given by $R_{\text{Ion}} = \Gamma_{\text{Ion}}(\vec{r_0}) \cdot N_{\text{Cs}}(t)$ (s. Eq. (3.3)). Since the measurement is done for only 0.2 s, the equilibrium between losses and loading is disturbed only slightly. The number of trapped atoms $N_{\text{Cs}}(t)$ can be kept almost constant during the measurement. Therefore, the count rate is determined by $\Gamma_{\text{Ion}}(\vec{r_0})$. Since $\Gamma_{\text{Ion}}(\vec{r_0}) \propto n_{\text{Ion}}(\vec{r_0})$ the rate of produced cesium ions depends on the local density of the ion beam at the position of the cloud $\vec{r_0}$. As a result, the measured count

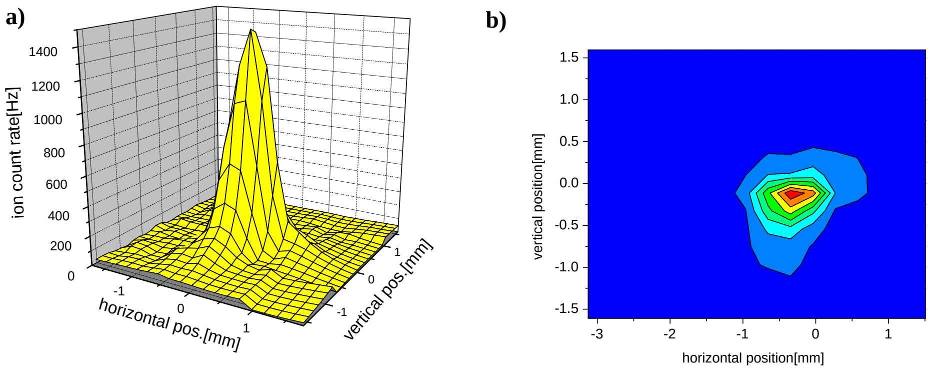

Figure 3.9: *Count rate of the MCP depending on the atom cloud's position inside the stored ion beam shown as a three-dimensional plot a) and as a density plot b).*

rates are a direct image of the density distribution of the beam. The position of the atom cloud is determined by the two CCD-cameras.

The scanning procedure is done as follows: The trap is loaded outside the ion beam until the steady state is reached. Then, the cloud is moved near the ion beam and the scan is performed with a mesh of e.g. 15 × 15 measuring positions. During the scan the trap is loaded continuously. As long as the cloud is outside the ion beam only restgas ions are detected. In figure 3.9 the outer regions with a count rate of ≈50 Hz correspond to this situation. The count rate increases significantly if the cloud interacts with the ion beam. At each point the counts of the MCP are recorded for 0.2 s.

During the scan several conditions have to be taken into account. The position of the atom cloud is determined by the fluorescence. During the measurement it becomes difficult to determine the cloud's position using the CCD-cameras. The repetition rate of the program taking the fluorescence images is very small. Therefore, it is not possible to measure fast enough (i.e. fast compared to the decay of the atom cloud) the counts of the MCP and the position of the cloud. The cloud would stay too long at a certain position which reduces the number of trapped atoms. To avoid this problem a calibration measurement is done without stored ions. The position of the cloud is imaged as a function of the current of the shifting coils (or the magnetic zero, respectively). The positions are scanned very fine, i.e. the distance between two positions is small in order to get a high spatial resolution. Figure 3.10 shows two examples of the position calibration. It is possible to extrapolate the positions where the cloud's fluorescence vanishes and the deviation from the magnetic zero can be determined. During the profile measurement the count rate is recorded as a function of the current of the shifting

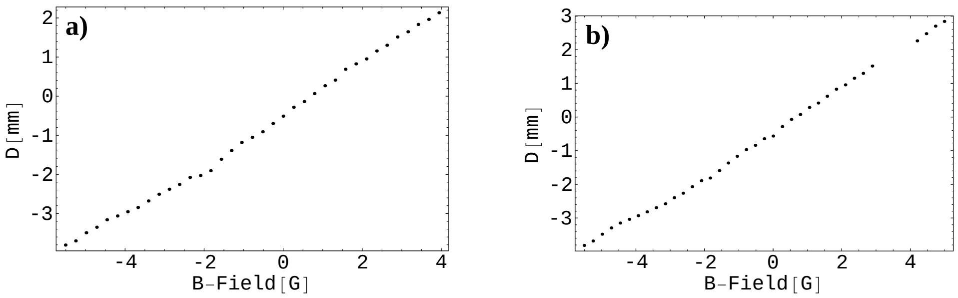

Figure 3.10: *Calibration measurement of the cloud's position. a) The deviation from the straight line can be extrapolated due to the fine mesh. b) Example of a position where the fluorescence vanishes. Since the measuring positions are very close the missing positions can be extrapolated by a straight line, too.*

coils. Afterwards the data sets of the calibration and the profile measurement are composited to the count rate depending on the cloud's position.

Concerning the ionization signal one has to take care of two main uncertainties of the measurement. According to equation (3.3) the number of produced cesium ions depends on $\Gamma_{\mathrm{Ion}}(\vec{r_0}) \cdot N_{\mathrm{Cs}}(t)$. This means that the density distribution of the ion beam must not change during the the two-dimensional scan and the density of the trapped atoms has to be constant, too. In fact, the stored ion beam decays by collisions with restgas according to

$$N_{\mathrm{Ion}}(t) = N_{0,\mathrm{Ion}} \cdot \exp(-t/\tau), \tag{3.6}$$

where $\mathrm{N}_{0,\mathrm{Ion}}$ is is the number of ions at the beginning and τ is the lifetime of the stored ions. Since the lifetime for each beam and the elapsed measuring time are known, this time dependence is corrected to a non-decaying ion beam.

In addition, the number of trapped atoms is reduced by the interaction with the ion beam (s. Sec. 3.3.3). As a consequence, the count rate decreases, too. In order to suppress this effect the two-dimensional scan has to be done fast compared to the reduction of the number of trapped atoms. Figure 3.11 shows a calculation of the development of the number of trapped atoms and the produced cesium ions if the cloud is moved once through the center of the stored ion beam. The number of ions is scaled by a factor of 5. The calculated beam is assumed to be a gaussian with a width of $\sigma_{\mathrm{x,y}} = 0.3\,\mathrm{mm}$. The values of the fluorescence and of the ionized cesium atoms are in this example calculated at 25 positions and correspond to one line of a two-dimensional scan with 25×25 points. At each point the cloud remains for 0.2 s (a) and 1.0 s (b). It becomes clear that in case b) the number of trapped particles is reduced rather strong and, therefore, the maximum of the ionized cesium atoms is shifted to the left (the scan starts from the left). So the ion beam is not imaged correctly. Case a) shows a correct image of the ion beam.

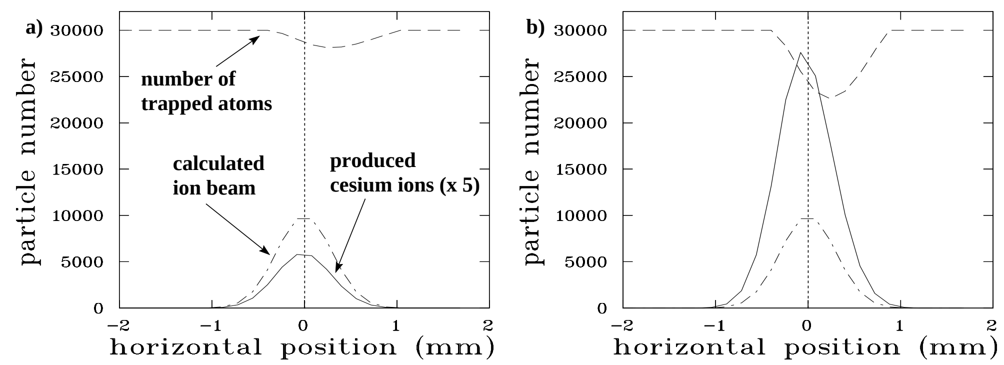

Figure 3.11: *A calculated ion beam profile is scanned with the atom cloud. The development of the number of trapped atoms and the number of the ionized cesium (× 5) is calculated for a measuring time of 0.2 s (a) and of 1.0 s (b) at each position.*

Experimentally, we found that during the two-dimensional scan a number of 30 - 300 cesium ions are produced per step. This corresponds to a rate of 150 Hz - 1.5 kHz (s. Fig. 3.9). The estimation of the loading rate $L \approx 500$ atoms·s^{-1} (s. Eq. 2.18) shows that the loss can be compensated for lower ionization rates (outer regions of the ion beam) and leads to a reduction of trapped atoms for higher rates (center of the ion beam). This situation is displayed in figure 3.11 a). If the reduction is small compared to the total number of trapped atoms the scan still yields the correct beam profile. If the number of produced ions in a complete two-dimensional scan is compared to the number of ions produced in a measurement of the decay rate (s. Fig. 3.8) we find that in the latter case the number of ions produced per step is about a factor of 6 - 8 higher. There the number of trapped particles is reduced strongly which is indicated by the fluorescence signal (s. Fig. 3.8). This shows that the total number of trapped atoms changes only slightly during the scan which is in very good agreement with the simulation.

The problem becomes even clearer if the complete two-dimensional scan is calculated. In this case a reduction of the number of trapped particles propagates through the whole scan. Figure 3.12 shows the above mentioned calculated ion beam in a density plot. The result for the two-dimensional scan with 1 s of measuring time is shown in figure 3.13. In figure 3.13 a) the scan is done in the horizontal direction and after each line the cloud is moved vertically. In figure 3.13 b) it is done vice versa. It becomes clear that the measured profile is shifted. The high ion beam current reduces the number of trapped atoms too strong and the distribution of the ionization rate R_{Ion} is shifted. Therefore, the results differ depending on the scanning procedure. We observe the same behaviour if the density of the stored ions is too high. Again, the number of trapped atoms is reduced too strong and,

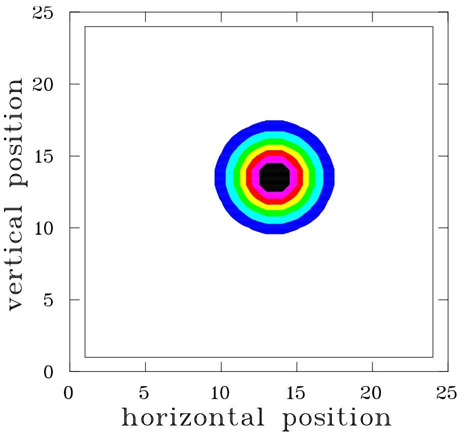

Figure 3.12: *The calculated ion beam with a width of* $\sigma_{\mathrm{x,y}} = 0.3$ *mm.*

therefore, the measured profile is shifted. It is necessary to adjust the measuring parameters very carefully. Only if the boundary conditions are taken into account the measured profile will be an image of the real distribution: The ion current has to be low, i.e. the decay time of the atom cloud is large compared to the measuring time. This can be assisted by choosing a measuring time as short as possible. In figure 3.14 a calculation using the correct conditions is compared with a two-dimensional scan of a C^{6+} ion beam [1]. The calculation and the measured profile are in good agreement. Now the ion beam current in the calculation is increased by a factor of ten. Figure 3.15 a) shows the results for the calculation and b) for a C^{6+} profile we measured. The measuring time is again 0.2 s. Figure 3.15 shows a vertical scan with horizontal steps. The center of the measured distribution is shifted compared to figure 3.14. In addition the shape of the calculation and the measurement agree and the shown effects are comparable. If the ion beam current is again increased no profile can be recognized anymore. Figure 3.16 a) shows a calculation where the ion beam current again is increased by a factor of ten. The measurement for C^{6+} is shown in b). At this far too high current the profile is distorted and no density distribution can be determined anymore. The calculation and the observed effects are comparable. The number of trapped particles is already reduced very strongly in the outer regions of the ion beam. Therefore, the rate R_{Ion} is rather high but in the center of the beam there are only few trapped atoms left. So the ionized cesium cannot be distinguished from the restgas signal anymore.

The considerations done here show that this method is limited at ion beam

---

[1] The measured profile shown here is not an ideal one. But in the series of measurements done with this ion beam the effects described later on occurred. In this way the effect of the reduction of the ion beam current is presented in a consistent way.

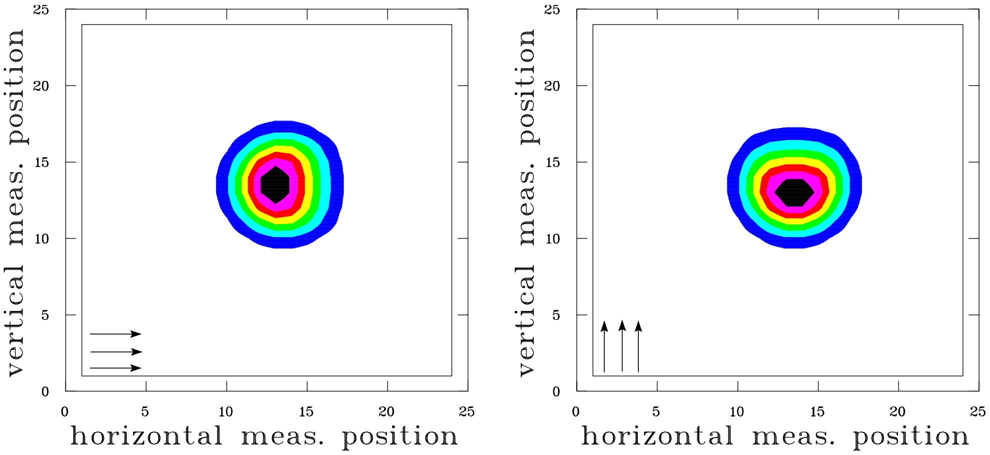

Figure 3.13: *Calculated beam profile with a measuring time of 1.0 s. a) shows the result for the horizontal scan and vertical steps. b) shows a vertical scan with horizontal steps.*

currents higher than $\approx 1\,\mu$A. In addition, the measuring time has to be short compared to the decay constant $\Gamma_{\mathrm{Ion}}(\vec{r_0})$ in the exponential part of equation (3.4). Nevertheless, this method can provide beam profiles down to currents of some nA which cannot be reached using the restgas beam profile monitor. Besides, the restgas BPM has to integrate in the order of minutes at its limit in order to provide projections of the horizontal and the vertical profile whereas our scan takes about one minute and offers a complete two-dimensional picture of the density distribution of the ion beam. A one-dimensional scan takes just a few seconds for each direction.

3.3.5 Comparison to Restgas Beam Profile Monitor

The measured profiles using the trapped atoms cannot be compared directly with the profiles of the restgas BPM. One has to consider that the profile of the restgas BPM is a projection of the density distribution onto the horizontal and the vertical plane, respectively. The MOT measures directly the two-dimensional density distribution of the ion beam. Furthermore, the width of the ion beam changes depending on the position inside the TSR. In order to compare the two positions the beam width measured with the atom cloud has to be transformed to the position of the restgas BPM. The transformation is given by the change of the betatron function [Wille, 1996] which is simulated on the lattice of the TSR. For the comparison the two-dimensional profile has to be projected on the appropriate plane and the widths have to be transformed. Figure 3.17 shows the projected and trans-

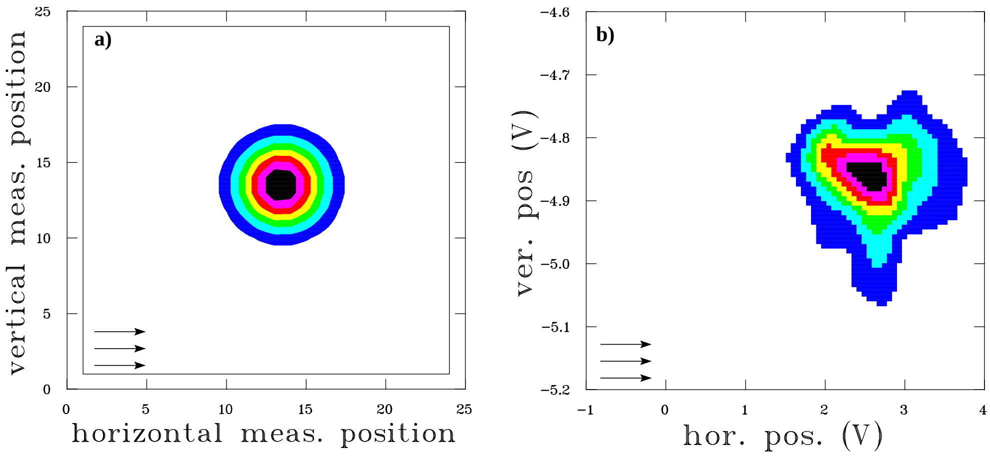

Figure 3.14: *Comparison of a) the calculated profile with b) the measured* C^{6+} *profile.*

formed results for the horizontal a) and the vertical b) profile measurement. The histogram shows the profile of the BPM and the points correspond to the measurement with the MOT. The results of both methods agree very well. Concerning the MOT the measured beam width is slightly smaller. Since the measured width σ_{meas} is a convolution of the real width σ_{real} and the resolution width σ_{res} one can deconvolute the profiles of the restgas BPM and the MOT in order to be able to compare the results. Since the resolution widths are known the real width σ_{real} can be calculated according to

$$\sigma_{\text{meas}} = \left(\sigma_{\text{real}}^2 + \sigma_{\text{res}}^2\right)^{\frac{1}{2}}, \tag{3.7}$$

which leads to

$$\sigma_{\text{real}} = \left(\sigma_{\text{meas}}^2 - \sigma_{\text{res}}^2\right)^{\frac{1}{2}}. \tag{3.8}$$

For the deconvolution a gaussian distribution is assumed. The resolution of the restgas BPM is known from [Beutelspacher, 2000]. The resolution of the profile measurement using the atom cloud is limited by the size of the cloud. The width of the atom cloud is determined by a CCD-camera with calibrated imaging properties. These widths have to be transformed to the position of the BPM. The results are summarized in table 3.1. The deconvolution yields a real horizontal width of ≈ 130 μm. This is consistent with independent measurements performed by [Lange, 2002]. For the vertical width the two measurements cannot be compared because the vertical BPM reached already its resolution limit. Since the deconvolution yields at least for the horizontal measurement the same widths this is a clear indication that the resolution of the measurement using the atom cloud is better than the resolution of the restgas BPM.

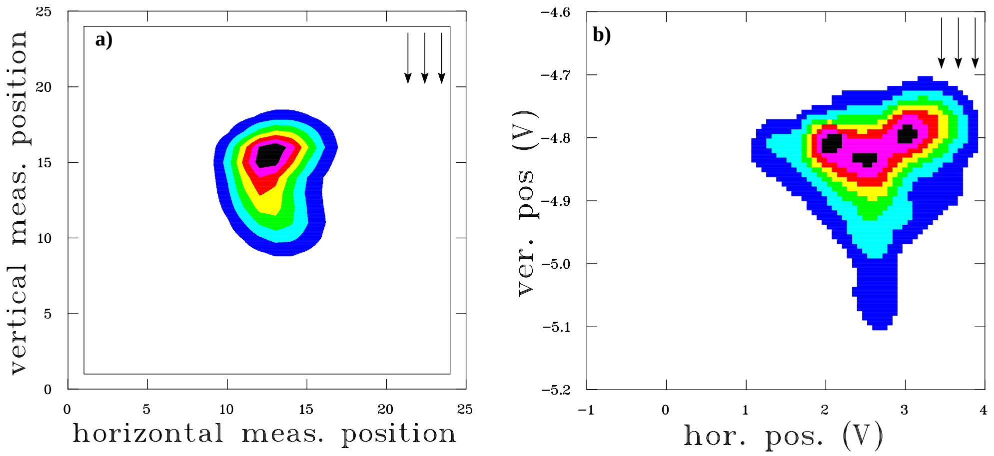

Figure 3.15: *a) Calculated beam profile with much higher ion beam density. b) Measured profile with too high ion current.*

	$\sigma_{\rm MOT}$ [μm]	$\sigma_{\rm MOT,dec}$ [μm]	$\sigma_{\rm BPM}$ [μm]	$\sigma_{\rm BPM,dec}$ [μm]
x	290	125	280	137
y	230	100	200	-

Table 3.1: *Summary of the measured and calculated widths. $\sigma_{\rm MOT}$ denotes the beam width measured with the atom cloud at the position of the trap and $\sigma_{\rm MOT,dec}$ the deconvoluted width at the position of the BPM. The widths are defined analogue for the BPM measurement.*

The simulation which has to be used to obtain the transformation factors for the betatron oscillation includes rather large errors. The bending and focussing fields of the magnets are not exactly known and, therefore, an error of $\approx 20\%$ is assumed for the transformation. Since our measurement of the ion beam's profile includes the widths of the beam we can directly compare the results of our measurement with the simulation of the TSR lattice. In particular this measurement is important for the determination of the total cross sections (s. Chap. 4.2) because the major error is the contribution of the transformed widths. In the previous measurements the width of the ion beam was very close to the resolution of the restgas BPM or already at its limit (s. Tab. 3.1). Therefore, the comparison between the widths of the trap position and of the BPM position are not very reliable, yet. During the next beam time this ratio between the widths will be investigated in detail with a broader ion beam.

To stress the power of this method using the atom cloud the ion beam and the electron cooler were misaligned intentionally. This procedure broadens the stored ion beam since the cooling conditions become worse. Figure 3.18 shows the re-

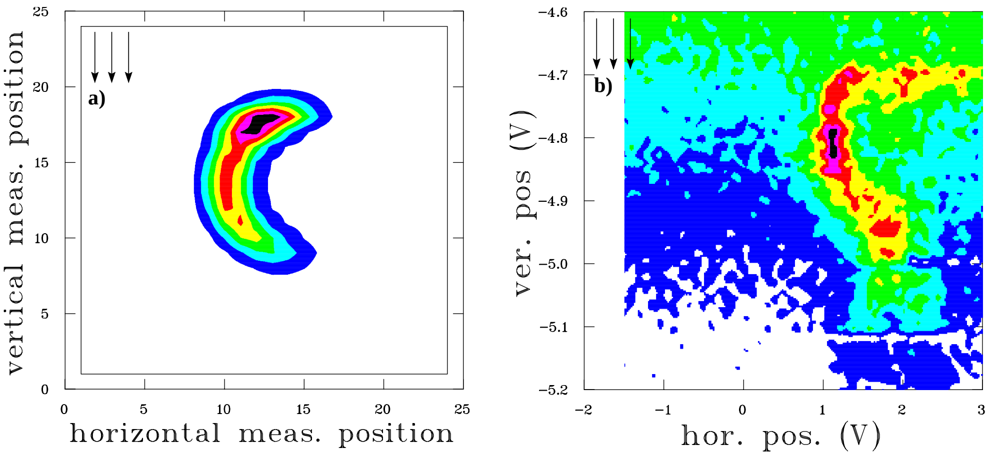

Figure 3.16: *a) Calculated beam profile with far too high ion beam current. b) Measurement of a comparable profile.*

sults of the restgas BPM and the two-dimensional scan. The two-dimensional scan of the ion beam uncovers that the beam has a two-peak structure which is not resolved by the restgas BPM. It is necessary to increase the misalignment until it can be resolved by the restgas BPM, too. This is shown in figure 3.19. The distance between the two peaks grows caused by the stronger misalignment. This measurement is a strong indication that the new method is much more sensitive to imperfections in the ion beam and thus the resolution is higher compared to the restgas BPM.

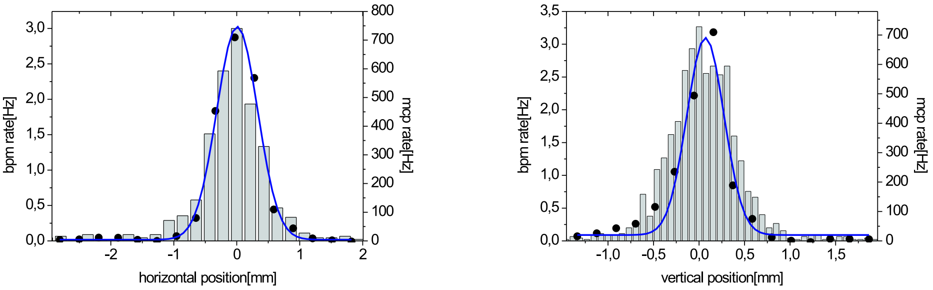

Figure 3.17: *The results of the two independent methods are compared. The horizontal profile a) and the vertical profile b) show very good agreement between the BPM (solid line) and the atom cloud (dashed line).*

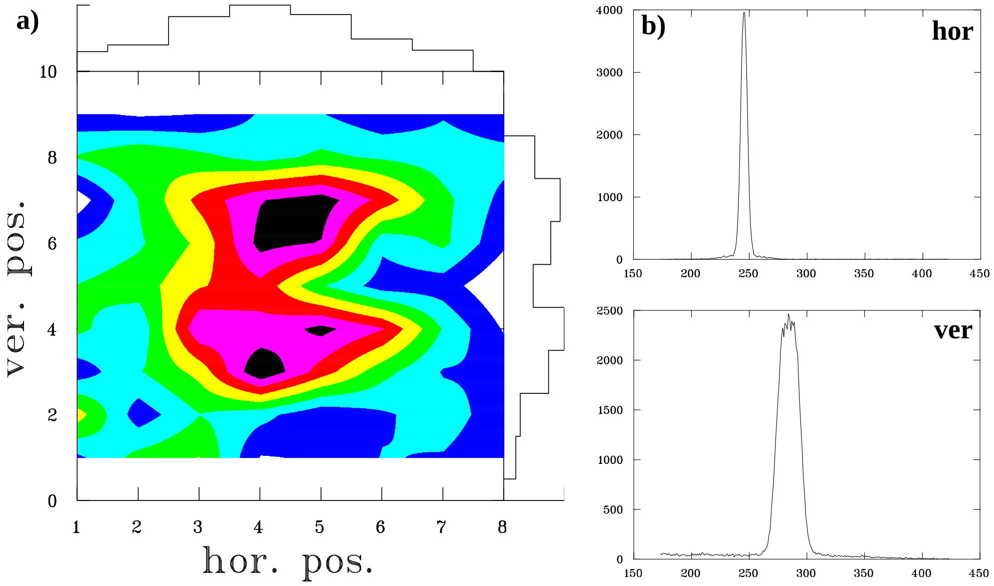

Figure 3.18: *a) Two-dimensional scan of the ion beam after the misalignment of the electron cooler. b) Corresponding profiles of the restgas BPM.*

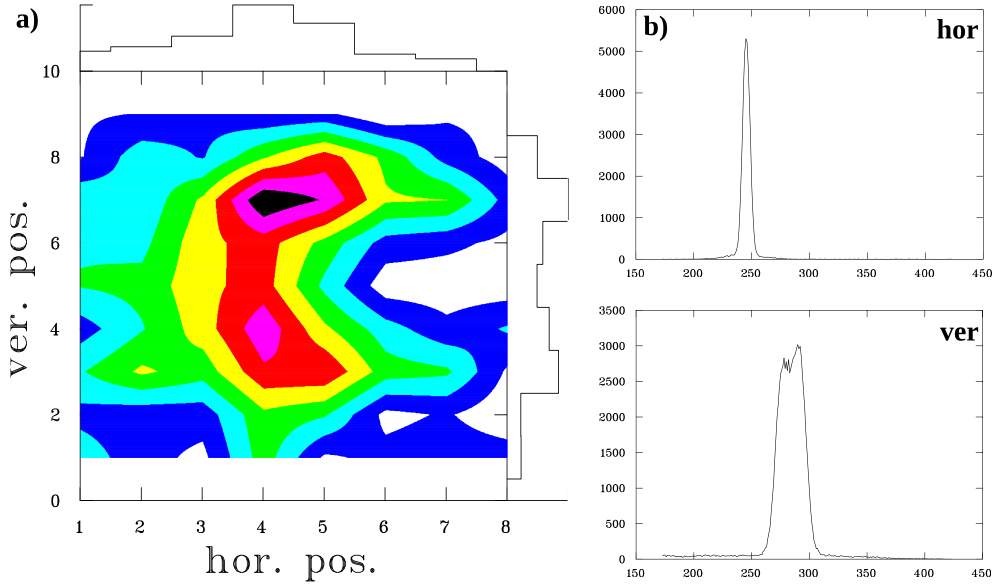

Figure 3.19: *a) The misalignment is increased, the distance between the peaks grows. b) The restgas BPM resolves a double peak structure in the vertical direction.*

Chapter 4

Laser-trapped Atoms as a Target for Collision Experiments

4.1 Measurement of the Ionization Cross Section

The ionization of cesium atoms depends on the number of the trapped cesium atoms $N_{\mathrm{Cs}}(t)$ and on the local density $n_{0,\mathrm{Ion}}$ of the stored ion beam (s. Sec. 3.3.3). This dependence is used to determine the cross section σ for the ionization of the trapped cesium atoms induced by the ion beam:

$$\mathrm{C}^{\mathrm{q}+} + \mathrm{Cs} \rightarrow \mathrm{C}^{\mathrm{q}+} + \mathrm{Cs}^{\mathrm{q}'+}, \tag{4.1}$$

where q' refers to the ionization state of the cesium. Since the ionization energy of Cs^{1+} is 3.9 eV this will be the main contribution. Higher ionizations are possible but cannot be distinguished in the measurement. We investigated this reaction with different charge states of carbon ($\mathrm{C}^{\mathrm{q}+}$: q=6,5,4,3) and bare oxygen (O^{8+}). The properties of the ions are summarized in table 4.1:

Ion	Energy [MeV/u]	v/c	lifetime τ [s]
C^{6+}	6.11	0.113	2000
C^{5+}	4.25	0.095	380
C^{4+}	2.72	0.076	220
C^{3+}	1.53	0.057	60
O^{8+}	3.03	0.085	455

Table 4.1: *Properties of the carbon ions used in the experiments.*

The energy denotes the total energy of the stored ion and τ the lifetime of the ion beam. The lifetime depends strongly on the ion species and is limited by collisions with restgas and interactions inside the electron cooler.

According to equation 3.4 introduced in section 3.3.3 the production rate of cesium ions is determined by $\sigma \cdot v \cdot n_{0,\mathrm{Ion}} \cdot N_{\mathrm{Cs}}(t) \equiv \Gamma_{\mathrm{Ion}} \cdot N_{\mathrm{Cs}}(t)$. In order to determine the cross section σ it is necessary to measure the decay rate Γ_{Ion} and the flux $v \cdot n_{0,\mathrm{Ion}}$. An example for the dependence of Γ_{Ion} and the ion flux (C^{6+}) is given in figure 4.1.

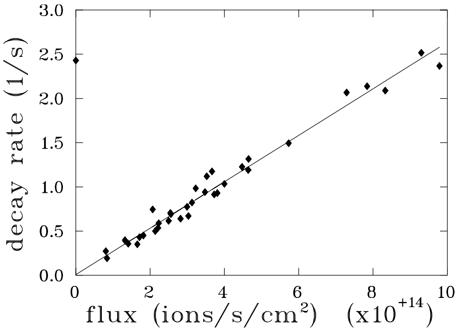

Figure 4.1: *The flux of C^{6+} is plotted versus the decay rate of the cloud. The slope of the straight line yields the cross section σ.*

The data analysis is discussed in detail in the following section. Here, the evaluation procedure is sketched shortly.

- Decay rate Γ_{Ion}

  The principle of the measurement has already been introduced in section 3.3.3 - the trap is loaded outside the ion beam until the steady state is reached. Then the cloud is moved into the ion beam and the count rate of the MCP is recorded until the equilibrium is reached (s. Fig. 3.8). From this curve the decay rate Γ_{Ion} is determined. The measurement is done several times with different ion beam currents. Since equation (3.4) is only valid for an ion beam density which is constant during the measurement the lifetime τ of the ion beam cannot be neglected. The decay of the ion beam itself will reduce the number of ionized cesium atoms. This has to be corrected to an non-decaying ion beam. The procedure is described in detail in section 4.1.1. Table 4.1 already indicates that the decay of the C^{6+} ion beam won't play a role during a measurement of $\approx 20\,\mathrm{s}$. But for C^{3+} the decay is not negligible.

- Ion flux

  The flux is determined by the restgas beam profile monitor. Therefore, the BPM has to be calibrated against the *Current Transformer (Bergoz, France)*. The calibration defines the ratio between the stored ion beam current and the count rate of the BPM in Hz/μA. Then the BPM can be used to measure the stored ion current and from the profiles the horizontal and the vertical widths of the ion beam can be determined. The flux can be calculated by these data. Since the BPM profiles are recorded after the decay measurement the profiles and the rates have to be shifted back in time and corrected to a non-decaying ion beam. This procedure will be discussed in more detail in section 4.1.1, too.

For the measurement of the cross section σ it is assumed that the atom cloud is moved to the center of the stored ion beam. Therefore, a two-dimensional scan (s. Sec. 3.3.4) has to be done first in order to determine the center of the ion beam.

The cross section σ can be determined by $\sigma = \Gamma \cdot \eta$ where η is the ion flux. The slope of the line in figure 4.1 yields the cross section σ. Since the flux can be evaluated by using the horizontal or the vertical BPM. One calculates two slightly different cross sections σ. Table 4.2 gives an overview of the measured cross sections and their mean values. The included errors represent the statistical errors and the systematic errors. The systematic error acts on all cross sections simultaneously. This will be discussed in detail in section 4.1.2. Appendix B shows the individual measurements of each cross section.

Ion	σ_{h} [10^{-15} cm^2]	σ_{v} [10^{-15} cm^2]	$\bar{\sigma}$ [10^{-15} cm^2]
C^{6+}	2.34	1.95	2.15 ± 9.5% ± 29%
C^{5+}	1.83	1.90	1.87 ± 7.5% ± 29%
C^{4+}	1.54	1.27	1.41 ± 9.5% ± 29%
C^{3+}	2.38	2.13	2.26 ± 5.0% ± 29%
O^{8+}	2.50	2.12	2.31 ± 7.8% ± 29%

Table 4.2: *Measured cross sections for the reaction* $C^{q+} + Cs \rightarrow C^{q+} + Cs^{q'+}$ *and* $O^{8+} + Cs \rightarrow O^{8+} + Cs^{q'+}$. *The indices h and v indicate the used calibration factor for the determination of the flux. The errors represent the statistical and the systematical error.*

4.1.1 Data Analysis and Results

Calibration of the Restgas BPM

The restgas BPM has to be calibrated in order to determine the count rate of the BPM per stored ion current. This is necessary because during the cross section measurement the ion current will be near the limit of the above mentioned Current Transformer and there is no possibility to read out the Current Transformer directly. Whereas the BPM is still able to provide reliable profiles during the measurements and can be accessed directly by the network.

A certain ion current is stored in the TSR, typically several μA. The value is taken from the Current Transformer which transforms the influenced charges by the stored ions into a current. This is an absolute value. For a fixed time the BPM signal is then recorded. This procedure is repeated for several different ion currents. Since the production of restgas ions depends on the restgas density and on the ion beam density the count rate of the BPM depends linearly on the stored ion current. Figure 4.2 shows an example of the calibration. The slope gives the calibration factor. Since the systematic offset of the Current Transformer can experimentally not be adjusted exactly to zero an ordinate offset occurs in figure 4.2. This offset has to be taken into account in the calibration. The integral count rate of each BPM spectrum is determined by a gaussian fit to the profile. The integrated rate is divided by the fixed measuring time. If a gaussian fit is used to determine the integral count rate the background can be substracted from the signal. Therefore, only counts of the BPM contributing to the signal are considered. If e.g. the sum of all counts would be used, the background of the BPM would be included. An example of the spectrum of the BPM is shown in figure 4.3 including the gaussian fit.

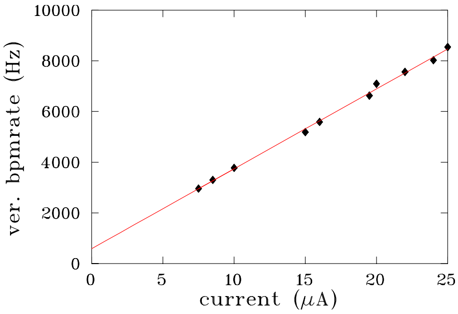

Figure 4.2: *The ion current is plotted vs. the BPM count rate. The slope yields the calibration factor in Hz/μA.*

Determination of the Decay Rate Γ_{Ion}

The decay rate of the atom cloud is determined from the count rate of the MCP which is recorded for a certain time. A typical spectrum of the count rate is shown in figure 4.4 a). At the beginning the cloud is outside the ion beam and the count rate is given by the ionization of the restgas. The cloud is then moved into the center of the ion beam. The decay of the atom cloud is monitored by the number of produced cesium ions which depends on the number of trapped particles $N_{\text{Cs}}(t)$

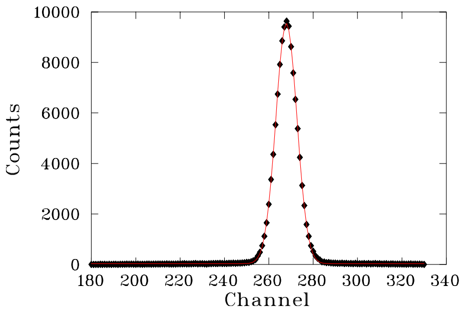

Figure 4.3: *Measured beam profile from the restgas BPM. The gaussian fit is used to determine the area of the gaussian distribution.*

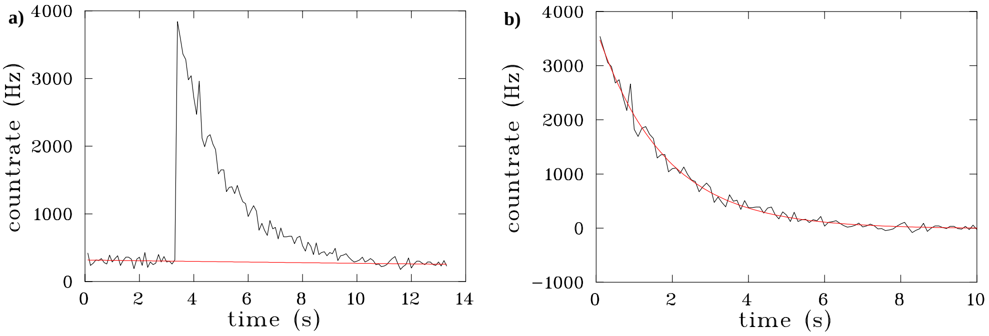

Figure 4.4: *a) Ion count rate measured by the MCP. At the beginning the cloud is outside the atom beam and is then moved into the center of the beam. The line indicates the ion signal corresponding to restgas. b) Count rate of the MCP monitoring the decay of the atom cloud. The restgas background is substracted.*

(s. Eq. (3.4)). The restgas background is substracted from the cesium signal. The fit to the restgas signal (the line in figure 4.4 a)) includes the decay of the ion beam which is given by the known lifetime τ. After the substraction the relevant part of the decay can be zoomed. Figure 4.4 b) shows the decay of the cloud without restgas background. We use the following equation to fit the measured count rates γ:

$$\gamma = \gamma_0 \cdot e^{-\Gamma_{\text{Ion}} \cdot t \cdot \exp(-t/\tau)} + C \tag{4.2}$$

$$\overset{\Gamma_{\text{Ion}} \gg 1/\tau}{\approx} \gamma_0 \cdot e^{-\Gamma_{\text{Ion}} \cdot t \cdot \left(1 - \frac{t}{\tau}\right)} + C. \tag{4.3}$$

γ_0 describes the maximum value of the decay at the very beginning, the constant C represents the equilibrium which is reached after a certain time and the exponential decay is given by the exponent $\Gamma_{\text{Ion}} \cdot t \cdot (1 - t/\tau)$. Since the decay rate Γ_{Ion} is affected with the ion beam's lifetime τ the last part of the exponent includes the expansion of the exponential beam decay.

Determination of the Ion Beam Size

The profiles of the stored ion beam are recorded for a fixed time (typically 20 s - 30 s) by the restgas BPM after the decay measurement. Since the control of the atom cloud and the measurement of the count rate is very time sensitive, it is necessary to measure the decay and the profile successively (s. Fig. 4.5). In this way we prevent priority conflicts in the experiment control. A simultaneous measurement leads to software problems and causes data losses either in the BPM signal or in the ion signal. Therefore, the count rate of the BPM has to be extrapolated in time since the ion beam has decayed during the first measurement. Similar to figure 4.3 a gaussian distribution is fitted to the measured beam profile in order to determine the integrated counts of the beam and its widths $\sigma_{\mathrm{x,y}}$. Using the integrated counts the current can be determined by the known calibration factor. For a measurement using an ion beam of C^{6+} the different widths vs. the integrated counts are shown in figure 4.6. In figure 4.6 a) the data from the horizontal BPM is shown, b) shows the vertical BPM. The dashed lines indicate the resolution limits of the BPM. Since the determination of the width of the ion beam is necessary for the calculation of the flux one has to make sure that the measured widths are well above the resolution limit of the BPM. Otherwise the width extracted from the deconvolution according to

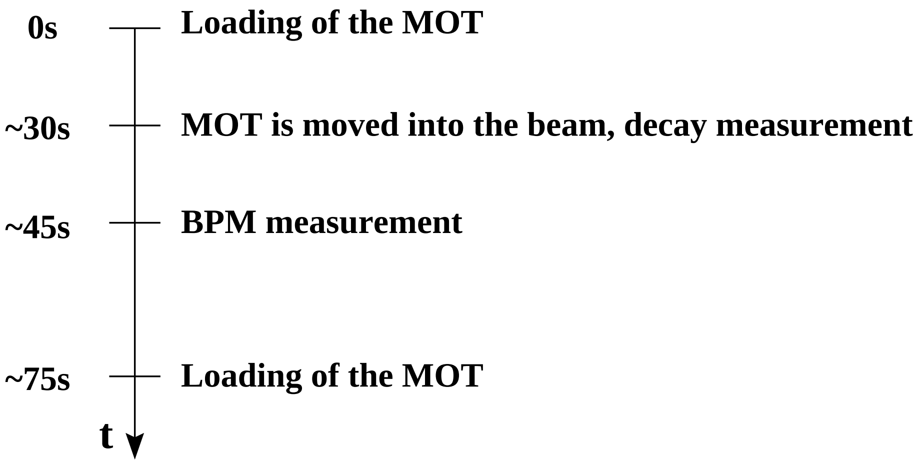

Figure 4.5: *Sequence of the measurement. The BPM is recorded after the decay of the atom cloud.*

$$\sigma_{\mathrm{Ion}} = \left(\sigma_{\mathrm{meas}}^2 - \sigma_{\mathrm{res}}^2\right)^{\frac{1}{2}} \tag{4.4}$$

is not reliable and as a consequence the flux and the collision cross section are not correct. Figure 4.6 b) indicates that for the vertical BPM some values are already

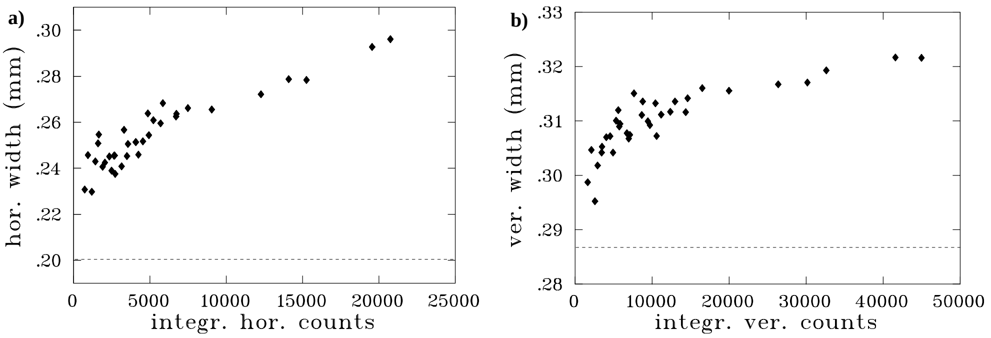

Figure 4.6: *Widths of the ion beam vs. the integrated counts. The horizontal BPM is shown in a) the vertical BPM in b).*

very close to the resolution limit. Therefore, it is necessary to know the resolution limit as good as possible. For the determination we use the constant ratio between the betatron amplitudes at the position of the BPM. In thermal equilibrium the dependence for the deconvoluted widths is described as

$$\left(\sigma^2_{\mathrm{h,meas}} - \sigma^2_{\mathrm{h,res}}\right)^{\frac{1}{2}} = a \cdot \left(\sigma^2_{\mathrm{v,meas}} - \sigma^2_{\mathrm{v,res}}\right)^{\frac{1}{2}}, \tag{4.5}$$

where $\sigma_{\mathrm{i,meas}}$ is the measured beam widths and $\sigma_{\mathrm{i,res}}$ describes the resolution limits. The ratio a between the deconvoluted widths is known to be constant (≈ 2) for all ion currents [Lauer, 1999]. For several horizontal resolution limits $\sigma_{\mathrm{h,res}}$ the parameter a and the vertical resolution limit $\sigma_{\mathrm{v,res}}$ are fitted. Only in a narrow interval of $\sigma_{\mathrm{h,res}}$ the factor a is close to 2 and independent of the ion current. From the fit we obtain a horizontal resolution limit of 200 μm and a vertical limit of 287 μm. The uncertainty of the limits is 2%.

Furthermore, the betatron oscillation changes the width of the ion beam at different positions inside the storage ring. Therefore, the measured distribution has to be transformed from the position of the BPM to the position of the trap. The transformation factors are taken from a simulation of the lattice of the TSR. Since the lattice is not known in all details - e.g. the fields of the magnets cannot be exactly measured - the error of the transformation factors is about 20%. The measured widths $\sigma_{\mathrm{x,y}}$ of the ion beam at the restgas BPM are transformed according to

$$\begin{aligned} \sigma_{\mathrm{x,MOT}} &= \sigma_{\mathrm{x,BPM}} \cdot 1.68(\pm 20\%), \\ \sigma_{\mathrm{y,MOT}} &= \sigma_{\mathrm{y,BPM}} \cdot 1.07(\pm 20\%). \end{aligned} \tag{4.6}$$

This error can be reduced if the atom cloud is used to measure directly the width of the beam. In these measurements we used the BPM because the analysis of the profile measurement was not completed in detail, yet.

Evaluation of the Flux η

The cross section σ is determined by $\Gamma_{\text{Ion}}(\vec{r_0}) = \sigma \cdot \eta(\vec{r_0})$, where $\eta(\vec{r_0}) = v \cdot n_{\text{Ion}}(\vec{r_0})$ at the position $\vec{r_0}$ of the atom cloud. As already mentioned in section 3.3.3 $n_{\text{Ion}}(\vec{r_0})$ results from an overlap integral of the density distribution of the trapped atoms and the ion beam (s. Eq. (3.2, 3.3)). Since the deconvoluted widths of the atom cloud and the ion beam have to be included in $n_{\text{Ion}}(\vec{r_0})$ the problem for the determination of the beam width causes a large error at a low ion flux. The widths of the atom cloud is measured by a CCD-camera. The measured width of the cloud is high above the resolution of the camera system. The contributed error caused by the deconvolution of this widths can be neglected against the error of the beam widths.

The cross section is determined from the slope of the straight line in figure 4.1 [1]. The ordinate offset is given by the decay rate of the cloud without any stored ions, i.e. the decay is caused by collisions with restgas.

4.1.2 Statistical and Systematic Errors

In the data analysis one has to distinguish carefully between statistical and systematical errors. The statistical errors are given by the evaluation steps of the analysis while the systematical error is caused by the transformation factors from the TSR lattice simulation.

Statistical Errors

- Calibration of the restgas BPM

  The statistical error for the calibration of the BPM vs. the Current Transformer can be determined from the deviation of the linearity shown in figure 4.2. The deviation yields a relative error of 4% for the calibration factor.

- Determination of the decay rate Γ_{Ion}

  A statistical error for the determination of the decay rate Γ_{Ion} is again given by the error of the fit. The deviation of the fit using equation 4.3 yields a statistical error of 1% for the decay rate.

- Determination of the ion beam size

  The statistical error for the determination of the width of the ion beam is given by the deviation of the gaussian fit to the beam profile shown in figure 4.3. The fit yields an error of 2% for the determination of the width and

---

[1] The measured decay rates dedicated to 0 flux in the spectra belong to measurements where the BPM signal was not recorded and therefore no flux could be determined.

an error of 2% for the determination of the amplitude. As shown before an error of 2% for the resolution limits of the BPM has to be included.

Systematic Errors

The systematic error originates from the transformation factors which convert the ion beam width from the position of the BPM to the position of the trap. For the transformation factors an error of 20% is expected because of the mentioned uncertainties in the simulation.

Evaluation of the Cross Section σ

For the evaluation of the cross section the flux has to be derived. The deconvoluted widths of the ion beam is used to calculate the area (A) of the beam and the according flux. For the deconvolution the horizontal limit is assumed to be 200 μm and 287 μm for the vertical limit. Figure 4.7 shows an example for C^{6+} where the mentioned statistical errors are included, too. Two boundary conditions have to be fulfilled: The data must follow a linear dependence and the straight line must include the decay of the atom cloud caused by restgas collisions, i.e. at 0 flux. The offset does not include neither errors from the resolution limit nor from the transformation factor.

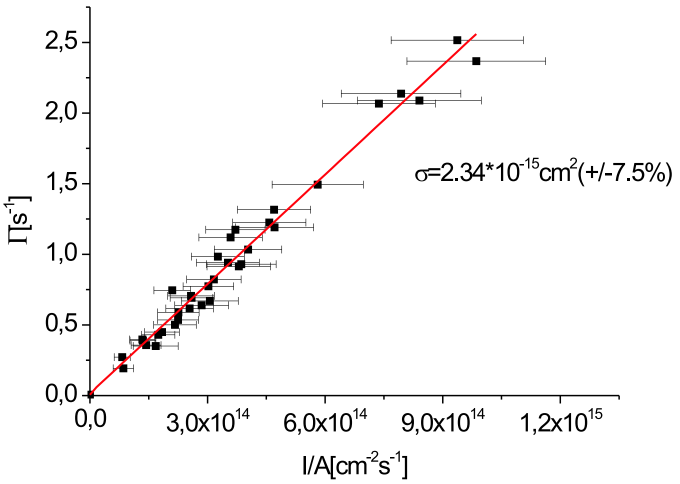

Figure 4.7: *Decay rate vs. ion flux with statistic errors (projectile: C^{6+}). The BPM resolutions are 200 μm (hor) and 287 μm (ver).*

Clearly, all the requirements are satisfied by the fit. As a check for consistency whether the assumed resolution limit for the horizontal BPM is correct the limit is varied. Since the ratio between the widths of the BPM has to remain constant both resolution limits have to be shifted. The change of the resolution limit of the BPM changes the derived beam area (A). The result is shown in figure 4.8. In this figure the horizontal limit is 210 μm and the vertical limit is 295 μm. Obviously, the evaluated flux is shifted. The linear fit is still valid but the ordinate offset is not included correctly. This is a clear indication that the assumed horizontal resolution limit is wrong. The shift is already obvious if the assumed resolution limits deviates by 2% from 200 μm (horizontal resolution) and 287 μm (vertical resolution). As a consequence, the error of the total collision cross sections is mainly determined by the statistical errors in the data evaluation. They are in the order of 8%. The results are summarized in figure 4.9. The shown cross sections are derived using the calibration factor from the horizontal BPM. The error bars include the statistical errors and the error of the remaining uncertainty of the resolution limit. The systematical error caused by the transformation factors is indicated by the upper and lower limits for the measured cross sections. Note that this systematic error affects all cross sections in the same way. In addition to the check of the resolution limits errors in the measured beam width become directly visible as a deviation from the linearity. Appendix E gives an example for the deviation.

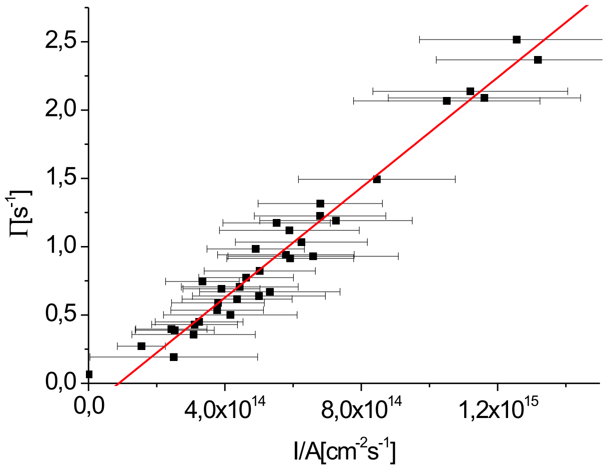

Figure 4.8: *Decay rate vs. ion flux with statistic errors (projectile: C^{6+}) assuming a resolution limit of 210 μm (hor) and 295 μm (ver).*

4.1.3 Comparison to Theory

In figure 4.9 the comparison between the measured cross sections and the calculated values is shown. The calculations have been done by V.P. Shevelko using the LOSS-code [Tolstikhina and Shevelko, 2000a]. Perturbation theory in first order is used by this code. The needed wave functions were determined by a numerical solution of the radial Schrödinger-equation [Shevelko et al., 2001].

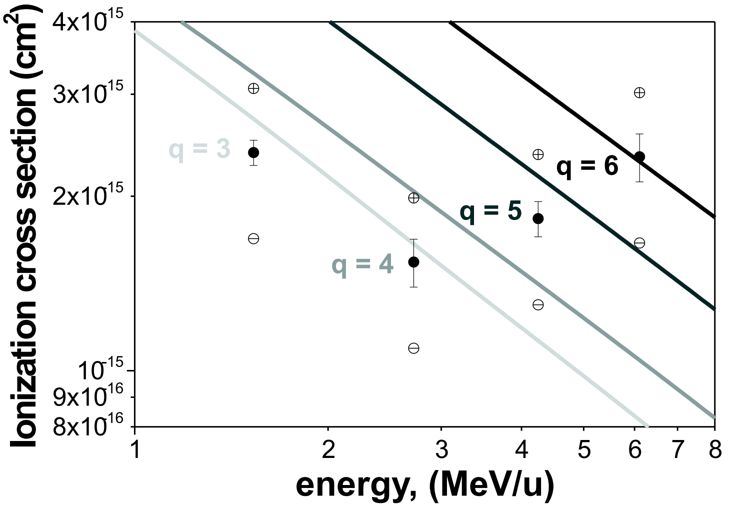

Figure 4.9: *Comparison of theory and measurement. The cross section is plotted against the energy of the projectile. The cross section are derived using the calibration factor from the horizontal BPM. The error bars include the statistic errors and the systematic errors are given by the lower ($\ominus$) and upper ($\oplus$) limits of each cross section.*

The calculations and the measurements are in very good agreement apart from the measured cross section for C^{4+}. Until now it is not clear where this discrepancy comes from.

The measurements which have been shown here are the first test of the theory in this energy region of the projectile and for a target as heavy and complicated as cesium. Concerning the 55 electrons of the cesium target several considerations and scaling laws had to be used in the calculation. Although the results agree very well it has to be clarified why C^{4+} differs from the calculation concerning the cross section for the ionization and for electron capture (s. Sec. 4.2).

The systematic error in figure 4.9 is given by the transformation factors of the betatron amplitude. These error shifts all the measured values simultaneously. The minimum ($\ominus$) and the maximum ($\oplus$) of the possible shift is shown.

For the cross section of bare oxygen (O^{8+}) is no theory available, yet.

4.2 Measurement of the Electron Capture Cross Section

Compared to the ionization of the target the process of single electron capture from the target is less probable by some orders of magnitude. With these projectile energies (s. Tab. 4.1) only electron capture from inner shells is possible: The impact parameter has to be very small and, therefore, the probability decreases.

In order to distinguish the cesium ions produced in a capture process from the direct ionization we measure coincidentally the reloaded projectile ions and the cesium ions. The setup for this measurement is shown in figure 4.10 using C^{6+} as a projectile. In addition, this coincidence measurement gives us the opportunity to determine the time the cesium ions need to reach the MCP. From the time-of-flight (TOF) measurement we can deduce the final charge state of the cesium ions and the relative occurrence of each state.

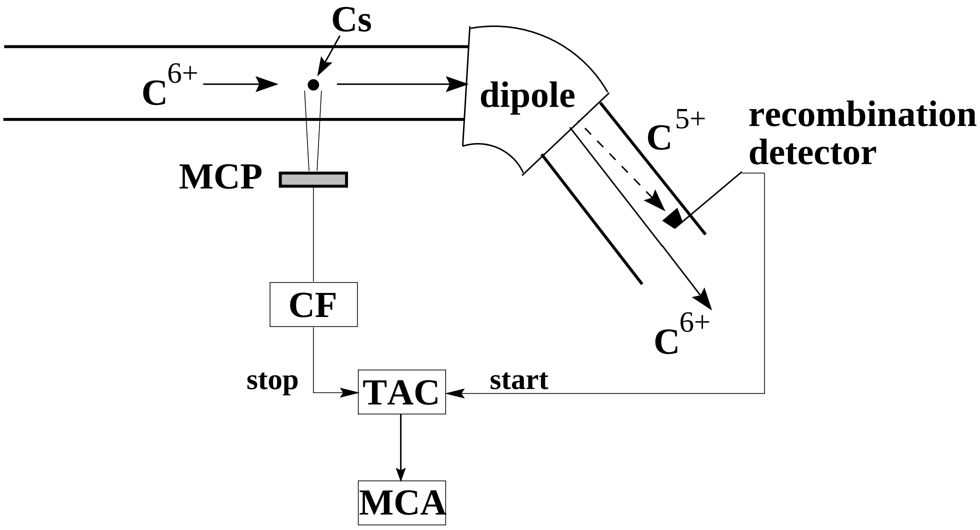

Figure 4.10: *Experimental setup of the electron capture measurement. MCP: Micro channel plate, CF: Constant fraction, TAC: Time-to-amplitude converter, MCA: Multi channel analyzer.*

Measurement Procedure

The ion beam is injected into the storage ring and is cooled by the electron cooler for 10 s. Simultaneously, the trap is loaded outside the ion beam until a steady state is reached. Since the electron cooler causes a substantial background of reloaded ions, it is switched off and then the cloud is moved into the ion beam. For 0.2 s the cloud remains inside the beam and is then moved out again. This time is short enough that the ion beam is not enlarged by intra-beam scattering and thus the ion flux is constant. Finally, the ion beam is kicked out of the storage ring. During the measuring time of 0.2 s the counts of the MCP are recorded. The signal of a reloaded ion serves as a start trigger for the TOF measurement. The signal of the MCP within a certain gate serves as a stop trigger. Both signals are given into a time-to-amplitude converter (TAC). This amplitude is transferred to the channel of a multi-channel-analyzer (MCA) which then yields a spectrum of the different flight times of the cesium ions. Figure 4.11 shows the spectrum for electron capture of C^{6+}:

$$C^{6+} + Cs \rightarrow C^{5+} + Cs^{q+}.$$

The figure resolves clearly the different final charge states of the ionized cesium.

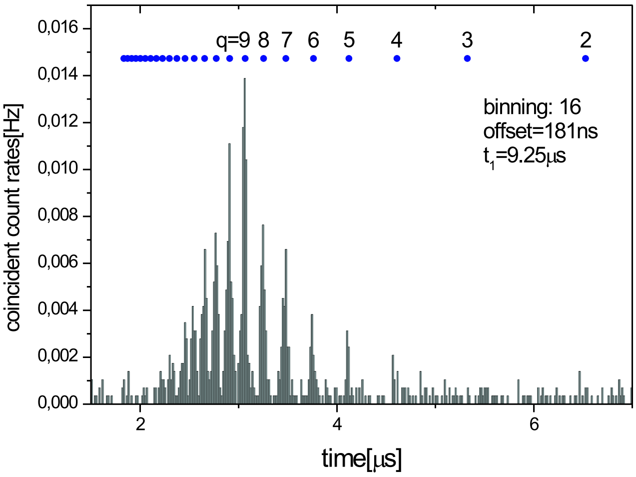

Figure 4.11: *Spectrum of the final charge state of the cesium ions. The highest peak belongs to* Cs^{9+} *and the charge decreases to the right. The calculated position of each charge is indicated by the points.*

In addition, the relative probabilities for each charge state are included. For the electron capture of C^{6+} the most probable final charge state of the cesium is Cs^{9+}. The points added in figure 4.11 correspond to the expected positions of the cesium charge states. Their time dependence is $t_{q+} = t_1/\sqrt{q}$, where t_1 describes the TOF for Cs^{1+}. The time t_1 is obtained by the calibration described in section 3.1.1. The points are in very good agreement with the measured data.

In addition to the final charge state distribution the comparison of the total count rate of the MCP and the coincident count rate yields the ratio of ionization to electron capture and thus the cross section for electron capture can be calculated.

The same measurement has been done for a C^{4+} projectile. The results are shown in figure 4.12. Although the statistics is not very good the different charge states can be identified. The highest peak corresponds to Cs^{6+}. Nevertheless, the ratio between electron capture and ionization can be determined. The results for both measurements are summarized in table 4.3. For the calculation of the electron capture cross section σ_{ec} we took into account that the detection efficiency of the MCP changes with higher cesium charge states. Since the energy of the

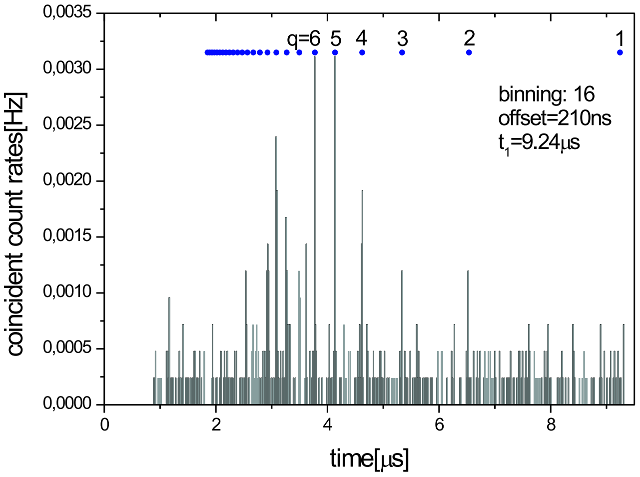

Figure 4.12: *Spectrum of the final charge state of the cesium ions after an electron capture occurred. The highest peak belongs to* Cs^{6+} *and the charge decreases to the right. The calculated position of each charge is indicated by the points.*

Ion	$\bar{\sigma}_{\mathrm{ion}}$ $[10^{-15}\,\mathrm{cm}^2]$	ratio ion : ec	rel. efficiency	σ_{ec} $[\mathrm{cm}^2]$
C^{6+}	2.15	257 : 1	2.8	2.99×10^{-18}
C^{4+}	1.41	3460 : 1	2.7	1.51×10^{-19}
O^{8+}	2.31	279 : 1	3.0	2.76×10^{-18}

Table 4.3: *Measured ionization cross section* σ_{ion} *, measured ratio between ionization and electron capture and extracted electron capture cross section* σ_{ec}. *The capture cross section includes increasing efficiency for higher cesium charge states.*

ions increases the efficiency of the MCP increases, too. The assumed efficiency factor is deduced from the most probably final charge state in the described capture processes. Figure 4.13 shows the used efficiencies from [Proxitronic, 2002].

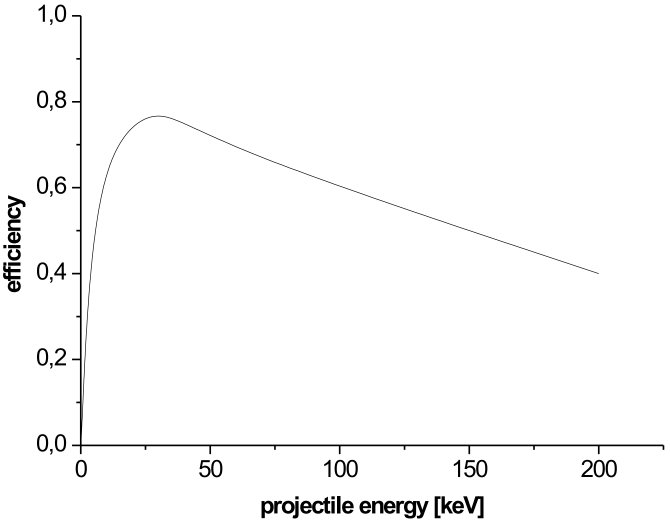

Figure 4.13: *Efficiency of the MCP for different energies of the projectile.*

4.2.1 Comparison to Theory

In figure 4.14 and figure 4.15 the calculated cross sections for electron capture using C^{6+} and C^{4+} as a projectile are shown. The figures show the contribution of each shell to the total cross section for a certain projectile energy.

The cross sections are calculated by V.P. Shevelko using the CAPTURE-code [Tolstikhina and Shevelko, 2000b]. The vertical and horizontal line in each figure indicate the energy and the corresponding cross section for our experiments. For C^{6+} this yields a cross section $\sigma_{\mathrm{calc},C^{6+}} = 2.5 \times 10^{-18}\,\mathrm{cm}^2$. This value is in good agreement with our measurement where we obtained $\sigma_{\mathrm{meas},C^{6+}} = 2.99 \times 10^{-18}\,\mathrm{cm}^2$. In addition, figure 4.14 indicates that at our actual energy the inner shells 3s, 3p and 3d (corresponding to the M-shell) give the largest contribution to the cross section.

However, for C^{4+} the calculated value is $\sigma_{\mathrm{calc},C^{4+}} = 1.9 \times 10^{-18}\,\mathrm{cm}^2$. The calculation shown in figure 4.15 indicates that the main contribution to the cross section is given by the shells 3p,3d and 4p (corresponding to the M-shell and the N-shell). The comparison with the measured value reveals a contradiction

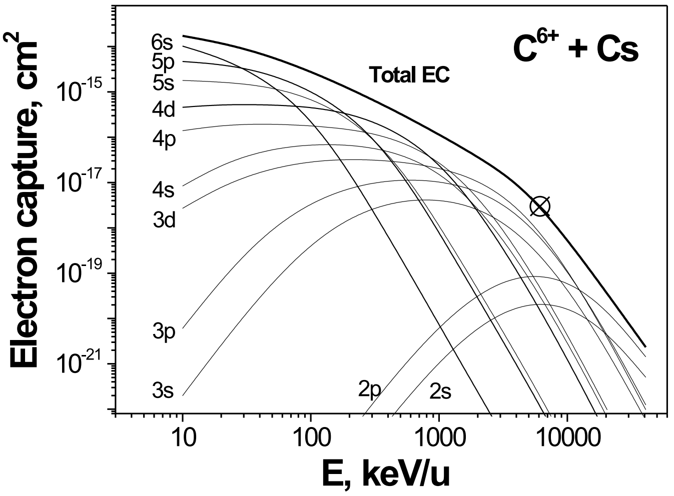

Figure 4.14: *Calculated cross section for electron capture of a C^{6+}-ion at a given energy. The contribution of each shell is included. The calculation is done by V.P. Shevelko. The measured cross section is indicated by the plotted data point.*

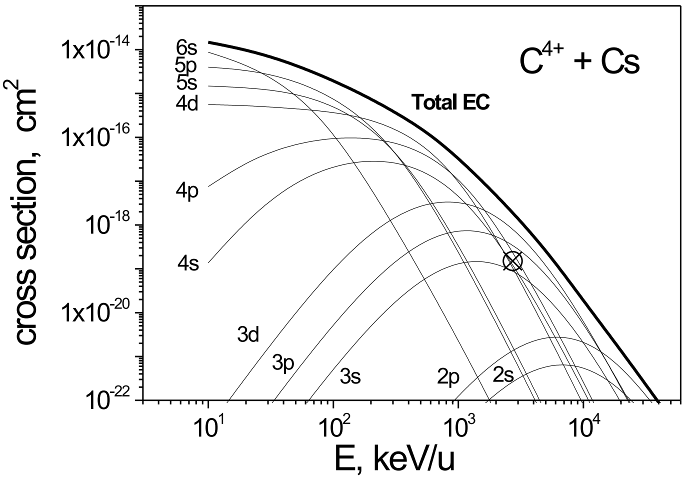

Figure 4.15: *Calculated cross section for electron capture of a C^{4+}-ion at a given energy. The contribution of each shell is included. The calculation is done by V.P. Shevelko. The measured cross section is indicated by the plotted data point.*

because the measured cross section is $\sigma_{\mathrm{meas,C^{4+}}} = 1.51 \times 10^{-19}\,\mathrm{cm}^2$. Even if the calculated value for the ionization of cesium by C^{4+} would be used (s. Fig. 4.9) to calculate the electron capture cross section the result would still be one order of magnitude smaller than expected according to the calculation. It is still not clear what the discrepancy causes.

The error of the measured cross section has not been investigated, yet. Therefore, error bars still have to be evaluated.

4.2.2 Transverse Momentum of the Recoil Ion

The width of the peaks on TOF spectrum includes two additional information. It is a convolution of the extension of the atom cloud and of the momentum transferred to the recoil ion during the collision process. This becomes even more obvious if the final charge state of the recoiled ion gets higher and thus the transferred momentum increases, too. The TOF spectrum then shows a double peak structure for several charge states. An example which shows the spectrum for the reaction

$$\mathrm{O}^{8+} + \mathrm{Cs} \rightarrow \mathrm{O}^{7+} + \mathrm{Cs}^{q+}$$

is shown in figure 4.16. The ion are ejected from the cloud on a plane perpendicular to the ion beam with an azimuthal symmetry. If the transfer of momentum to

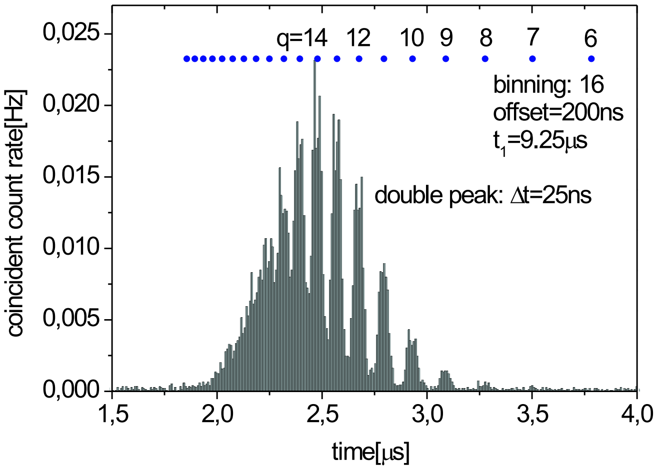

Figure 4.16: *Spectrum of the final charge state of the cesium ions after an electron is captured by the O^{8+}. The double peak structure makes it possible to determine the momentum transfer to the recoil ion.*

recoil ion increases the number of cesium ions which reach the MCP is reduced. The electrodes in front of the MCP filter the ions which are not on a path directly towards the MCP or in the opposite direction. The principle is shown in figure 4.17. The difference in the flight time of these two remaining pathes includes the information on the transferred recoil momentum. From this difference we calculate an energy transfer to the recoil ion in the order of $\approx 1\,\mathrm{eV}$. This leads to a momentum transfer of $\approx 2.65 \times 10^{-22}\,\mathrm{kg{\cdot}m{\cdot}s^{-1}}$ to the recoiled cesium ion. The time difference of about 25 ns corresponds for Cs^{14+} to a difference in the path length of $15\,\mu$m, i.e. the cesium ion arriving later is elongated by $7.5\,\mu$m in the direction opposed to the MCP. If the ion leaves the cloud with a momentum pointing up, i.e. perpendicular to the direction of the MCP the ions are elongated for about 2 mm. The opening of the first electrode in front of the MCP has a diameter of 12 mm. Compared to the elongations this indicates that only a few cesium ions are filtered by the electrodes. The spectrum in figure 4.16 shows that the double peak structure is rather narrow and only the center of the peak is missing. This missing part belongs to the filtered ions.

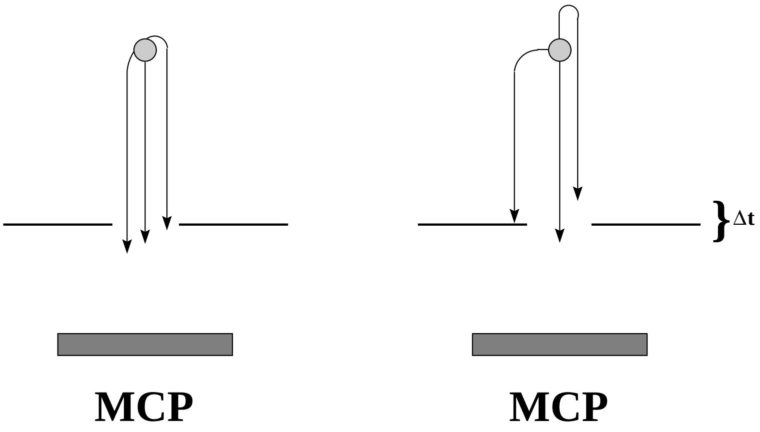

Figure 4.17: *If the momentum transfer to the recoil ion increases the electrodes in front of the MCP block several ion paths. Only ions which are accelerated directly towards the MCP or in the opposite direction hit the detector.*

Since the distance between the double peaks is very small the determination of the time difference is limited. The resolution of this method is given by the possibility to distinguish two peaks. In the whole spectrum the peaks are very close. Although it is possible to resolve the double peak structure the determination of the different flight times includes a large error. The determination of the center of the peak is only possible with a resolution of ≈ 5 ns. The uncertainty is given by the width of the peak itself which is mainly caused by the binning procedure. 16 channels of the MCA spectrum are binned in figure 4.16. This corresponds already to a width of 8.5 ns. Assuming that the center of the peak is determined exactly an uncertainty of ≈ 4.5 ns has to be expected for each peak. As a consequence the difference for the time-of-flight is $\Delta t = 25\,\mathrm{ns} \pm 9\,\mathrm{ns}$. In this respect only the order of magnitude can be given for the momentum transfer. If the binning is reduced the spectrum gets even more diffuse and the peaks cannot be correctly determined anymore. For further investigations it is necessary to increase the resolution in time by zooming into the spectrum, i.e. only a small part of the spectrum has to be recorded by the MCA.

Nevertheless, the double peak structure of the spectrum of the projectile O^{8+} is a clear indication that the momentum transfer to the recoil ion is higher than e.g. for the projectile C^{6+} where no structure can be identified. This means that in the first case the impact parameter of the collision is smaller compared to C^{6+}. In addition, the smaller impact parameter indicates that for O^{8+} the electron is captured from the innermost shells (K- or L-shell) since for C^{6+} the M-shell has the highest contribution. Besides, the most probable final charge state of the cesium is higher (q=14) than for C^{6+} (q=9). Again, this is an indication that the electron is captured from one of the shells below the M-shell.

Chapter 5

Conclusions and Outlook

This work presents the first successful implementation of a magneto-optical trap (MOT) for cold atoms into a storage ring. The system works very reliable under beamtime conditions and the experiments have shown that laser-trapped atoms are an excellent target for collision experiments with projectiles at energies of some MeV/u. The trapped atoms are well localized and their position can be precisely controlled.

The atom cloud has been employed as a probe to scan the ion beam. The ionization rate of the trapped cesium is monitored as a function of the position of the cloud. The scan yields the density distribution of the ion beam. The spatial resolution of the profile measurement is only limited by the size of the cloud. Currently, the cloud has a diameter of $\approx 450\,\mu$m. The resolution of the measurement is already better compared to the restgas beam profile monitor (BPM) [Hochadel, 1994] at the TSR and the sensitivity to imperfections, e.g. in the alignment of the electron cooler and the ion beam, is much higher compared to the BPM. Since the two-dimensional density distribution is monitored an inhomogeneity in the ion beam induced by the electron cooler can be clearly identified whereas the integral method of the restgas BPM shows a perfect ion beam. Nevertheless, the spatial resolution of our measurement can still be improved by reducing the size of the cloud. This can be done by increasing the gradient of the quadrupole trap field. The increase reduces the cloud size [Townsend et al., 1995] and thus the spatial resolution increases. The profile measurement has been applied to ion beam currents in the order of several nA (corresponding to $\approx 10^4$ C^{6+}-ions). The restgas BPM is already limited to currents of $1\,\mu$A ($\approx 10^6$ C^{6+}-ions). During the experiments it turned out that the scan of the ion beam cannot be applied to currents higher than the used several nA. The reduction in the number of trapped atoms during the scan leads to a lower ionization rate which is not caused by the lower local ion beam density but by the reduced particle number in the trap. As a consequence, the beam profile is not imaged correctly. Therefore, one has to make sure that the reduction of the number of trapped particles is small during the scan, i.e. the ion beam current has to be low. Nevertheless, it is possible to measure higher ion beam currents using a different technique. The ionization rate can be determined stepwise: The trap is loaded outside the ion beam and is then moved to the measuring position. The decay of the cloud is recorded. Afterwards, the trap is loaded outside the beam again. In this way the beam profile can be determined for ion currents up to some μA. This procedure however is much more time consuming than the direct scan. Alternatively, a redesign of the loading section would make it possible to increase the loading flux.

Total collision cross section have been determined by monitoring the decay of the atom cloud depending on the ion flux. The total cross sections can then be evaluated without any assumptions. The results agree very well with theoretical predictions. The flux determination includes the width of the ion beam measured by the BPM. Since the properties of the atom cloud as a beam profile monitor were not known in detail during the collision experiments the BPM has been used to determine the beam width. It turned out that in our experiments the width of the ion beam was already close to the resolution limit of the BPM. For the flux evaluation the measured beam width is deconvoluted to the real width of the beam. If the measured width is already close to the resolution limit the deconvoluted width gets rather small but the uncertainty becomes large. This we have to improve by using broader beams which are well above the resolution limit of the BPM. Furthermore, the beam width at the position of the BPM has to be transformed to the position of the trap. In our experiments we used a transformation factor which is given by the simulation of the TSR lattice. This factor includes an error of 20% because the lattice is not known in all details. We can overcome this limitation by measuring the width of the beam directly with the atom cloud which will be done in future experiments.

Electron transfer from the target to the projectile has been studied by applying a coincidence technique. The coincidence of the reloaded projectile and the ionized cesium atom are used to measure the coincident rates and the time-of-flight of the cesium ions. From the time-of-flight spectrum momentum transfer and the charge state of the recoiled ion are determined. The ratio between the coincident rate and the total ionization rate yields the cross section for the capture process. For the measurement one has to make sure that electron capture from the electron cooler is suppressed. Therefore, the electron cooler is switched off before the cloud is moved into the ion beam. Since the ion beam expands due to intra beam scattering [Sørensen, 1987] the window for the actual measurement is very short. In fact, the measurement takes 0.2 s after 10 s of electron cooling. After the measurement the beam is kicked off the ring. Consequently, the duty cycle of the measurement is not very efficient. The efficiency can be enhanced if the role of the recombination detector and the MCP in the coincidence measurement is inverted. The time-of-flight of the cesium ions is now known and so the MCP signal can be used as the start trigger and the recombination signal which has to be electronically delayed sets the stop trigger. In this way one can distinguish between capture from the electron cooler and the trapped atoms. Therefore, it is not necessary anymore to switch off the electron cooler and to use a new injection for each measurement. The measurement can be done with a much higher duty cycle.

Cross sections for the production of recoil ions have already been measured for collisions of e.g. argon and xenon with highly charged uranium at high velocities (3.6-15.5 MeV/u) [Kelbch et al., 1985]. A recoil-ion/projectile-ion coincidence technique made it possible to distinguish between pure ionisation of the target and ionisation of the target plus capture of one or more electrons into a bound state of the projectile. Time-of-flight measurements were used to resolve the produced recoil ion charge states. The results and the used techniques are summarized in [Ullrich, 1994]. We use the same coincidence techniques in our experiments and find good agreement with the resolution of the time-of-flight measurements and the possibility to distinguish the produced recoil ion charge states.

The ultracold target has become a reliable device which can be used for high precision measurements. In principle, one can investigate all ion species which can be stored in the TSR. It is even possible to take part in the beamtime of another experiment with the target because no disturbance of the ion beam has been identified.

In the near future, the current setup will be used to investigate collisions between singly charged molecular ions and ultracold cesium atoms. Electron transfer to the molecular ion can be studied applying the approved coincidence technique. In addition, a position sensitive detector can be used for the reloaded projectile [Zajfman et al., 1995]. The position sensitive measurement of the neutral projectile makes it possible to determine its scattering angle. The measured scattering angle would provide additional information on the momentum transfer during the collision. At the moment, it is neither clear whether the resolution of the detector is sufficient nor whether the probability of electron capture is high enough for molecular ions at energies of MeV/u.

The negligible thermal motion of the ultracold target has not played a role in any of the measurements mentioned. The implementation of additional detectors in order to do RIMS [Ullrich et al., 1997] is not possible at the current position of the trap inside the TSR. Although the laser-trapped atoms are ideally suited for experiments using the RIMS technique, the magnetic stray fields present at the current position make it impossible to do measurements of e.g. the recoiled electrons. For RIMS experiments it would be necessary to move the trap to a straight section of the TSR where no magnets are present. An alternative would be the implementation as a single-pass experiment into a beam line, like e.g. the extraction section of the TSR [Albrecht, 1996].

The technique of laser-trapped atoms which is present at our laboratory can be used for other alkalis, too. In fact, laser-cooled lithium has a much simpler internal structure and theory has to deal only with three electrons instead of 55. Therefore, lithium is very promising as a target in MOTRIMS experiments [Schünemann et al., 1996]. One step further would be to use not a magnetooptical trap but an optical dipole trap to provide ultracold target atoms [Grimm et al., 2000]. In a dipole trap one has full control of the internal degrees of freedom and no magnetic trapping fields are present. Collision experiments with ultracold atoms in a well defined internal state would become possible.

Appendix A

Detailed Drawing of the Ion Detector and the Electrostatic Lens System

The engineering drawings have been done by J. Kleinert [Kleinert, 2002] using the Linux program *QCAD*.

Gesamtansicht des Ionendetektors

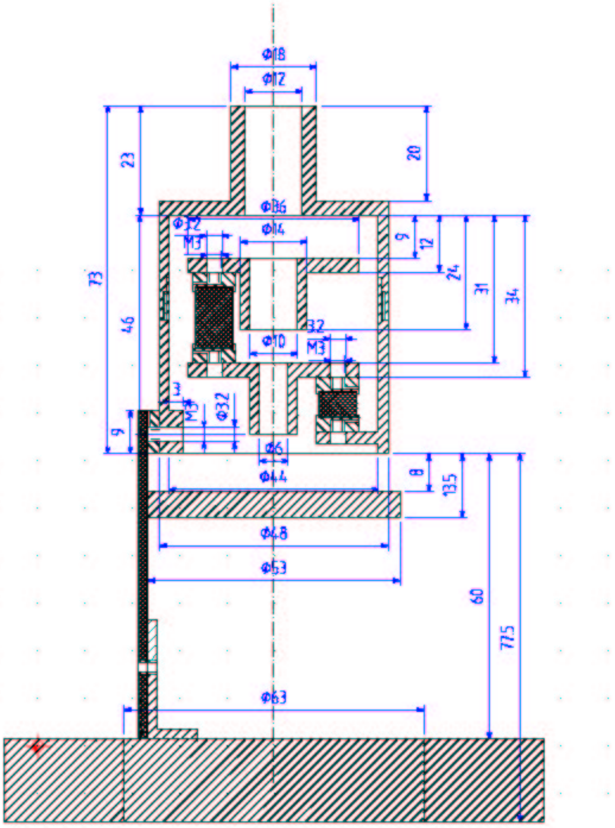

Elektrode aussen

Teil 1

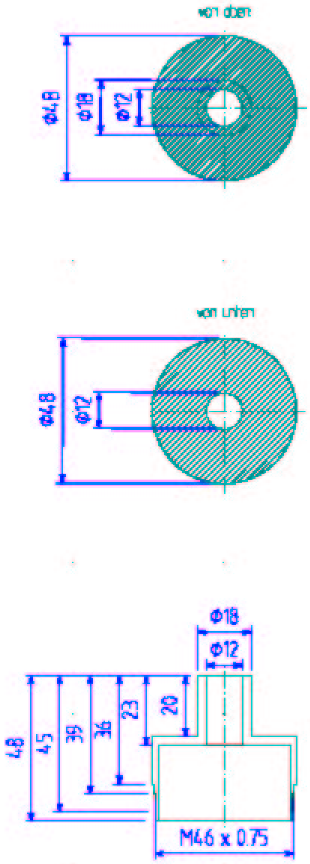

Teil 2

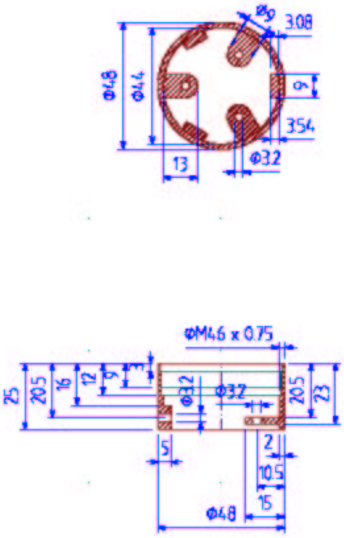

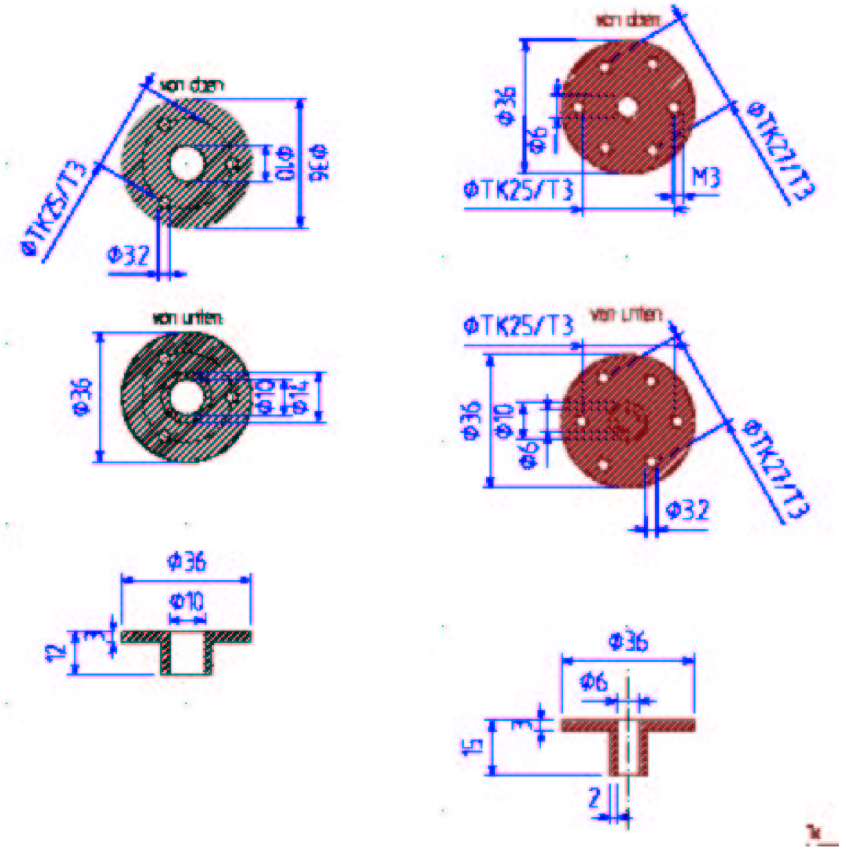

Elektroden innen

Teil 1 **Teil 2**

Keramiken

Keramikhalterung aussen

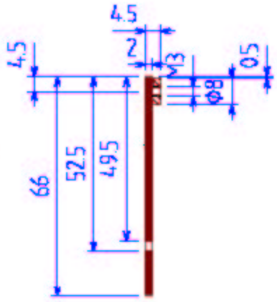

3 x

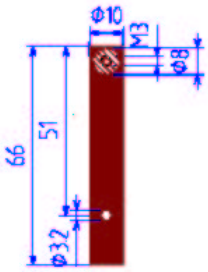

Keramikhalterungen innen

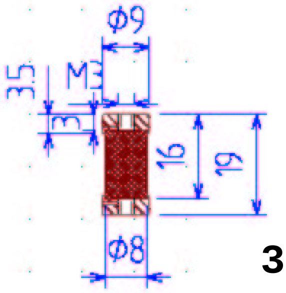

3 x

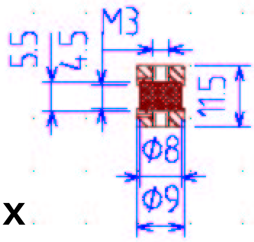

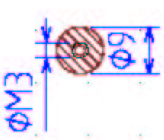

3 x

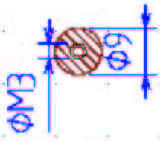

Flansch

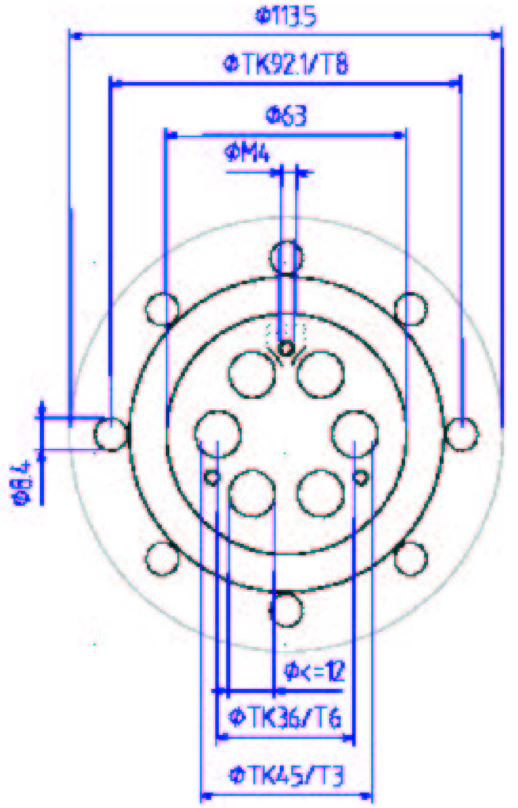

Uebergangsstueck
Flansch - Keramikhalterung

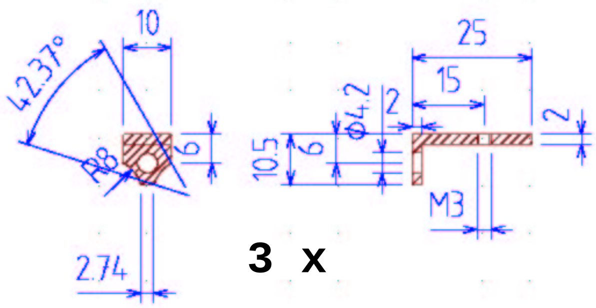

3 x

Appendix B

Measurement of the Cross Sections

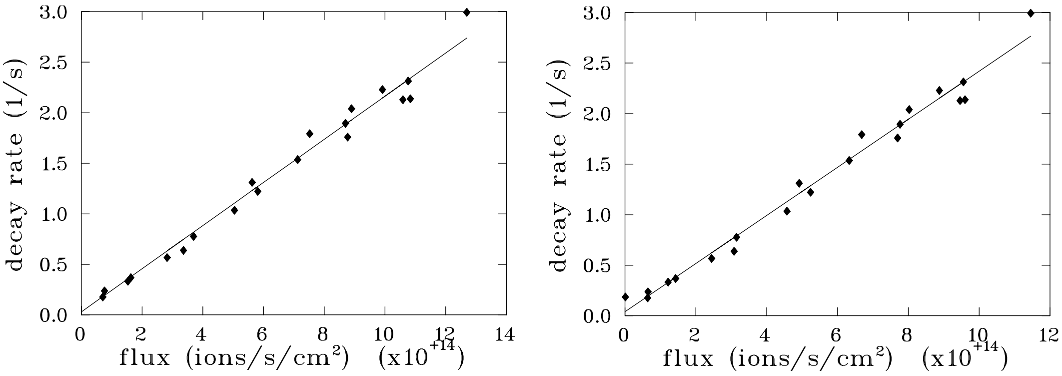

Figure B.1: Measurement of the cross section for C^{3+}. The data using the vertical BPM for the flux determination is shown to the left, the horizontal BPM is shown to the right.

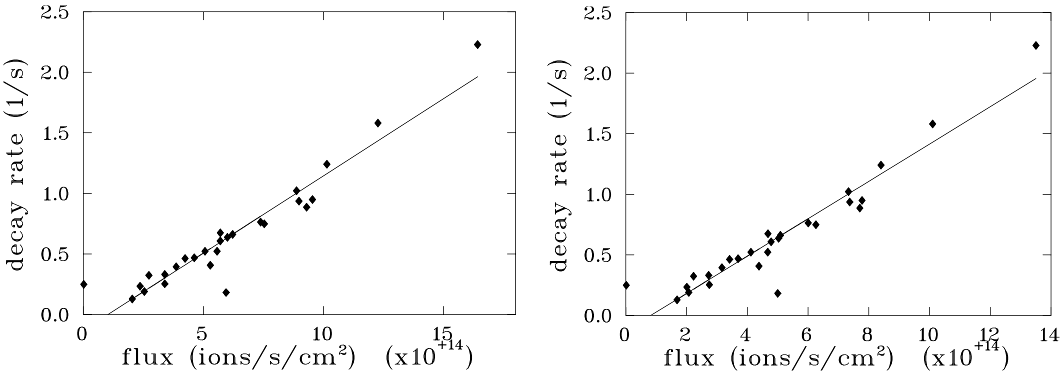

Figure B.2: Measurement of the cross section for C^{4+}. The data using the vertical BPM for the flux determination is shown to the left, the horizontal BPM is shown to the right.

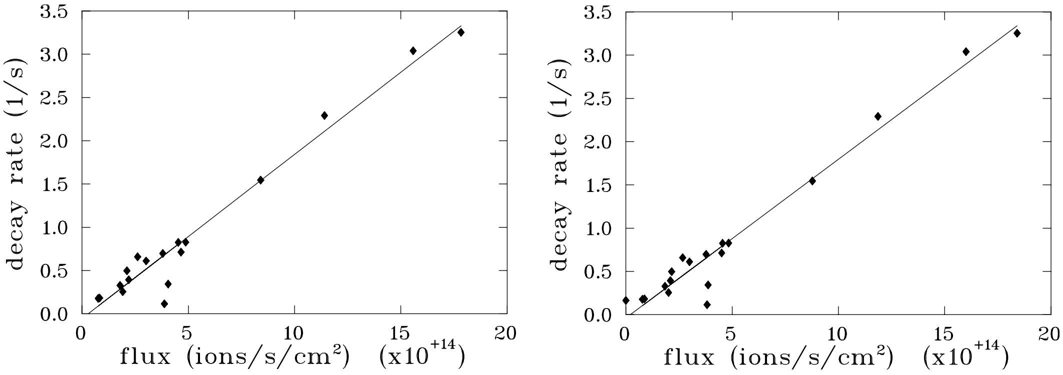

Figure B.3: Measurement of the cross section for C^{5+}. The data using the vertical BPM for the flux determination is shown to the left, the horizontal BPM is shown to the right.

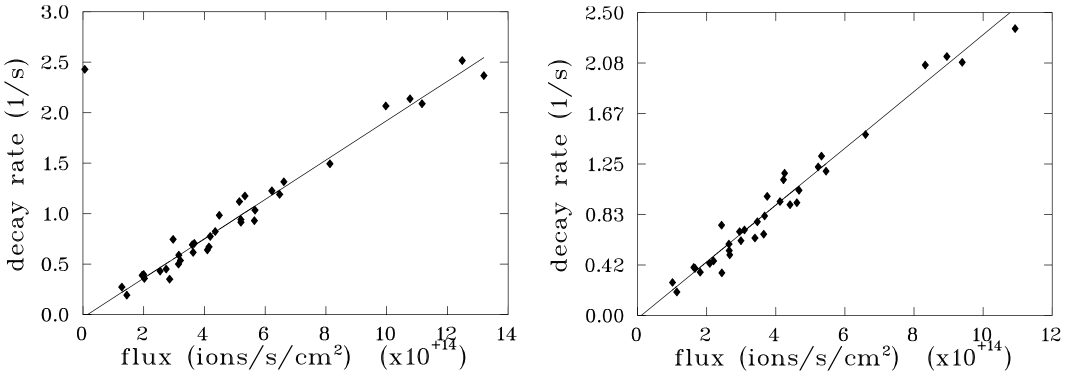

Figure B.4: Measurement of the cross section for C^{6+}. The data using the vertical BPM for the flux determination is shown to the left, the horizontal BPM is shown to the right.

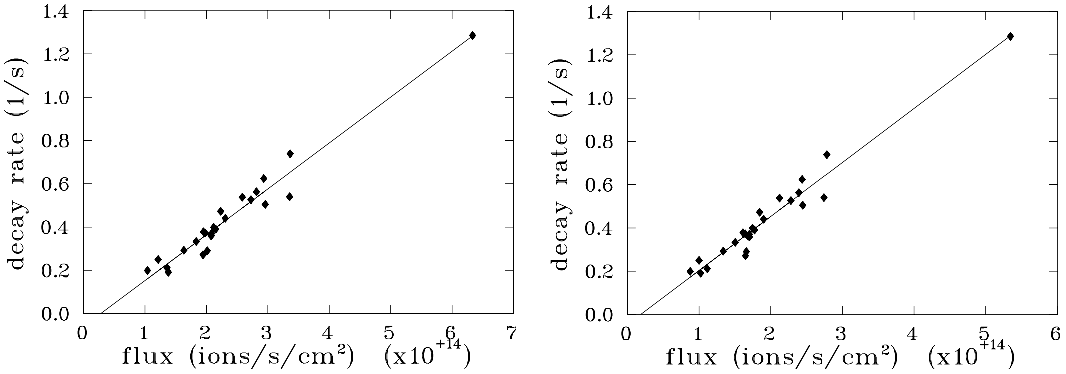

Figure B.5: Measurement of the cross section for O^{8+}. The data using the vertical BPM for the flux determination is shown to the left, the horizontal BPM is shown to the right.

Appendix C

Calibration of the MCA

In order to extract the TOF from the MCA spectrum the channels have to be calibrated. Therefore, a *time calibrator* (ORTEC, 462) is used. The time calibrator generates a certain number of equidistant pulses. Since the distance between the pulses and the total number of pulses is known the spectrum of the MCA can be calibrated. An example is shown in figure C.1. Since the first peak in the spectrum is missed an offset occurs for the calibration.

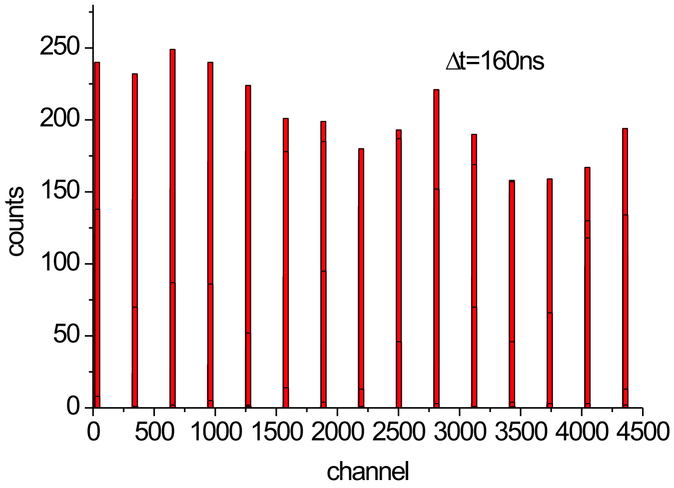

Figure C.1: *Spectrum of the MCA calibration. The distance between the peaks is 0.5 μs. The calibration of channels vs. time yields an offset because the first calibration peak is missed.*

Apart from the calibration several additional delays have to be taken into account in order to obtain the exact TOF spectrum. These delays are caused by electronic devices or cables and the time the reloaded projectile needs until it reaches the recombination detector. Since the flight time of the Cs-ions is in the order of some μs the delays of $\approx 100\,\mathrm{ns}$ cannot be neglected. The delays can be summarized as follows:

- Recombination detector

  The cables and the electronics cause a constant delay for all measurements of $\Delta\, t = 125\,\mathrm{ns} \pm 30\,\mathrm{ns}$.

- Distance between trap and recombination detector

  The delay depends on the energy of the projectile:

  - C^{6+}: $\Delta\, t = 55\,\mathrm{ns} \pm 30\,\mathrm{ns}$,
  - C^{4+}: $\Delta\, t = 84\,\mathrm{ns} \pm 30\,\mathrm{ns}$,
  - O^{8+}: $\Delta\, t = 74\,\mathrm{ns} \pm 30\,\mathrm{ns}$.

The sum of the delays corresponds to the offset (s. Fig. 4.11, 4.12, 4.16) which has to be taken into account in order to determine the correct flight time.

Using the photoionization of cesium to calibrate the time-of-flight for Cs^{1+} the following delays have to be considered:

- Flight time of the photons: $\Delta\, t = 52\,\mathrm{ns} \pm 10\,\mathrm{ns}$,
- Cable delay for the start trigger: $\Delta\, t = 155\,\mathrm{ns} \pm 10\,\mathrm{ns}$.

Since the delays for the photoionization partly compensate each other the final delay can be assumed to be $\Delta\, t = 103\,\mathrm{ns} \pm 15\,\mathrm{ns}$.

In addition there are unknown delays from the photodiode which generates the start trigger for the photoionization measurement. But this delay can be neglected since the two independent time-of-flight measurements yield the same time for Cs^{1+}. The delay of the MCP readout is not known, either. It can be estimated to $\approx 30\,\mathrm{ns}$ from other experiments. This delay is not included in the analysis.

Appendix D

Integration of the Overlap Integral

The integration carried out in equation (3.2) is shown first for one dimension.

$$\begin{aligned}
I &= \int_{-\infty}^{+\infty} n_{\mathrm{Ion}}(\mathrm{x}-\mathrm{x}_0)\cdot n_{\mathrm{Cs}}(\mathrm{x},\mathrm{t})\,dx \\
&= \int_{-\infty}^{+\infty} n_{0,\mathrm{Ion}}\cdot n_{0,\mathrm{Cs}}(\mathrm{t})\cdot e^{-\frac{(x-x_0)^2}{2\sigma_{\mathrm{x,Ion}}}^2}\, e^{-\frac{x^2}{2\sigma^2_{\mathrm{x,Cs}}}}\,dx \\
&= n_{0,\mathrm{Ion}}\cdot n_{0,\mathrm{Cs}}(\mathrm{t})\cdot\sqrt{2\pi}\cdot\frac{\sigma_{\mathrm{x,Ion}}\cdot\sigma_{\mathrm{x,Cs}}}{\sqrt{\sigma^2_{\mathrm{x,Ion}}+\sigma^2_{\mathrm{x,Cs}}}}\cdot e^{-\frac{x_0^2}{2(\sigma^2_{\mathrm{x,Ion}}+\sigma^2_{\mathrm{x,Cs}})}} \\
&= n_{0,\mathrm{Ion}}\cdot n_{0,\mathrm{Cs}}(\mathrm{t})\cdot\sqrt{2\pi}\cdot C'_{\mathrm{x}_0}.
\end{aligned}$$

The integration has to be done for all three dimensions which leads to

$$n_{0,\mathrm{Ion}}\cdot n_{0,\mathrm{Cs}}(\mathrm{t})\cdot(2\pi)^{\frac{3}{2}}\cdot C'_{\mathrm{x}_0}\cdot C'_{\mathrm{y}_0}\cdot C'_{\mathrm{z}_0}.$$

The density $n_{0,\mathrm{Cs}}(\mathrm{t})$ can be written in a particle number using the relation

$$\begin{aligned}
N_{\mathrm{Cs}}(\mathrm{t}) &= \int_{-\infty}^{+\infty} n_{0,\mathrm{Cs}}(\mathrm{t})\cdot e^{-\frac{x_0}{2\sigma^2_{\mathrm{x,Cs}}}}\cdot e^{-\frac{y_0}{2\sigma^2_{\mathrm{y,Cs}}}}\cdot e^{-\frac{z_0}{2\sigma^2_{\mathrm{z,Cs}}}}\,d^3r \\
&= n_{0,\mathrm{Cs}}(\mathrm{t})\cdot(2\pi)^{\frac{3}{2}}\cdot\sigma_{\mathrm{x,Cs}}\cdot\sigma_{\mathrm{y,Cs}}\cdot\sigma_{\mathrm{z,Cs}} \\
\Leftrightarrow n_{0,\mathrm{Cs}}(\mathrm{t}) &= N_{\mathrm{Cs}}(\mathrm{t})\cdot(2\pi)^{-\frac{3}{2}}\left(\frac{1}{\sigma_{\mathrm{x,Cs}}\cdot\sigma_{\mathrm{y,Cs}}\cdot\sigma_{\mathrm{z,Cs}}}\right),
\end{aligned}$$

where $N_{\mathrm{Cs}}(\mathrm{t})$ is the total number of trapped particles in the trap volume V. Using this result the expression for I can be written as

$$\begin{aligned}
I &= n_{0,\mathrm{Ion}}\cdot N_{\mathrm{Cs}}(\mathrm{t})\cdot C_{\mathrm{x}_0}\cdot C_{\mathrm{y}_0}\cdot C_{\mathrm{z}_0} \\
&= n_{0,\mathrm{Ion}}(\vec{\mathrm{r}_0})\cdot N_{\mathrm{Cs}}(\mathrm{t}),
\end{aligned}$$

which is the result shown in equation (3.3).

Appendix E

Consistency of the Data Evaluation

Apart from the check of the resolution limit the deviation from the straight line can be used to check the consistency of the data evaluation. A deviation of the data points from the linearity shows up immediately like e.g. in figure E.1 a). The measurement is done with C^{4+}. Figure E.1 a) makes clear that the measured values cannot be fitted with a straight line. The deviation is caused by the measured vertical widths. Figure E.1 b) shows the vertical width determined by the BPM. Obviously, for low ion currents the width of the beam was close to the resolution limit. Therefore, the flux is not derived correctly. From this measurement the vertical limit can be expected to be 320 μm. The deviation from the resolution mentioned in section 4.1.1 is caused by the electronics of the BPM. The resolution has to be checked for each evaluation.

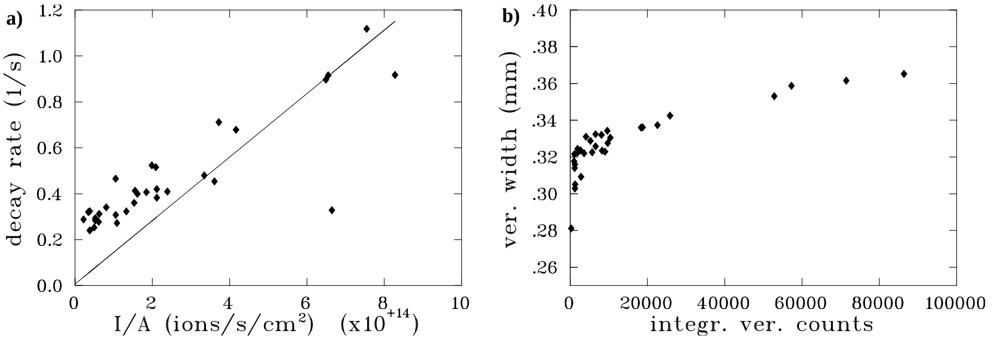

Figure E.1: *a) The measured points deviate from the expected linearity. b) The vertical widths measured by the BPM.*

Bibliography

[Abraham et al., 1995] Abraham, E. R. I., Ritchie, N. W. M., McAlexander, W. I., and Hulet, R. G. (1995). Photoassociative spectroscopy of long-range states of ultracold ^{6}Li$_2$ and ^{7}Li$_2$. *J. Chem. Phys.* **103**, 7773.

[Albrecht, 1996] Albrecht, F. (1996). *Langsame Extraktion am Heidelberger Schwerionenspeicherring TSR*. Dissertation Universität Heidelberg und Max-Planck-Institut für Kernphysik.

[Anderson et al., 1995] Anderson, M. H., Ensher, J. R., Matthews, M. R., Wieman, C. E., and Cornell, E. (1995). Observation of Bose-Einstein Condensation in a Dilute Atomic Vapor. *Science* **269**, 198.

[Arnold et al., 1986] Arnold, W., Baumann, P., Blum, M., Brix, P., Friedrich, A., Grieser, M., Habs, D. Jaeschke, E., Krämer, D., v. Kruechten, B., Martin, C., Matl, K., Povh, B., Repnow, R., Rudnik, U., Schmidt-Rohr, U., Sailer, H., Schuch, R., Steck, M., Steffens, E., and Wiedner, C. A. (1986). The Heidelberg Heavy Ion Test Storage Ring TSR. In: *Proc. 13th Int. Conf. On High Energy Accelerators, Novosibirsk* , pp. 334–340.

[Beutelspacher, 2000] Beutelspacher, M. (2000). *Systematische Untersuchungen zur Elektronenkühlung am Heidelberge Schwerionenspeicherring TSR*. Dissertation Universität Heidelberg und Max-Planck-Institut für Kernphysik, MPI H-V18-2000.

[Burgess, 1964] Burgess, A. (1964). *Astrophys. J.* **139**, 776.

[Dalibard and Cohen-Tannoudji, 1989] Dalibard, J. and Cohen-Tannoudji, C. (1989). Laser Cooling below the Doppler Limit by Polarization Gradients: Simple Theoretical Models. *J. Opt. Soc. Am. B* **6**, 2023.

[Davis et al., 1995] Davis, K. B., Mewes, M.-O., Andrews, M. R., van Druten, N. J., Durfee, D. S., Kurn, D. M., and Ketterle, W. (1995). Bose-Einstein Condensation in a Gas of Sodium Atoms. *Phys. Rev. Lett.* **75**, 3969.

[Dieckmann et al., 1998] Dieckmann, K., Spreeuw, R. J. C., Weidemüller, M., and Walraven, J. T. M. (1998). Two-dimensional magneto-optical trap as a source of slow atoms. *Phys. Rev. A* **58**, 3891.

[Dörner et al., 2000] Dörner, R., Mergel, V., Jagutzki, O., Spielberger, L., Ullrich, J., Moshammer, R., and Schmidt-Böcking, H. (2000). Cold Target Recoil Ion Momentum Spectroscopy: A 'Momentum Microscope' to View Atomic Collisions Dynamics. *Phys. Rep.* **330**, 95.

[Drewsen et al., 1994a] Drewsen, M., Laurent, P., Nadir, A., Santarelli, G., Clairon, A., Castin, Y., Grison, D., and Salomon, C. (1994a). Investigation of sub-Doppler cooling effects in a cesium magneto-optical trap. *Appl. Phys. B* **59**, 283.

[Drewsen et al., 1994b] Drewsen, M., Laurent, P., Nadir, A., Santarelli, G., Clairon, A., Castin, Y., Grison, D., and Salomon, C. (1994b). Investigation of sub-Doppler cooling effects in a cesium magneto-optical trap. *Appl. Phys. B* **59**, 283.

[Eike, 1999] Eike, B. (1999). Aufbau eine magnetooptischen Falle zur transversalen Strahldiagnose am Heidelberger Testspeicherring TSR. Diplomarbeit Universität Heidelberg und Max-Planck-Institut für Kernphysik.

[Eisenbarth et al., 2000] Eisenbarth, U., Mudrich, M., Eike, B., Grieser, M., Grimm, R., Luger, V., Schätz, T., Schramm, U., Schwalm, D., and Weidemüller, M. (2000). Anomalous behaviour of laser-cooled fast ion beams. *Hyp. Int.* **127**, 223.

[Fioretti et al., 1998] Fioretti, A., Comparat, D., Crubellier, A., Dulieu, O., Masnou-Seeuws, F., and Pillte, P. (1998). Formation of Cold Cs_2 Molecules through Photoassociation. *Phys. Rev. Lett.* **80**, 4402.

[Flechard et al., 2001] Flechard, X., Nguyen, H., Wells, E., Ben-Itzhak, I., and DePaola, B. (2001). Kinematically Complete Charge Exchange Experiment in the $Cs^+ + Rb$ Collision System Using a MOT target. *Phys. Rev. Lett.* **87**, 123203/1.

[Grieser, 2002] Grieser, M. (2002). private communication.

[Grimm et al., 2000] Grimm, R., Weidemüller, M., and Ovchinnikov, Y. B. (2000). Optical dipole traps for neutral atoms. In: Bederson, B. and Walther, H. (Eds.), *Advances in Atomic Molecular and Optical Physics* Vol. 42 , p. 95. Academic Press, San Diego.

[GSI, 1996] GSI (1996). GSI-Nachrichten 4/96.

[Gwinner et al., 1994] Gwinner, G., Behr, J. A., Cahn, S. B., Ghosh, A., Orozco, L. A., Sprouse, G. D., and Xu, F. (1994). Magneto-Optic Trapping of Radioactive ^{79}Rb. *Phys. Rev. Lett.* **72**, 3795.

[Hochadel, 1994] Hochadel, B. (1994). Residual-gas ionization beam profile monitor for the Heidelberg test storage ring TSR. *Nucl. Inst. and Meth. A* **343**, 401.

[Hodges and Breig, 1991] Hodges, R. R. J. and Breig, E. L. (1991). Ionosphere-exosphere coupling through charge exchange and momentum transfer in Hydrogen-proton collisions. *J. Geophys. Res.* **96**, 7697.

[Julienne, 1991] Julienne, P. S. (1991). Cold Collisions of Ground- and Excited-state Alkali-metal Atoms. *Phys. Rev. A* **44**, 4464.

[Kasevich et al., 1989] Kasevich, M. A., Riis, E., Chu, S., and DeVoe, R. G. (1989). rf Spectroscopy in an Atomic Fountain. *Phys. Rev. Lett.* **63**, 612.

[Kelbch et al., 1985] Kelbch, S., Ullrich, J., Mann, R., Richard, P., and Schmidt-Böcking, H. (1985). Cross sections for the production of highly charged argon and xenon recoil ions in collisions with high-velocity uranium projectiles. *J. Phys. B* **18**, 323.

[Kleinert, 2002] Kleinert, J. (2002). Ultrakalte Atome als Target in einem Schwerionenspeicherring. Diplomarbeit Universität Heidelberg und Max-Planck-Institut für Kernphysik.

[Lange, 2002] Lange, M. (2002). private communication.

[Lauer, 1999] Lauer, I. (1999). *Transversale Dynamik lasergekühlter $^{9}Be^{+}$-Ionenstrahlen im Speicherring TSR*. Dissertation Max-Planck-Institut für Kernphysik, MPI H-V15-1999.

[Lett et al., 1995] Lett, P. D., Julienne, P. S., and Phillips, W. D. (1995). Photoassociative Spectroscopy of Laser-Cooled Atoms. *Annu. Rev. Phys. Chem.* **46**, 423.

[Lett et al., 1988] Lett, P. D., Watts, R. N., and Westbrook, C. I. Phillips, W. D. (1988). Observation of Atoms Laser Cooled below the Doppler Limit. *Phys. Rev. Lett.* **61**, 117.

[Lu et al., 1994] Lu, Z. T., Bowers, C. J., Freedman, S. J., Fujikawa, B. K., Mortara, J. L., Shang, S. Q., Goulter, K. P., and Young, L. (1994). Laser Trapping of Short-Lived Radioactive Isotopes. *Phys. Rev. Lett.* **72**, 3791.

[Lu et al., 1996] Lu, Z. T., Corwin, K. L., Renn, M. J., Anderson, M. H., Cornell, E. A., and Wieman, C. E. (1996). Low-Velocity Intense Source of Atoms from a Magneto-optical Trap. *PPhys. Rev. Lett.* **77**, 3331.

[Luger, 1999] Luger, V. (1999). *Storage ring target for high-precision beam profile diagnostics based on a magneto-optical trap*. Dissertation Universität Heidelberg und Max-Planck-Institut für Kernphysik.

[Marcassa et al., 1993] Marcassa, L., Bagnato, V., Wang, Y., Tsao, C., Dulieu, O., Band, Y. B., and Julienne, P. S. (1993). Collisional Loss Rate in a Magneto-Optical Trap for Sodium Atoms. *Phys. Rev. A* **47**, R4563.

[Metcalf and van der Straten, 1994] Metcalf, H. and van der Straten, P. (1994). Cooling and Trapping of Neutral Atoms. *Physics Reports* **244**, 205.

[Mortimer, 1987] Mortimer, C. E. (1987). *Chemie*. Georg Thieme Verlag, Stuttgart.

[O'Hanlon, 1988] O'Hanlon, J. F. (1988). *A User's Guide to Vacuum Technology*. Wiley. 2 edition.

[Poel et al., 2001] Poel, M. v. d., Nielsen, C., Gearba, M.-A., and Andersen, N. (2001). Fraunhofer Diffraction of Atomic Matter Waves: Electron Transfer Studies with a Laser Cooled Target. *Phys. Rev. Lett.* **87**, 123201/1.

[Poth, 1990] Poth, H. (1990). Electron cooling: theory, experiment, application. *Phys. Rep.* **196**.

[Prodan et al., 1985] Prodan, J., Migdall, A., Phillips, W. D., So, I., Metcalf, H., and Dalibard, J. (1985). Stopping Atoms with Laser Light. *Phys. Rev. Lett.* **54**, 992.

[Proxitronic, 2002] Proxitronic (2002). www.proxitronic.de.

[Raab et al., 1987] Raab, J., Prentiss, M., Cable, A., Chu, S., and Pritchard, D. (1987). Trapping of Neutral Sodium Atoms with Radiation Pressure. *Phys. Rev. Lett.* **59**, 2631.

[Santos et al., 1995] Santos, M. S., Nussenzveig, P., Marcassa, L. G., Helmerson, K., Flemming, J., Zilio, S. C., and Bagnato, V. S. (1995). Simultaneous Trapping of two Different Atomic Species in a Vapor-Cell Magneto-optical Trap. *Phys. Rev. A* **52**, R4340.

[Schlöder, 1998] Schlöder, U. (1998). Ultrakalte Stöße zwischen Lithium- und Cäsiumatomen in einer kombinierten magnetooptischen Falle. Diplomarbeit Universität Heidelberg und Max-Planck-Institut für Kernphysik.

[Schünemann et al., 1996] Schünemann, U., Manek, I., Grimm, R., Habs, D., and Schwalm, D. (1996). Laser-cooled and trapped atoms as a precision target for heavy-ion beams. *Hyp. Int.* **99**, 127.

[Shevelko et al., 2001] Shevelko, V., Stoehlker, T., and Tolstikhina, I. (2001). Stripping of fast heavy low-charged ions in gaseous targets. *Nuclear Instruments and Methods in Physics Research B* **184**, 295.

[Sørensen, 1987] Sørensen, A. H. (1987). Introduction to Intrabeam Scattering. In: Turner, S. (Ed.), *CERN Accelerator School*. Report CERN 87-10.

[Stancil et al., 1998] Stancil, P. C., Havener, C. C., Krstic, P., Schultz, D. R., Kimura, M., Gu, J.-P., Hirsch, G., Buenker, R. J., and Zygelman, B. (1998). Charge transfer in collisions of C^+ with H and H^+ with C. *Astrophys. J.* **502**, 1006.

[Steane and Chowdhury, 1992] Steane, A. M. and Chowdhury, M. Foot, C. J. (1992). Radiation Force in the Magneto-optical Trap. *J. Opt. Soc. Am. B* **9**, 2142.

[Steck et al., 2001] Steck, M., Beckert, K., Beller, P., Franzke, B., and Nolden, F. (2001). Extremely cooled ion beams in the ESR with evidence of ordering. In: *Proceedings of the 2001 Particle Accelerator Conference, Piscataway, NJ, USA* Vol. 1. IEEE.

[Steck et al., 1996] Steck, M., Beckert, K., Eickhoff, H., Franzke, B., Nolden, F., Reich, H., Schlitt, B., and Winkler, T. (1996). Anomalous Temperature Reduction of Electron-cooled Heavy Ion Beams in the Storage Ring ESR. *Phys. Rev. Lett.* **77**, 3803.

[Tolstikhina and Shevelko, 2000a] Tolstikhina, I. and Shevelko, V. (2000a). Short Commun. Physics (Lebedev Institute, Moscow).

[Tolstikhina and Shevelko, 2000b] Tolstikhina, I. and Shevelko, V. (2000b). Short Commun. Physics (Lebedev Institute, Moscow).

[Townsend et al., 1995] Townsend, C. G., Edwards, N. H., Cooper, C. J., Zetie, K., and Foot, C. J. (1995). Phase-space density in the magneto-optical trap. *Phys. Rev. A* **52**, 1423.

[Townsend et al., 1996] Townsend, C. G., Edwards, N. H., Zetie, K., Cooper, C. J., Rink, J., and Foot, C. J. (1996). High-density Trapping of Cesium Atoms in a Dark Magneto-optical Trap. *Phys. Rev. A* **53**, 1702.

[Turkstra et al., 2001] Turkstra, J., Hoekstra, R., Knoop, S., Meyer, D., Morgenstern, R., and Olson, R. (2001). Recoil Momentum Spectroscopy of Highly Charged Ion Collisions on Magneto-optical Trapped Na. *Phys. Rev. Lett.* **87**, 123202/1.

[Ullrich, 1994] Ullrich, J. (1994). Rückstossionen-Impulsspektroskopie: Ein neuer Weg zur Untersuchung der Dynamik atomarer Reaktionen, Habilitationsschrift der Universität Frankfurt. GSI-Report 03/94.

[Ullrich et al., 1997] Ullrich, J., Moshammer, R., Dörner, R., Jagutzki, O., Mergel, V., Schmidt-Böcking, H., and Spielberger, L. (1997). Recoil-Ion Momentum Spectroscopy. *J. Phys. B* **30**, 2917.

[Wallis et al., 1993] Wallis, H., Werner, J., and Ertmer, W. (1993). Magneto-optical Trapping of Atoms. *Comments At. Mol. Phys.* **28**, 275.

[Wille, 1996] Wille, K. (1996). *Physik der Teilchenbeschleuniger und Synchrotronstrahlungsquellen*. Teubner Studienbücher. Stuttgart 2. edition.

[Witte et al., 1992] Witte, A., Kisters, T., Riehle, F., and Helmcke, J. (1992). Laser Cooling and Deflection of a Calcium Atomic Beam. *J. Opt. Soc. Am. B* **9**, 1030.

[Wiza, 1979] Wiza, J. L. (1979). Microchannel Plate Detectors. *Nucl. Instr. and Meth.* **162**, 587.

[Wolf et al., 2000] Wolf, A., Gwinner, G., Linkemann, J., Saghiri, A., Schmitt, M., Schwalm, D., Grieser, M., Beutelspacher, M., Bartsch, T., Brandau, C., Hoffknecht, A., Müller, A., Schippers, S., Uwira, O., and Savin, D. (2000). Recombination in electron coolers. *Nucl. Inst. Meth. A* **441**, 183.

[Zajfman et al., 1995] Zajfman, D., Amitay, Z., Broude, C., Forck, P., Seidel, B., Grieser, M., Habs, D., Schwalm, D., and Wolf, A. (1995). Measurement of Branching Ratios for the Dissociative Recombination of Cold HD^+ Using Fragment Imaging. *Phys. Rev. Lett.* **75**, 814.

Danksagung

Ein solches Experiment allein am Laufen zu halten, ist fast unmöglich. Dass man dabei Hilfe braucht, ist klar, dass man sie bekommt, ist nicht selbstverständlich - deshalb möchte ich mich an dieser Stelle bedanken. Bedanken bei allen, die zum Enstehen dieser Arbeit beigetragen habe.

Prof. Dirk Schwalm. Vielen Dank, dass ich diese Arbeit in Ihrer Gruppe anfertigen konnte. Herzlichen Dank auch für die vielen wertvollen und kritischen Diskussionen, besonders im Hinblick auf die Ionendetektion.

Matthias Weidemüller. Vielen Dank für die Unterstützung beim Schreiben dieser Arbeit und für die vielen hilfreichen Diskussionen. Dein Enthusiasmus für das Experimentieren hat mich oft weitergebracht, wenn der Ring einen mal wieder in ein tiefes Loch gezogen hat. Alles Gute für Dich in Freiburg!

Rudi Grimm. Vielen Dank für die gute Betreuung in Deiner Zeit hier. Leider bist Du jetzt wohl der einzige 96-Fan in Innsbruck!

Herzlichen Dank möchte ich auch sagen an Herrn Prof. H.-J. Kluge für die Bereitschaft, diese Arbeit als Zweitgutachter zu bewerten.

Meinen Diplomanden:
Frank Herrmann, mit dem ich das Baby BPMMOT in den TSR gehievt und ringtauglich gemacht habe. Die erste Strahlzeit lief auch gut bis wir feststellten, dass unser Channeltron den Betrieb eingestellt hatte. Auch das Umtaufen in TSR-MOT half nichts!

Jan Kleinert. Das Jahr mit Dir ist viel zu schnell vorbeigegangen. Wir haben sicher viel gelitten am Ring und auf *La Galère*, aber genauso tiefe Freude haben wir gemeinsam empfunden. Danke für die super Zusammenarbeit, den Spass und das Wissen, sich auf Dich immer verlassen zu können! Ich wünsche Dir alles Gute in Amerika und hoffe, dass wir weiterhin den Kontakt halten!

Achim Dahlbokum. Achim hat im Zelt den anaeroben Betrieb für die Experimentatoren erfunden. Das Justieren ging danach wie von selbst! Sogar im *Notstrom* hat Achim Labview noch das Fürchten gelehrt! Leider fürchte ich, dass es mit Werder in dieser Saison nichts wird! Vielen Dank für die Hilfe mit den Bildern und das knallharte Korrekturlesen.

Meine Kolleginnen und Kollegen:
Herzlichen Dank für hervorragende Klima in unserer Gruppe! Die Atmosphäre trägt einfach dazu bei, dass das Arbeiten Spaß macht! An den vierfachen Rydberger: Michaela (für das tägliche Backup), Kilian (das Genie beherrscht das Chaos!), Markus und Simon. An die Li-Cs: Marcel, Stefan, Jörg, Marc und Mathias. Ganz besonderer Dank an Udo Eisenbarth: Strahlzeiten haben mit Dir immer Spaß gemacht! Herzlichen Dank für die Hilfe beim Umbauen der Experimentsteuerung. Ohne Dich wäre sie bis zur Strahlzeit sicher nicht fertig gewesen!

An die Innsbrucker Gang: Markus, David, Tino, Selim (Duck-Tape rules!)!

Danke an Helga Krieger, die mich während des Schreibens beherbergt hat und für die vielen kleinen aber wertvollen Hilfen!

Ein großes Danke an die gesamte Strahlzeit-Crew: Frank, Jan, Achim, Udo, Sandro und Patrick. Vielen Dank für Euer aller Engagement. Ohne Euch wären viele der gemachten Messungen nicht möglich gewesen! Danke an Manfred und Kurt für das unermüdliche Neueinstellen des Rings und die vielen kleinen Tricks! Insbesondere auch dafür am Wochenende einen Ansprechpartner zu haben!

Dank an die Werkstätten: Hier gab es immer Hilfe, wenn es brannte. Besonderen Dank an die Hauptwerkstatt, die den Aufbau für den Ionendetektor auch bei engstem Zeitplan punktgenau fertig hatte!

Danke an Prof. Ullrich und Robert Mooshammer für wertvolle Diskussionen. Vielen Dank an V.P. Shevelko für die Rechnungen zu unseren Messungen!

Ein riesiges Dankeschön an meine Eltern, die mich während des gesamten Studiums und der Promotion unterstützt haben. Danke nicht nur für die finanzielle Hilfe sondern für all die vielen Hilfen jeglicher Art und die Aufmunterungen, wenns mal nicht so rund lief! Und natürlich auch an meine Großeltern, die mich ebenso unterstützt haben.

Alexander und Katrin. Danke für Eure Hilfe. Egal, ob Strahlzeit, Schreiben oder andere Sorgen - Euer Lachen hat mir immer wieder Kraft gegeben. Vieles wäre ohne Eure Unterstützung sicher viel schwerer gewesen. Das Leben ist mit Euch einfach wunderbar!

Vielen Dank an Euch alle!

Und dass mir keine Klagen kommen! Aber Ihr wisst ja wie’s ist:

Muss ja...!